

NORTHWESTERN UNIVERSITY

Phonon-Defect Interactions in Thermoelectric Materials

A DISSERTATION

SUBMITTED TO THE GRADUATE SCHOOL
IN PARTIAL FULFILLMENT OF THE REQUIREMENTS

for the degree

DOCTOR OF PHILOSOPHY

Field of Materials Science and Engineering

By

Ramya L. Gurunathan

EVANSTON, ILLINOIS

December 2021

© Copyright by Ramya Gurunathan 2021
All Rights Reserved

ABSTRACT

Phonon-Defect Interactions in Thermoelectric Materials

Engineering heat transport in materials is essential for thermal management in a wide range of technologies, from batteries to thermoelectrics. Materials host a wide spectrum of heat-carrying phonons, which vary in their frequency, spatial extent, and degree of plane-wave character. This diversity in phonon properties leads to complex behaviour, especially in materials with structural complexity, defects, and internal strain sources. The study of thermal conductivity has benefited from simple, physics-based models for over 70 years, as they are easily implemented, elucidate underlying mechanisms, and can even help point to exotic physics when they fail to describe a system. Their lasting relevance supports the argument for continued work on analytic, physical expressions in emerging fields of materials science even as new techniques in simulation and materials informatics become widespread. This thesis primarily focuses on the development of analytic theory to describe the phonon interactions with structural defects. Special focus is given to the phonon scattering effects of point defects and low energy interfaces, which are composed of an underlying array of interfacial dislocations.

We start by reviewing previous descriptions of phonon—point-defect interactions and presenting a conceptually clear model of point defect scattering. We then apply this model to study the thermal properties in multicomponent alloy systems for thermoelectrics. We additionally show an extension of alloy scattering models for charge carriers to high dimensional alloy systems by drawing analogy to the calculation of excess Gibbs free energy. Design rules are suggested based on this modelling for when a reduction in thermal conductivity can be expected from multicomponent alloying.

We end with a discussion of phonon-interface scattering and introduce our model of the thermal boundary resistance R_K of low-energy grain boundaries and interfaces. Our modelling of symmetric tilt and twist grain boundaries as well as semicoherent heterointerfaces helps to address fundamental questions about R_K such as: How does the R_K of a twist and tilt grain boundary compare? How does R_K relate to grain boundary angle and energy? How does the degree of misfit at a heterointerface impact its R_K ?

Acknowledgements

Being a member of the Snyder group has been a true privilege. If I had to pick, my favorite part of the PhD experience has been standing in front of the office whiteboard discussing scientific problems together. The moments of clarity, confusion, and laughter are equally cherished. Jeff, thank you for your consistent support and for leading me to such interesting research problems. I have learned so much just from observing the questions you ask and the approach you take to distill complex phenomena into intuitive, pedagogical nuggets of information. The humility and affability that you bring to research work is equally inspiring—I suppose I should also thank “the gut” and its musings as well.

To the labmates I shared time with, I feel so lucky to have worked with you. You are all simply so creative and kind. At one of Jeff’s parties, he described us all as “basically cousins,” and that felt like the truth. You feel like my academic cousins from around the world. Special thanks to Riley Hanus, my consistent mentor, who believed in my ability to tackle this thesis work far before I believed it myself. I am so grateful to my committee members, Profs. Anupam Garg, Peter Voorhees, and Chris Wolverton. Anupam especially taught me so much about concise and clear communication of physical concepts.

I have also been lucky during this time to collaborate with excellent scientists outside of Northwestern. Changning Niu and the whole team at Questek offered me a truly fun and rewarding foray into ICME and scientific software development. Thanks also to Logan Ward and the rest of the TECCA team for their mentorship and great scientific discussions covering thermoelectrics, statistics, and database design. I couldn’t leave out Prof. Eric Toberer and the co-PIs of the DMREF project— despite not being heavily involved in this project, these Zoom calls were my favorite of the week. Finally, I am so thankful to my previous mentors. Special thanks to Drs.

Allen Kimel and Suzanne Mohny of Penn State University, who continue to be active members of my support team.

The friends I've made during grad school have been such an unexpected boon. A shout-out to those who banded together with me over the course of the COVID-19 pandemic: Nikolay Markov, Hayley White, Ali Ehlen, Hector Manuel Lopez Rios, Sarah Schlossberg, and Neto Canton-Josh. Rogan Grant, you know as well as I that your support and encouragement was always valuable but, at times, crucial to get me to this point. And to Ellie G, the 1-year-old lab/hound mix, I only wish you knew how much your daily excitement means to me.

Finally, I must credit those who have truly stuck with me through thick and thin, my family. My mother and father, Dr. Saraswathy and Mr. Vasudevan Gurunathan have, in every step of the way, shaped my path as a scientist and engineer. They are, in addition to my brother, Arun, sister-in-law, Sanya, and my niece, Neha, my biggest cheerleaders. I have leaned on my family's love and support during so many important junctions of my PhD experience.

Notation Conventions

Physical Constants

Boltzmann constant $k_B = 1.38 \times 10^{23}$ J/K

Planck constant $\hbar = 1.054 \times 10^{-34}$ J·s

Electron charge $e = 1.602 \times 10^{-19}$ C

Electron mass $m_e = 9.11 \times 10^{-31}$ kg

Conventions

- (1) Vector quantities will be indicated with a **bold font**. For example, the phonon wavevector $\mathbf{q} = [q_x, q_y, q_z]$. The non-bold character indicates the magnitude of the vector (e.g. $|\mathbf{q}| = q$). Components of multidimensional tensor quantities will be signified with an ijk indices typically referring to the Cartesian direction of each dimension of the tensor (e.g. strain tensor component ϵ_{ij} is the j component of the gradient of the displacement in the i direction).
- (2) Variable quantities are italicized, whereas non-italic subscripts and superscripts tend to indicate categorical labels.
- (3) Phonon mode will often be designated with a combined notation $\mathbf{q}s$, where \mathbf{q} is the wavevector and s is the branch index.
- (4) Unless otherwise indicated, V_{tot} will refer to the volume of the crystal, while V_0 will refer to the volume per atom.
- (5) Phonon wavevectors are designated as \mathbf{q} , while electronic wavevectors are designated as \mathbf{k} . For scattering problems, the scattering vector is designated as $\mathbf{Q} = \mathbf{q}' - \mathbf{q}$.

Table of Contents

ABSTRACT	3
Acknowledgements	5
Notation Conventions	7
Table of Contents	8
Chapter 1. Introduction and Motivation	11
1.1. Thermal Engineering of Materials	11
1.2. Thermoelectric Conversion	12
1.3. Thesis Roadmap	18
Chapter 2. Theoretical Background	20
2.1. Lattice Dynamics and Phonons	20
2.2. Phonon Scattering Theory	27
2.3. Calculating Transport Coefficients	35
Chapter 3. Phonon–Point-Defect Scattering	39
3.1. Introduction: Approaches to Point Defect-Phonon Scattering	39
3.2. Lattice Perturbation Due to Point Defects	40
3.3. Callaway-Klemens Model of Point-Defect Scattering	42
3.4. Lattice thermal conductivity versus n Trends in zT Predictions	53
3.5. Beyond the Phonon Limit: Diffusons and Scattering Theory	55
3.6. Conclusions	57

Chapter 4. Thermoelectric Transport in Multicomponent Alloys	59
4.1. Motivation: Unexplored Phase Space for Thermoelectric Materials	59
4.2. Theoretical Background	60
4.3. Excess Thermodynamic Quantity Estimations: Redlich-Kister Polynomial and Muggianu Model	65
4.4. Results and Discussion	68
4.5. Multicomponent Alloy Design Rules	74
4.6. Conclusions	80
Chapter 5. Thermal Resistance of Grain Boundaries and Interfaces	81
5.1. Motivation: Thermal Management in Semiconductor Devices	81
5.2. Phonon-Boundary Scattering Background	82
5.3. Existing Approaches to Evaluating Phonon-Boundary Scattering	90
5.4. Model for Low Energy Grain Boundaries and Interfaces	94
5.5. Additional Interfacial Dislocation Scattering Effects: Core Scattering and Phonon Drag	117
5.6. Conclusions	121
Chapter 6. Conclusions and Future Directions: Bridging Atomistic and Continuum Methods	123
References	127
Appendix A. Phonon Boltzmann Transport Equation	148
Appendix B. Phonon Relaxation Time Derivations	150
B.1. Mass Defect Scattering	150
B.2. Phonon-Phonon Scattering	151
Appendix C. Elaborated Example of Vacancy Scattering	154
Appendix D. Pseudoternary half-Heusler Data Summary	156

Appendix E. Grain Boundary Scattering: Model Parameters and Strain Field Descriptions	160
E.1. Model Parameters	160
E.2. Twist Boundary Strain Field Details	160
E.3. Heterointerface Strain Field Details	162
List of Tables	164
List of Figures	166

CHAPTER 1

Introduction and Motivation**1.1. Thermal Engineering of Materials**

In the United States, 67% of energy goes unutilized as waste heat due to losses in power generation, transmission, and conversion [1]. Materials design principles for directing and controlling heat conduction are therefore highly impactful across applications like thermoelectric conversion, thermal barrier coatings, and heat management systems for power electronic and energy storage devices. A common challenge in the discipline of thermal conductivity engineering is the heterogeneity of heat carrying lattice vibrations, or phonons, within a single material. Most materials host a broad spectrum of phonons with wavelengths ranging from Ångstroms to micrometers, which couple to different types of structural defects and sources of internal strain within the material. Therefore, understanding the heat carried by phonons, or the lattice thermal conductivity κ_L , is inherently a multiscale problem, requiring information about the bonding (atomistic), internal strain effects (nanoscale), and grain or pore structure (microscale).

Since functional thermal materials also tend to contain numerous structural defects, either as a product of processing or to intentionally tailor material properties, understanding phonon-defect interactions is crucial to thermal materials design. Demonstrations of engineering low, high, or anisotropic thermal conductivity through defects exist for several technological applications. Thermal barrier coatings (TBCs), for example, are thermal insulators used to coat components exposed to high temperatures, such as the blades and vanes in gas turbines [2, 3]. A state-of-the-art TBC material is yttria-stabilized zirconia (YSZ), and introducing oxygen and cation vacancies is one of the most common and effective ways to further reduce the thermal conductivity of these materials [2]. In thermoelectric applications, a focus of this thesis, engineering low thermal conductivity is

required to maintain a temperature differential across the thermoelectric module. Many of the defect engineering strategies discussed here will be towards the goal of scattering phonons and suppressing thermal transport.

In other instances, such as power electronic devices, heat dissipation away from the device is required to prevent over-heating. Current nano-/micro-electronic devices, however, contain a high density of interfaces, separating the package, substrate, channel, barrier layer, and electrodes. Therefore, in order to achieve higher device densities and power densities, these interfaces should be designed to be as thermally conductive as possible [4, 5].

Finally, a unique approach to thermal dissipation involving linear defects, or dislocations, was presented by Sun *et al.* [6]. As discussed in detail in Chapter 5, the phonons tend to strongly interact with dislocation strain fields, which can lead to larger scattering for phonons travelling perpendicular to the dislocation line. In their work, Sun *et al.* leveraged this effect to induce anisotropic thermal transport in the otherwise fairly isotropic material, wurtzite InN using vertically-aligned threading dislocations. The engineered thermal anisotropy is proposed as a mechanism to direct heat flow in thin film semiconductor devices such as power electronics or light emitting diodes (LEDs) [6].

The impact of thermal engineering through material defects is therefore widespread. In the following section, we will introduce the fundamentals of thermoelectric conversion, as this is the technological focus of this thesis work.

1.2. Thermoelectric Conversion

Thermoelectric modules directly interconvert between a temperature gradient and electrical power in a fully solid-state device. This profound ability to convert between a “lossy” form of energy, excess heat, and a highly transferrable form of energy, electricity, affords two major technologies that can greatly promote sustainable energy harvesting and utilization. The first, thermoelectric power generation, involves reclaiming rejected heat to produce clean, electrical power. A typical nuclear fission reactor, for example, operates at 25-30% efficiency, and therefore produces a steady supply

of low-grade (200-277°C) waste heat. Recycling of this waste heat into electricity via thermoelectric conversion not only improves the operating efficiency, but also provides an environmentally-friendly heat management strategy versus cooling water, which is released at very hot temperatures into nearby waterways [7].

The second technology, thermoelectric cooling, stems from the reciprocal process and involves driving a DC current through a thermoelectric module, allowing it to operate as a heat pump. Solid-state cooling could provide an opportunity for personalized temperature control devices to reduce the $\sim 40\%$ of building energy consumption currently devoted to heating, ventilation, and air conditioning (HVAC) [8]. The coefficient of performance (COP) for a thermoelectric cooler is solely dependent on the hot and cold side temperatures, T_c and T_h (which are limited by the heat-exchanger losses), as well as the device ZT , which is related to the thermoelectric materials selection. The COP, labeled as ϕ , is the heat removed Q_c divided by the electrical power consumed W . The thermodynamic limit of ϕ is set by the Carnot efficiency $T_c/(T_h - T_c)$, which in thermoelectric modules is reduced by the parenthetical factor below, where $\Delta T = T_h - T_c$ and \bar{T} is the average temperature across the device:

$$(1.1) \quad \phi = \frac{T_c}{\Delta T} \left(\frac{\sqrt{1 + Z\bar{T}} - T_h/T_c}{\sqrt{1 + Z\bar{T}} + 1} \right)$$

The coefficient of performance for a thermoelectric cooler increases as ΔT decreases, and existing thermoelectric coolers meet the U.S. EnergyStar certification at ΔT values of about 8°C while being competitive with vapor compression cycle systems [9]. If rather than attempting to cool large spaces, a distributed cooling approach was implemented with reduced ΔT values (e.g. cooling car seats rather than air conditioning), thermoelectric coolers are a compact, quiet, and reliable solution. However, to realize thermoelectric low-grade waste heat recovery or refrigeration technologies with larger ΔT applications, $ZT > 2$ is required [7, 10].

Realizing efficient thermoelectric materials, which can fundamentally shift both waste heat recovery and temperature control systems, directly addresses the exigent technological demands

stated in the White House research priorities memorandum under *Energy and Environmental Leadership*, which calls for investment in early-stage technology that can “harness American energy resources safely and efficiently” [11].

1.2.1. Thermoelectric Material Performance

In the previous section, we introduced the device ZT , a quantity related to the efficiency of a thermoelectric generator or cooler. ZT is an aggregate, macroscopic parameter, accounting for a complete device, composed of both n- and p-type components, wired electrically in series and thermally in parallel, and operating over a temperature gradient [12]. If we zoom into a microscopic, finite element of a thermoelectric leg, we can define what is often referred to as the material zT , the combination of T-dependent material properties defined at a specific temperature T along the temperature gradient:

$$(1.2) \quad zT = \frac{S^2\sigma}{\kappa}T.$$

The three main material properties which enter into the zT equation include the following:

- **Seebeck coefficient** (S or α ; $\mathbf{V/K}$): The voltage produced by a temperature differential (ΔT) is determined by the Seebeck coefficient as $V = \alpha\Delta T$. The Seebeck coefficient will relate to the imbalance of electronic states around the Fermi level. As a result, it is related to effective mass derived from the density-of-states.
- **Electrical conductivity** (σ ; $\mathbf{S/m}$): The electrical conductivity characterizes a material’s ability to transport charge, and is related to the charge carrier density, lifetime, and inertial effective mass.
- **Thermal conductivity** (κ ; $\mathbf{W/m/K}$): The thermal conductivity is the ratio of the heat flux to the temperature gradient across the system, and is a measure of a material’s ability to transport heat. In semiconductors, the majority of heat is carried by free charge carriers

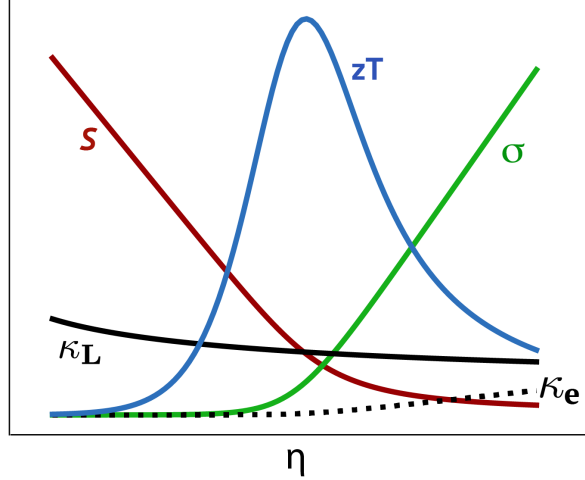


Figure 1.1. **zT Dependence on Doping Level** The constituents of the figure-of-merit zT each have a dependence on doping level, such that zT itself tends to be sharply peaked at an optimal doping level. Therefore, without the assurance of optimal doping, zT is an inadequate metric of the true potential of a thermoelectric material. In order to reliably compare literature values, doping-independent metrics such as the transport function σ_{E0} are therefore preferable.

and lattice vibrations. The total thermal conductivity is the sum of these electronic and lattice contributions: $\kappa_{\text{tot}} = \kappa_e + \kappa_L$.

Each quantity is dependent on the electron chemical potential, as shown in Figure 1.1 through the mutual dependence on the reduced Fermi level (η). Also referred to here as the doping level, η is a function of effective mass m^* and the carrier concentration n , and is most easily manipulated through doping. Note that even the lattice thermal conductivity is depicted with a soft dependence on η because of phonon scattering off of dopant atoms as well as potential charge carrier lattice softening [13,14]. This mutual dependence on doping level is such that zT tends to peak at a specific optimum doping level. This makes reports of zT difficult to compare between different studies without assurance that each material is optimally doped. Instead, utilizing doping-independent metrics is a preferred method of benchmarking thermoelectric materials.

To derive the doping-independent metrics, it is useful to first discuss the energy-dependent transport function, σ_E , a measure of the “conductive quality” of carriers at energy E (note: the same expression will be shown to apply to phonons in the phonon gas model; Section 2.3.1):

$$(1.3) \quad \sigma_E = e^2 \langle v^2(E) \rangle \tau(E) g(E),$$

where $\langle v^2(E) \rangle$ is the directionally-averaged squared velocity, τ is the carrier lifetime, and g is the density of states. The three electronic components of the zT equation, namely, S , σ , and κ_e can all be understood as convolutions of the electronic transport function σ_E and selection functions which include the Fermi-Dirac distribution $f(E)$ and the Fermi level E_F [15]:

$$(1.4) \quad \begin{aligned} \sigma &= \int \sigma_E(E) \frac{-\partial f}{\partial E} dE \\ \alpha\sigma &= \frac{1}{e} \int \sigma_E(E) \left(\frac{E - E_F}{T} \right) \frac{-\partial f}{\partial E} dE \\ \kappa_e &= \frac{1}{e^2} \int \sigma_E(E) \frac{(E - E_F)^2}{T} \frac{-\partial f}{\partial E} dE - \alpha^2 \sigma T \end{aligned}$$

It is often possible to approximate the band edge as a parabolic dispersion to simplify the energy-dependence of σ_E . In addition, in semiconductor materials, it is common for the carrier lifetime to vary as $1/g(E)$. For example, this is the energy dependence expected for phonon scattering of charge carriers, which is typically the dominant effect. In this scenario, it is easy to show that σ_E should vary linearly with energy inside the band, following the expression $\sigma_E = \sigma_{E0}E$ with the constant σ_{E0} determining the slope. The electronic transport coefficient σ_{E0} can be thought of as describing the conductive quality of the band. It can be fit to the S vs. σ relation as each transport coefficient can be determined exclusively by σ_{E0} and η via the Fermi integrals F_j , where j represents the order [16]:

$$(1.5) \quad \begin{aligned} \sigma &= \sigma_{E0} F_0 \\ \alpha &= \frac{k_B}{e} \left(\frac{2F_1}{F_0} - \eta \right) \end{aligned}$$

The σ_{E0} is an energy-independent and η -independent metric that is related to the maximum achievable power factor $\alpha^2\sigma$ through optimal doping. The quality factor B , which is similarly correlated to the maximum achievable zT through optimal doping is then proportional to σ_{E0} divided by the lattice thermal conductivity κ_L , another roughly doping-independent metric:

$$(1.6) \quad B = \left(\frac{k_B}{e} \right)^2 \frac{\sigma_{E0}}{\kappa_L}.$$

1.2.1.1. Attributes of a Good Thermoelectric Material. Designing materials with excellent electronic transport and poor thermal transport is difficult, since the two are often coupled. The paradigm for thermoelectric material selection and design is referred to as the “phonon-gas electron-crystal,” and numerous structure types and classes of semiconductors have been explored to reach these properties. Most thermoelectric materials are degenerately-doped semiconductors, as this places the Fermi level just inside the band, close to a band edge, where the Seebeck coefficient tends to peak [15]. One of the main trade-offs in thermoelectric materials is between effective mass and mobility. High effective mass tends to indicate a large density-of-states near the Fermi level, which promotes large Seebeck coefficients, but also typically indicates heavy charge carriers with low mobility [12]. Many excellent thermoelectric materials, including Bi_2Te_3 , PbTe , and CoSb_3 , balance this trade-off through high band degeneracy. In this case, several electronic states with high curvature and low inertial mass converge at the same energy, leading to a large total density of states. High band degeneracy can be achieved through having band edge states at low symmetry k-points of high symmetry materials, or by having several electronic states at different k-points converged in energy at the band edge [17, 18].

Just like complexity of electronic structure with a large multiplicity of contributing electronic bands, complexity of the lattice can lead to desirable thermal properties. Complex unit cell materials carry a large amount of heat through flat, optical modes with low group velocities and short lifetimes, and therefore exhibit low lattice thermal conductivity values [12, 19]. Further disrupting the lattice through defects and disorder lead to reductions in κ_L , a primary focus of this thesis work.

1.3. Thesis Roadmap

In this thesis, we will first review fundamentals of lattice dynamics and thermal transport in Chapter 2: Theoretical Background. Particular emphasis is placed on the relationship between first-principles phonon descriptions and analytic transport theories, the latter of which are the primary tool used in this thesis. Chapter 3 summarizes our work on analytic phonon–point-defect scattering models. Here, we review implementations of point-defect scattering models to reveal inconsistencies, which have overshadowed important differences between the scattering strength of point defects. We propose a formulation to resolve these discrepancies and demonstrate a cancellation of errors, which may account for the robustness of analytic models. This chapter draws from three publications, and materials are reproduced with permission from:

- 1) R. Gurunathan, R. Hanus, M. Dylla, A. Katre, and G.J. Snyder. *Physical Review-Applied*, 13, 034011 (2020). Copyright 2020 by the American Physical Society [20].
- 2) R. Gurunathan, R. Hanus, and G.J. Snyder. *Materials Horizons*, 7, 1452–1456 (2020). with permission from the Royal Society of Chemistry [13].
- 3) S. Anand, R. Gurunathan, T. Soldi, L. Borgsmiller, R. Orenstein and G.J. Snyder. *Journal of Materials Chemistry C*, 8, 10174–10184 (2020). with permission from the Royal Society of Chemistry [21]

Chapter 4 includes work completed as part of the “Accelerated Discovery of Compositionally Complex Alloys for Direct Thermal Energy Conversion” DOE project DE-AC02-76SF00515. We apply analytic alloy scattering models, whose functional form is inspired by excess Gibbs free

energy models, to predict thermoelectric transport properties in multicomponent alloys formed between three or more thermoelectric compounds. We then discuss when multicomponent alloying is beneficial for the suppression of thermal conductivity. The content of the chapter heavily draws from a manuscript in preparation.

Chapter 5 covers the topic of phonon scattering and thermal resistance at grain boundaries and interfaces. This chapter includes a review of the thermal boundary or Kapitza resistance, including the factors that influence its value and the analytic and simulation-based approaches to estimating its value. Sections of this introduction are reproduced from R. Hanus, R. Gurunathan, L. Lindsay, M.T. Agne, J. Shi, S. Graham, and G.J. Snyder. Thermal transport in defective and disordered materials. *Applied Physics Reviews*, 8, 031311 (2021). [22] with the permission of AIP Publishing. The chapter additionally discusses a general framework for calculating the phonon scattering and thermal resistance of low-energy grain boundaries and interfaces, which can be decomposed into arrays of interfacial dislocations. The periodic dislocation arrays produce a unique type of phonon scattering, referred to as *diffractive scattering*. When combined with the thermal resistance effects stemming from the acoustic mismatch at the interface, this model captures important trends between interfacial thermal resistance, structure, and strain energy. Sections of this chapter are reproduced with permission from R. Gurunathan, R. Hanus, A. Garg, and G.J. Snyder. *Physical Review B*, 103, 144302 (2021). Copyright 2021 by the American Physical Society [23].

CHAPTER 2

Theoretical Background

2.1. Lattice Dynamics and Phonons

Notation in this section primarily comes from Srivastava [24], Dove [25], and Born [26].

The total lattice energy will be a sum of kinetic and potentials energy terms ($T + U$). In turn, the potential energy is commonly written as a Taylor series in terms of atomic displacements \mathbf{u} . The displacements are labelled by Cartesian indices (i.e. i) referring to the x , y , or z direction and a lattice position (i.e. \mathbf{r}), which combines both the location of the unit cell housing the atom and the position of the atom within the unit cell [24, 26]:

$$(2.1) \quad U = U_0 + \sum_{\mathbf{r}} \sum_i \left. \frac{\partial U}{\partial u_i(\mathbf{r})} \right|_{u=0} \mathbf{u}_i(\mathbf{r}) + \frac{1}{2} \sum_{\mathbf{r}, \mathbf{r}'} \sum_{i, j} \left. \frac{\partial^2 U}{\partial u_i(\mathbf{r}) \partial u_j(\mathbf{r}')} \right|_{u=0} \mathbf{u}_i(\mathbf{r}) \mathbf{u}_j(\mathbf{r}') + \\ \frac{1}{3!} \sum_{\mathbf{r}, \mathbf{r}', \mathbf{r}''} \sum_{i, j, k} \left. \frac{\partial^3 U}{\partial u_i(\mathbf{r}) \partial u_j(\mathbf{r}') \partial u_k(\mathbf{r}'')} \right|_{u=0} \mathbf{u}_i(\mathbf{r}) \mathbf{u}_j(\mathbf{r}') \mathbf{u}_k(\mathbf{r}'') + \dots$$

The partial derivatives of potential energy with respect to displacement are referred to as the “force constants”. Their rank or order signifies the number of interacting bodies that they describe energetically. The first term in the expansion U_0 is the potential energy for a static lattice, and is often ignored in lattice dynamical problems. The second term is essentially the total force on each atom, and is equal to 0 at equilibrium [24, 25].

In the harmonic approximation used to define normal phonon modes the third term, based on the second order force constant, is the only one considered. For simplicity, we’ll use standard convention to designate the second order force constant as:

$$(2.2) \quad \Phi_{ij}(\mathbf{r}, \mathbf{r}') = \left. \frac{\partial^2 U}{\partial u_i(\mathbf{r}) \partial u_j(\mathbf{r}')} \right|_{u=0}$$

Writing the equations of motion, which are identical to the classical case of a harmonic oscillator: $F = Ma = -kx$, we arrive at:

$$(2.3) \quad M_{\mathbf{r}} \ddot{u}_i(\mathbf{r}) = - \sum_{j\mathbf{r}'} \Phi_{ij}(\mathbf{r}') u_j(\mathbf{r}')$$

The solution for the displacement \mathbf{u} for the atom at position \mathbf{r} with mass M will be expressed as a sum of travelling plane waves, each described by a wave vector and branch index $\mathbf{q}s$, frequency $\omega_{\mathbf{q}s}$, polarization vector $\mathbf{e}_{\mathbf{q}s}$, and amplitude $A_{\mathbf{q}s}$ [26]:

$$(2.4) \quad \mathbf{u}_i(\mathbf{r}) = \frac{1}{\sqrt{M}} \sum_{\mathbf{q}s} \mathbf{e}_{i\mathbf{q}s}(\mathbf{r}) A_{\mathbf{q}s} \exp(i(\mathbf{q} \cdot \mathbf{r} - \omega_{\mathbf{q}s} t))$$

Substituting this solution into Equation 2.3, we get:

$$(2.5) \quad \sqrt{M} \sum_{\mathbf{q}s} \omega_{\mathbf{q}s}^2 \mathbf{e}_{i\mathbf{q}s}(\mathbf{r}') A_{\mathbf{q},s} \exp(i(\mathbf{q} \cdot \mathbf{r}_j - \omega_{\mathbf{q}s} t)) = - \sum_{\mathbf{q}s;\mathbf{r}'} \frac{\mathbf{e}_{j\mathbf{q}s}(\mathbf{r}) A_{\mathbf{q},s}}{\sqrt{M'}} \Phi_{ij}(\mathbf{r}') \exp(i(\mathbf{q} \cdot \mathbf{r}' - \omega_{\mathbf{q}s} t))$$

With some simplification, we can write this equation in the form of an eigenvalue problem:

$$(2.6) \quad \omega_{\mathbf{q}s}^2 \mathbf{e}_{i\mathbf{q}s}(\mathbf{r}) = D_{ij}(\mathbf{q}) \mathbf{e}_{i\mathbf{q}s}(\mathbf{r}).$$

Here, $D_{ij}(\mathbf{q})$ is referred to as the dynamical matrix and is equal to the mass-normalized Fourier transform of the second order force constants: $D_{ij}(\mathbf{q}) = \frac{1}{\sqrt{M}\sqrt{M'}} \sum_{\mathbf{r}'} \Phi_{ij}(\mathbf{r}, \mathbf{r}') \exp(i\mathbf{q} \cdot \mathbf{r}')$.

Phonon dispersion relations (ω vs. \mathbf{q} relations) come directly from solving the equation above. The eigenvalues $\omega_{\mathbf{q}s}^2$ indicate the phonon frequencies for each phonon mode. The mutually orthogonal

eigenvectors $\mathbf{e}_{i\mathbf{q}s}$ are the polarization vectors, defining the direction of the atom displacement at site \mathbf{r} as the atom participates in the phonon mode indexed by $\mathbf{q}s$. Two dispersion relation quantities which will be referenced throughout this thesis are the group (v_g) and phase velocity (v_p). Noting that phonons travel through a solid by forming wave packets, the group velocity refers to the velocity of these wave packets and the phase velocity refers to the velocity of the phase fronts within the wave packet. They are defined from the phonon frequency and wavevectors as follows:

$$(2.7) \quad \begin{aligned} v_{p,i} &= \omega/q_i \\ \mathbf{v}_g(\mathbf{q}s) &= \nabla_{\mathbf{q}}\omega \end{aligned}$$

Near the Γ point, the group and phase velocity should converge in value, however, they may deviate slightly in terms of direction [27]. The group velocity indicates the direction of heat travel, which may deviate from the wavefront propagation direction (see Section 5.4.2.2).

In the following subsections, we will first discuss common approximations made to the phonon dispersion which facilitate the development of analytic models (Section 2.1.1). We will define two additional quantities within the harmonic potential approximation: the density of states (Section 2.1.2) and the spectral heat capacity (Section 2.1.3). Finally, anharmonic terms in the potential energy will be included as a perturbation to the phonons derived here, which will lead to interactions between phonon modes (Section 2.2.1).

2.1.1. Phonon Dispersion Approximations

Analytic expressions for thermal transport properties, which are emphasized in this thesis, typically require approximating the full phonon dispersion using a closed-form expression. Two of the most common dispersion approximations are the Debye and Born von Karman models. The Debye, or linear dispersion, uses the classical speed of sound (v_s) as a proportionality constant between frequency and wavevector. The maximum vector written in terms of the average atomic volume would be equal to $q_{\max} = (\frac{6\pi^2}{V_0})^{1/3}$, and the maximum frequency (also referred to as the Debye

frequency ω_D) is simply defined as $\omega_D = v_s k_{\max}$. Finally, the Debye temperature $\theta_D = \hbar\omega_D/k_B$ is the temperature at which all phonon modes are excited. Successes of the Debye model have included predicting the T^3 dependence of the low-temperature heat capacity [28]. Generally, it is a more suitable model for low-frequency, long-wavelength phonons (those that dominate at low T), which coarsen over the atomistic structure of the material and propagate at the classical speed of sound. Additional isotropic approximations are made such that phonons lose dependence on crystallographic direction, and further, that phonons of different polarization have the same Debye frequency [29].

The Debye approximation is a non-dispersive model, as the slope of the ω - q relation is fixed as the classical speed of sound ($v_s = d\omega/dq|_{q \rightarrow 0}$). In contrast, the Born von Karman (BvK), or sinusoidal approximation, is a modification of the continuum Debye model to include dispersion of the phonon modes [29]. The BvK model uses the expression $\omega = \frac{2}{\pi}v_s q_{\max} \sin(\frac{\pi q}{2q_{\max}})$ with q_{\max} defined as before from the average atomic volume (V_0). The group velocity is then $v_g = v_s \cos(\frac{\pi q}{2q_{\max}})$ [30].

Finally, it is common to approximate the flat, optical branch using the Einstein model, which requires treating atoms as independent harmonic oscillators leading to a flat ω vs. q relation. Here, heat is conducted diffusively between atoms, which is captured by models for glass-like conduction presented by Cahill [31], Clarke [32], and Agne [33]. Therefore, a final dispersion approximation can be constructed by treating the acoustic branch using the Debye or Born von Karman approximation and treating the optical branch as flat Einstein modes, which carry a minimum thermal conductivity [19]. Each optical branch is described by a constant frequency ω , defined by the max frequency of the acoustic branch in an extended zone scheme: $\omega(q_{\max})$ for $q_{\max} = (\frac{6\pi^2}{nV_0})^{1/3}$ with $n = (N - 1), (N - 2), \dots, 1$. Figure 2.1 compares the three dispersion approximations discussed (i.e. Debye, Born von Karman, and Debye + Einstein) to the full phonon bandstructure for the half-Heusler compound, HfNiSn.

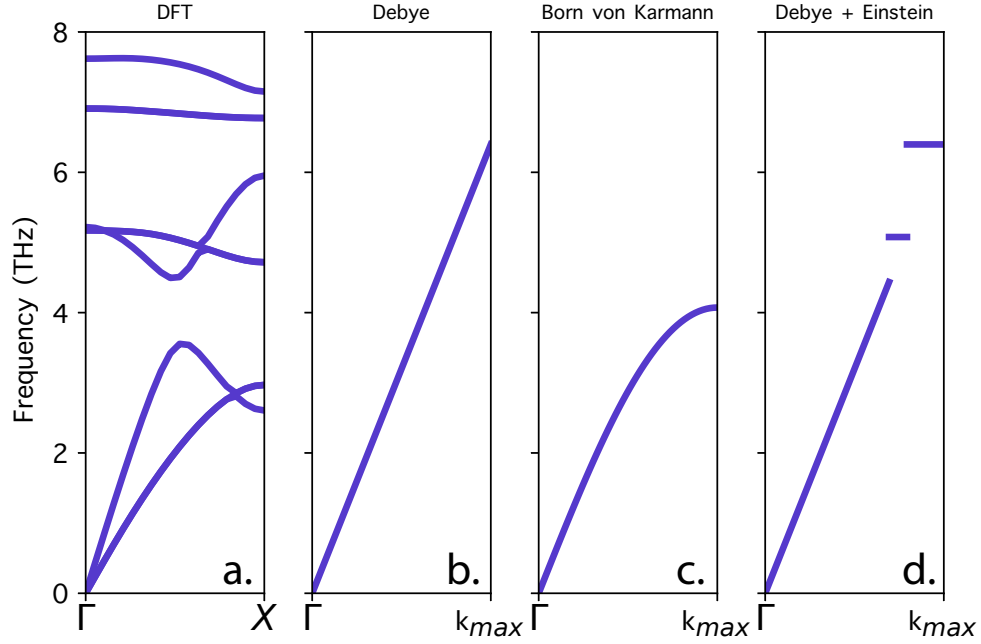


Figure 2.1. **Schematic of Dispersion Approximations** Comparison of phonon dispersion approximations for half-Heusler compound, $HfNiSn$. In comparison to the full phonon dispersion (a), the Debye model (b) uses the constant classical speed of sound, which assigns a large phonon velocity even to relatively flat optical modes. The Born von Karman dispersion (c) corrects for this by having the group velocity approach 0 at the zone edge using a sinusoidal form. Finally, the hybrid Debye + Einstein model (d) uses separate functional forms to treat the acoustic branch as propagating phonons and optical branches as localized Einstein modes, which couple to one another. A Born von Karman + Einstein model can also be used to describe the acoustic branch.

2.1.2. Phonon Density of States

The density of the normal mode states, or the number of states dN per frequency interval $d\omega$, is a crucial quantity in lattice dynamics and thermal transport. Here, we will derive the 3D phonon density-of-states, although we will show in latter sections that the 1D and 2D density-of-states also play an important role in defect scattering problems. For a solid of dimensions $L \times L \times L$, each mode \mathbf{q} occupies a volume of $(2\pi/L)^3$. If we can assume that phonon states fill up a sphere in \mathbf{q} -space, the resulting dependence of N on the magnitude of q is: $N = (L/2\pi)^3 (\frac{4}{3}\pi q^3)$. The volumetric 3D density of states is then given by the following expression, including a factor of 3 for the degeneracy of each phonon mode:

$$\begin{aligned}
(2.8) \quad g(\omega) &= 3 \frac{1}{L^3} \frac{\partial N}{\partial q} \frac{\partial q}{\partial \omega} \\
&= 3 \frac{q^2}{2\pi^2} \frac{1}{v_g} = \frac{3}{2\pi^2} \frac{\omega^2}{v_p^2 v_g}
\end{aligned}$$

The 1D and 2D density of states can be derived using the same strategy, by viewing phonon modes as filling up a line or circle in q -space, instead. As a result, the 1D density-of-states will be a constant with respect to frequency and the 2D density-of-states will vary as ω .

2.1.3. Heat Capacity

Within the harmonic approximation, the lattice does not experience thermal expansion and it is natural to define the heat capacity in the constant volume approximation. The heat capacity is the temperature derivative of the energy density at constant volume, resulting in the following expression in terms of the phonon density-of-states ($g(\omega)$) and the Bose-Einstein distribution ($f_{\text{BE}} = 1/(\exp(\hbar\omega/k_{\text{B}}T) - 1)$):

$$\begin{aligned}
(2.9) \quad C(\omega) &= \hbar\omega g(\omega) \frac{\partial}{\partial T} \frac{1}{e^{\hbar\omega/k_{\text{B}}T} - 1} \\
&= \frac{3\omega^4}{2\pi^2 v_g(\omega) v_p^2(\omega)} \frac{\hbar^2}{k_{\text{B}} T^2} \frac{e^{\hbar\omega/k_{\text{B}}T}}{(e^{\hbar\omega/k_{\text{B}}T} - 1)^2}
\end{aligned}$$

It is informative to then study the behavior of C at the low- and high-temperature limits, and, to do so, it is common to define the variable $x = \hbar\omega/k_{\text{B}}T$. Focusing first on the high-temperature limit ($T \gg \theta_{\text{D}}$ and $x \rightarrow 0$), we can use the power series representation of e^x in the limit of small x to suggest that $e^x \approx 1 + x$. Through straightforward manipulation of Equation 2.9, we find that the high-temperature spectral heat capacity is simply the density of states weighted by the Boltzmann coefficient:

$$(2.10) \quad C_{\text{HT}}(\omega) = k_{\text{B}}g(\omega).$$

The volumetric heat capacity at a given temperature T is then simply the integral of $C(\omega)$ over the full frequency spectrum. Since $\int g(\omega)d\omega = 3n$, where n is volumetric density of atoms in the system, we see that C_{V} converges to $3nk_{\text{B}}$ at high temperature, also known as the Dulong-Petit limit.

For simplicity, we will discuss these low-temperature limit using the Debye approximation to the phonon dispersion, introduced in Section 2.1.1. It is reasonable to do so because the Debye model will match the true phonon dispersion for very low frequency phonons (which characterize the low temperature limit). The integration of spectral heat capacity is shown here explicitly with $x = \hbar\omega/k_{\text{B}}T$ as the integration variable:

$$(2.11) \quad C_{\text{V}} = \frac{9k_{\text{B}}}{V_0} \left(\frac{T}{\theta_{\text{max}}} \right)^3 \int_0^{x_{\text{max}}} \frac{x^4 e^x}{(e^x - 1)^2} dx$$

At very low temperature ($T \ll \theta_{\text{D}}$ and $x_{\text{D}} \rightarrow \infty$), the integral converges to a constant value: $4\pi^4/15$, yielding a heat capacity of [34]:

$$(2.12) \quad C_{\text{V}} = \frac{12\pi^4}{5} \frac{k_{\text{B}}}{V_0} \left(\frac{T}{\theta_{\text{D}}} \right)^3$$

The $C_{\text{V}} \propto T^3$ relation at low temperatures has been verified experimentally, and was one of the earliest successes of the Debye model.

Here, we have focused on phononic contributions to the heat capacity, and in this thesis, we will use the expressions defined in this section when defining the heat capacity. However, there are scenarios in which additional contributions to the heat capacity become highly important. One of the most straightforward is the thermal expansion that occurs in any real (anharmonic) solid.

However, there may additionally be contributions from free electrons and latent heat from phase transformations [35].

2.1.4. Anharmonic Coefficient: the Grüneisen Parameter

The final quantity commonly used in thermal transport is the Grüneisen parameter, which quantifies anharmonic effects in a solid. An unfortunate attribute of the Grüneisen parameter is that it is presented in many different forms. Here, we will introduce the most generalized representation as a tensor quantity, which captures the strain (ϵ_{ij}) dependence of the frequency (ω) for a specific phonon mode indexed by \mathbf{qs} :

$$(2.13) \quad \gamma_{ij}(\mathbf{qs}) = -\frac{1}{\omega} \frac{\partial \omega}{\partial \epsilon_{ij}}$$

Since the Grüneisen parameter describes the perturbation to phonon energies due to strain or lattice distortions, it will be an important quantity in both phonon-strain and phonon-phonon scattering interactions. The Grüneisen parameter can also be determined from the third order force constants, often evaluated using density functional theory [36].

2.2. Phonon Scattering Theory

As discussed in the lattice dynamics section (Section 2.1), phonons are strictly defined within the harmonic approximation, as the dynamical matrix is specified from the mass-normalized Fourier transform of second order force constants. Any deviation to this periodic, harmonic model would perturb the phonon states, leading to finite coherence length and lifetime.

In this section, we will discuss common lattice effects which scatter phonons and lead to the diffusive heat transport commonly observed. First, there are a few key characteristics often used to codify scattering events. The first major distinction is between *harmonic* and *anharmonic* scattering. Anharmonic scattering essentially utilizes the 3rd order, anharmonic term in the Taylor expanded interatomic potential. The perturbation Hamiltonian for anharmonic scattering will

involve three displacement vectors (\mathbf{u}), which can be dynamic in nature (phonons) or static (internal strain) [37–39]. Anharmonic scattering will therefore primarily describe either phonon-phonon or phonon-strain interactions. By contrast, the perturbation Hamiltonian for harmonic scattering will involve only two displacement vectors \mathbf{u} for the incident and final phonon state. Harmonic scattering tends to emerge from perturbations to the 2nd order, harmonic potential energy term or the kinetic term of the lattice energy. Static imperfections, such as mass defects, typically result in harmonic scattering.

In contrast, the distinction between *elastic* and *inelastic* scattering has more to do with the conserved quantities in the phonon scattering process. Inelastic scattering occurs when energy is exchanged between the incident phonon and the scatterer, such that energy and momentum are not conserved between the initial and final phonon states, which are requirements of elastic scattering. For inelastic scattering to occur, the scatterer must contain the adequate dynamical degrees of freedom to absorb or emit the energy of a phonon. Perhaps the most straightforward instance of inelastic scattering is when the origin of the scattering is, itself, another phonon in the system. In such phonon-phonon interactions, the anharmonicity of the lattice gives rise to this form of inelastic scattering. However, the two need not always occur hand-in-hand. Scattering from a static strain field (discussed in detail in Section 5.2) is an example of an anharmonic scattering potential, which lacks dynamical degrees of freedom and leads to elastic scattering.

2.2.1. Phonon-Phonon Interactions

Before discussing the influence of lattice defects, it is important to describe the phonon scattering effects which limit thermal transport in a pristine, single crystal. Although the phonons derived in Section 2.1 should be non-interacting normal modes, this picture breaks down in real materials with interatomic potentials that are not fully harmonic. The higher order terms in the lattice potential cause phonons to interact with one another, yielding thermally resistive scattering events. Typically, scattering processes involving just three phonons (referred to as 3-phonon processes) are sufficient to describe the thermal transport in a material. However, in certain cases 4-phonon

processes have been shown to yield large scattering rates [40], which greatly influence the expected thermal conductivity of a compound. A notable example is BAs, a compound with an unusually large acoustic-optical bandgap. The energy distribution of phonon states is such that the number of allowed 3-phonon interactions is very limited, but 4-phonon interactions are more prevalent than in typical compound semiconductors [41–43].

Interactions involving three phonon modes should have one of two basic configurations: 1) a *decay* process in which an incident phonon divides into two final phonon states or 2) a *collision* process in which two incident phonons combine into a single final phonon state. Either case requires a conservation of the total energy. For an example *decay* process, the energy conservation might be:

$$(2.14) \quad \hbar\omega_1 = \hbar\omega_2 + \hbar\omega_3$$

Three-phonon interactions are further categorized as either normal (described as momentum-conserving) and umklapp (described as non-momentum-conserving). It is common to consider normal processes as non-resistive processes such that only the umklapp scattering should impact the overall phonon lifetime. More specifically, the momentum conservation for a normal process is:

$$(2.15) \quad \mathbf{q}_1 - \mathbf{q}_2 - \mathbf{q}_3 = 0,$$

while the momentum conservation for an umklapp process is:

$$(2.16) \quad \mathbf{q}_1 - \mathbf{q}_2 - \mathbf{q}_3 = \mathbf{G},$$

where \mathbf{G} is a reciprocal lattice vector. Therefore, the umklapp process involves an “exchange” of crystal momentum (which emerges from the periodicity of the lattice) in units of \mathbf{G} . However, as noted by Maznev *et al.* [44], phonons, being defined from a periodic potential and obeying Bloch’s

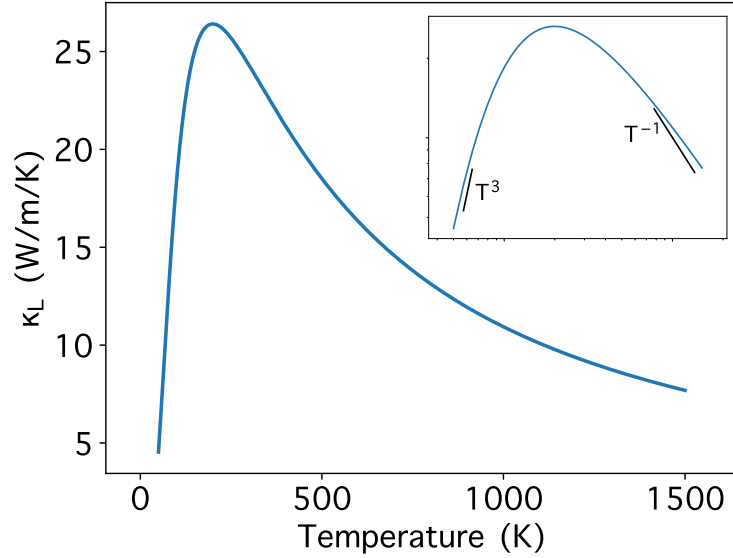


Figure 2.2. **Lattice Thermal Conductivity Trends with Temperature** Plot inset shows the log-log trend to highlight temperature dependencies at the low- and high-temperature regimes. At the low-T limit, κ_L varies as T^3 , stemming from the heat capacity. A rollover occurs, characterized by the onset of resistive phonon-phonon scattering processes. Finally, beyond the Debye temperature, $\kappa_L \propto T^{-1}$, stemming from the phonon-phonon relaxation time.

theorem have a wavevector defined modulo \mathbf{G} such that \mathbf{q} is equivalent to $\mathbf{q} + \mathbf{G}$. The normal vs. umklapp distinction, instead, mostly depends on whether the phonon interaction is contained within a single primitive cell of the reciprocal lattice. The cut-off between the two scattering types is therefore not uniquely defined, as it depends on the choice of the primitive cell. Subsequent works have shown that both interaction types are, in fact, important to modelling thermal conductivity. Therefore, while we may use the distinction between *normal* and *umklapp* to highlight differences in conservation criteria, it is important to note the limits in the definition and that the more general classification of “phonon-phonon scattering” is the most cleanly defined. At room temperature and above, *umklapp* processes tend to dominate in thermoelectric materials, so in later sections, we will only use the more general case in which an exchange of reciprocal lattice vector \mathbf{G} is permitted in the momentum conservation.

The analytic expression for lifetime in the case of phonon-phonon scattering depends on frequency as ω^2 and temperature as T^{-1} (since phonon occupancy increases with temperature) [19, 45, 46].

$$(2.17) \quad \tau_{\text{pp}} = \frac{(6\pi^2)^{1/3}}{2} \frac{\overline{M}v_s^3}{k_B\omega^2V^{1/3}\gamma^2} \exp(\theta_D/3T)T^{-1}$$

The exponential term reflects the onset of *umklapp* processes, which tend to dominate once high frequency phonons are excited in the vicinity of the Debye temperature. Equation 2.17 above is defined within the Debye approximation, in which the phonon velocity is a constant, equal to the classical speed of sound. The factor of ω^2/v_s^3 in the inverse lifetime, or scattering rate, is reminiscent of the 3D phonon density-of-states. In the more general derivation of the phonon-phonon relaxation time (Appendix B.2), it is evident that this factor instead represents a 2-phonon, or joint density-of-states, representing all the allowed phonon-transitions when the energy and momentum conservation criteria listed above are satisfied [47].

2.2.2. Perturbation Theory of Phonon-Defect Scattering

The basis of the defect scattering theory discussed here is Fermi's Golden Rule. To the first order in perturbation theory, Fermi's Golden Rule states that the scattering probability ($W_{\mathbf{q},\mathbf{q}'}$) from an initial state \mathbf{q} to final state \mathbf{q}' is directly related to the squared scattering matrix element $\langle \mathbf{q} | H' | \mathbf{q}' \rangle^2$, a measure of the overlap between the states, facilitated by the lattice perturbation. Additionally, the momentum and energy conservation constraints are enforced separately, using Dirac delta function conditions:

$$(2.18) \quad W_{\mathbf{q},\mathbf{q}'} = \frac{2\pi}{\hbar^2} |\langle \mathbf{q} | H' | \mathbf{q}' \rangle|^2 \delta(\omega_{\mathbf{q}} - \omega_{\mathbf{q}'}).$$

However, it is more straightforward to describe static lattice defects in real space, using defect site fractions and real space displacement fields. The scattering potential defined from the real-space lattice perturbation induced by the defect is denoted as $V(\mathbf{r})$. In the Born approximation, the scattering matrix element can be written in terms of a scattering vector $\mathbf{Q} = \mathbf{q}' - \mathbf{q}$, and requires taking the Fourier transform of $V(\mathbf{r})$. Here, we will consider a crystallite containing the defect,

which has dimensions of $L_x \times L_y \times L_z$ and a volume of $V_{\text{tot}} = L_x L_y L_z$. This choice of crystallite dimensions will not, however, influence the final solutions, which will be based only on intensive properties.

$$(2.19) \quad \langle \mathbf{q} | H' | \mathbf{q}' \rangle = \frac{1}{L_x L_y L_z} \iiint d^3r V(\mathbf{r}) e^{i\mathbf{Q} \cdot \mathbf{r}} = \frac{1}{L_x L_y L_z} |\tilde{V}(\mathbf{Q})|$$

Substituting this expression for $\langle \mathbf{q} | H' | \mathbf{q}' \rangle$ into the scattering probability equation, we get the following expression:

$$(2.20) \quad W_{q,q'} = \frac{2\pi}{\hbar^2} \frac{1}{(V_{\text{tot}})^2} |\tilde{V}(\mathbf{Q})|^2 \delta(\omega_{\mathbf{q}} - \omega_{\mathbf{q}'}).$$

The final derivation of a scattering, or inverse phonon lifetime τ^{-1} , requires integrating over all possible final phonon states when restrictions in frequency and momentum conservation are considered.

$$(2.21) \quad \tau^{-1} = \frac{V_{\text{tot}}}{(2\pi)^3} \iiint W_{\mathbf{q},\mathbf{q}'} d^3\mathbf{q}'$$

The final expression for the scattering rate is inversely related to the volume of the region containing the defect, or put more simply, related to the spatial density of defects in the system. The expression is additionally related to the phase space, or all final states available to scatter into once energy and momentum conservation criteria have been satisfied. Given the restriction of $\Delta\omega = 0$ for elastic defect scattering, the phase space should relate to the phonon density of states at ω .

Such physical insights into the defect scattering rate, allowed Hanus *et al.* [22] to introduce a modified form of Fermi's Golden Rule, which is more physically interpretable for defect scattering problems, and is particularly instructive when comparing defects of different dimensionalities. Here, the scattering rate $\Gamma(\mathbf{q})$ for an incident phonon state \mathbf{q} is:

$$(2.22) \quad \Gamma(\mathbf{q}) = \tau^{-1}(\mathbf{q}) = n_d |S|^2 g(\omega_{\mathbf{q}}),$$

where n_d is the spatial density of defects, $|S|^2$ is an averaged squared scattering matrix element, and $g(\omega_{\mathbf{q}})$ is the phase space available to scatter into once necessary energy and momentum conservation constraints have been met. $|S|^2$ is then defined by taking the integral over $\tilde{V}(\mathbf{Q})$ for all final phonon trajectories. The weighting factor $(1 - \hat{\mathbf{q}} \cdot \hat{\mathbf{q}}')$ suppresses any non-resistive forward scattering processes which should not contribute to the scattering rate. Finally, A is a numerical prefactor that varies slightly depending on the defect geometry [22].

$$(2.23) \quad |S|^2 = A \iiint d\Omega' |\tilde{V}(\mathbf{Q})|^2 (1 - \mathbf{q} \cdot \mathbf{q}')$$

The frequency-dependence of the relaxation time, which is often used as a signature of the dominant scattering effects, mainly comes from the $|S|^2$ and $g(\omega)$ terms. Figure 2.3 summarizes the frequency contributions for mass defects (i.e. change in the atomic mass) with different dimensionalities (i.e. point, line, or planar defects). The phase space term changes for each defect dimensionality shown. In point defect scattering, only phonon frequency is conserved, such that an incident phonon with frequency ω may scatter into the 3D phonon density of states ($g_{3d}(\omega)$). A one-dimensional line defect additionally conserves a component of the momentum along the sense vector, yielding a phase space term equal to the 2D density of states. Finally, the planar defect conserves two components of momentum, which span the plane, such that the phase space is equal to the 1D phonon density of states.

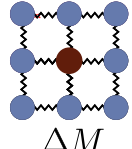
2.2.3. Matthiessen's Rule

The thermal and electronic transport properties discussed in this work will heavily leverage Matthiessen's rule to combine different scattering effects. Matthiessen's rule states that total scattering rate can be written as the sum of scattering rates due to different lattice perturbations, including phonons,

$$\tau^{-1} = n_d |S|^2 g(\omega)$$

Any mass defect (ΔM)

0D : $\mathbf{r}(x, y, z)$, 1D : $\mathbf{r}(x, y)$, 2D : $\mathbf{r}(x)$



$$V(\mathbf{r}) = \frac{1}{2} \frac{\Delta M}{M} A_0 \hbar \omega \delta(\mathbf{r})$$

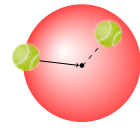
ΔM

$$|S|^2 = \frac{2\pi}{\hbar^2} \int d\Omega' |\tilde{V}(\mathbf{Q})|^2 (1 - \mathbf{q} \cdot \mathbf{q}')$$

$$|S|^2 \propto \left(\frac{\Delta M}{M}\right)^2 A_0^2 \omega^2$$

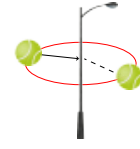
0D defect

$g_{3d} \propto \omega^2$



1D defect

$g_{2d} \propto \omega$



2D defect

$g_{1d} \propto \omega^0$

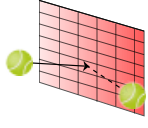


Figure 2.3. **Defect Dimensionality and Fermi's Golden Rule** The main components of Fermi's Golden Rule for defects are the number density of defects (n_d), the volume containing the defect (V_d), the squared scattering matrix element ($|H'|$), and the phase space for the scattering transitions ($g(\omega)$). The last two terms contribute frequency dependencies. The defect dimensionality influences the momentum conservation and thus the available phase space. In contrast, the squared matrix element is expected to be proportional to ω^2 for any defect dimensionality.

impurities, or boundaries. This rule carries the assumption that these various scattering effects act independently of one another, i.e. their scattering probabilities are not conditionally dependent. For example, a typical thermal model of a defective, anharmonic system will include the following terms in the total scattering rate: 1) phonon—phonon, 2) phonon—point-defect, 3) phonon—dislocation, and 4) phonon—grain-boundary interactions. Combined using Matthiessen's rule, this yields:

$$(2.24) \quad \tau^{-1} = \tau_{pp}^{-1} + \tau_{PD}^{-1} + \tau_{disl}^{-1} + \tau_{GB}^{-1} + \dots$$

2.3. Calculating Transport Coefficients

2.3.1. Phonon Gas Model

Within the phonon gas model framework, phonons are treated like gas molecules which carry energy of $\hbar\omega$. Thermal transport coefficients can then be derived by drawing inspiration from the kinetic theory of gases [48, 49]. We should note that more formal descriptions of thermal conductivity, derived from the phonon Boltzmann Transport Equation, all converge to the kinetic theory expression (see derivation in Appendix A) [45, 46, 50].

We can start with Fick's first law, describing isothermal particle diffusion, where the driving force for particle flux comes from a gradient in the concentration (n).

$$(2.25) \quad \mathbf{J} = -D\nabla n$$

If in this system, particles travel ballistically with a well-defined velocity v over an average distance equal to the mean-free-path l between collisions. Taking the isotropic approximation (i.e. travel in any direction is equally likely) the diffusivity in this system is then equal to:

$$(2.26) \quad D = \frac{1}{3}vl.$$

By analogy, one can write a phenomenological law for thermal transport based on the gradient in energy density (u) [48]. For simplicity, we'll use the one-dimensional form for a heat flux and energy density gradient along the x direction, relating the energy density gradient then to the temperature gradient across the sample:

$$(2.27) \quad \mathbf{J}_x = -D_{xx} \frac{du}{dx} = -D_{xx} \frac{\delta u}{\delta T} \frac{\delta T}{\delta x}.$$

The value of $\frac{\delta u}{\delta T}$ is simply the heat capacity C (Section 2.1.3). Fourier's law of heat conduction then states that the heat flux is proportional to the negative temperature gradient, where the constant of proportionality is the thermal conductivity κ :

$$(2.28) \quad \mathbf{J}_x = -\kappa_{L,xx} \frac{dT}{dx}.$$

Relating this expression to its chemical analogue, Fick's law (Equation 2.27), the thermal conductivity must equal:

$$(2.29) \quad \kappa_{L,xx} = \frac{1}{3} C v_{g,x} l_x = \frac{1}{3} C v_{g,xx}^2 \tau,$$

where the mean-free-path can, alternatively, be defined as the phonon velocity times the lifetime τ . It is common to express the $\kappa_{L,xx}$ as an integral over all phonon frequencies ω hosted by the lattice, of the spectral quantities for C , v , τ as shown in Figure 2.4. Intuitively, the components of the thermal conductivity include the amount of heat carried by phonon in the frequency integral $d\omega$ (as captured by $C(\omega)$), how quickly they propagate through the lattice ($v_g^2(\omega)$), and how long they travel between scattering events ($\tau(\omega)$).

$$(2.30) \quad \kappa_L = \frac{1}{3} \int_0^{\omega_{\max}} C(\omega) v_g^2(\omega) \tau(\omega) d\omega$$

A pitfall of this formalism is that it requires a well-defined phonon velocity, which flat, optical modes tend to lack [51, 52]. In complex unit cell or amorphous materials, these flat, spatially localized vibrational modes can predominate the thermal transport leading to significant breakdowns of the phonon gas model. The spatial localization and lack of plane wave character of these vibrational modes, leads them to be termed *diffusons* rather than propagating phonons. More akin to the Einstein model of lattice vibrations, these diffuson modes may transport heat through the random hopping mechanism. Vibrational modes that are so localized that they are tethered to an

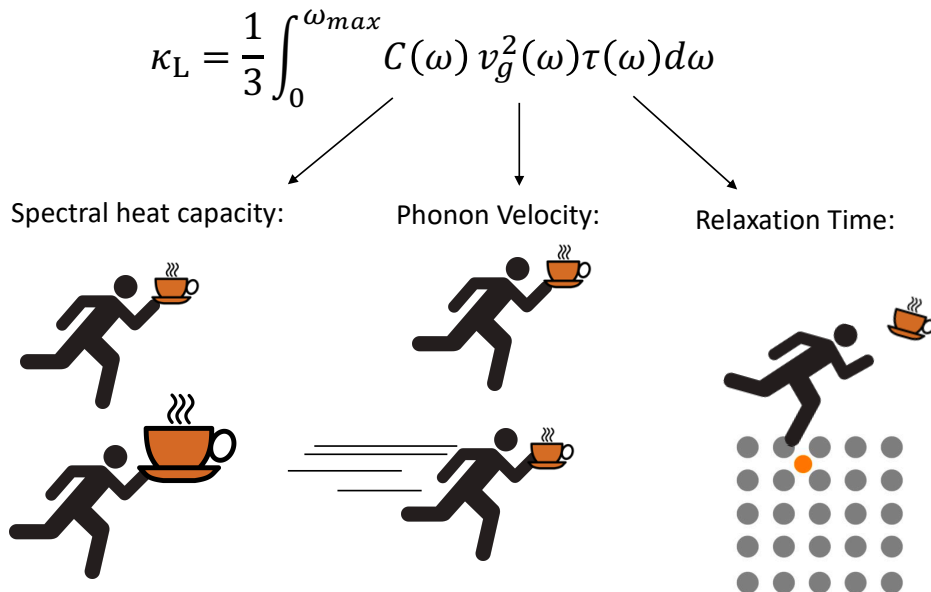


Figure 2.4. **Phonon Gas Model Schematic** In the phonon gas model, the thermal conductivity can be written as an integral over the phonon spectrum, where the heat carried by the phonons in each frequency integral is determined by the amount of heat they carry (spectral heat capacity; $C(\omega)$), the velocity of the phonons (spectral group velocity; $v_g(\omega)$), and the time the phonon travels between scattering events (spectral lifetime; $\tau(\omega)$).

atom site and do not transport heat at all are instead termed *locons*. There has been a great deal of recent focus in the development of a diffusion coefficient expression based on quantum particle attributes that are still well-defined in this regime, including frequency and even lifetime. Agne *et al.* developed such an expression from the standpoint of random walk theory:

$$(2.31) \quad D(\omega) = \alpha^2 \frac{N}{t},$$

where α is the jump distance (usually the interatomic distance) and N/t is then number of jumps per unit time. Einstein suggested that each oscillator makes two jump attempts per period, such that $N/t = \frac{2\omega}{2\pi} P$ with P representing the probability of a successful jump. In Section 3.5, we will

discuss diffuson transport in the context of highly disordered materials and its role in estimates of the minimum thermal conductivity supported by a material.

In this thesis, we focus on lattice thermal conductivity frameworks from the standpoint of lattice dynamics, with the requisite phonon properties C , v_g , and τ defined either for a given phonon mode \mathbf{q} or for a given frequency interval $d\omega$ from a phonon dispersion, be it DFT-derived or from an approximation discussed in Section 2.1.1. An alternative approach is molecular dynamics, in which real-space atom displacements and velocities are used to define the heat transport. The heat flux (first derived by Hardy [53]) in a simulation defined by pairwise potentials will be equal to [54]:

$$(2.32) \quad \mathbf{j} = \frac{1}{V} \sum_i \epsilon_i \mathbf{v}_i + \sum_{i,j \neq i} (\mathbf{F}_{i,j} \cdot \mathbf{v}_j) \mathbf{r}_{ij},$$

where ϵ_i is the total energy (kinetic and potential) of atom i , \mathbf{v}_i is the velocity of atom i , \mathbf{F}_{ij} is the interatomic force and \mathbf{r}_{ij} is the separation between atoms i and j . The Green-Kubo formalism is based on the fluctuation-dissipation theorem and relates the lattice thermal conductivity to the time correlation of the heat fluxes:

$$(2.33) \quad \kappa = \frac{1}{Vk_{\text{B}}T} \int_0^\infty \langle \mathbf{j}(0) \cdot \mathbf{j}(t) \rangle dt.$$

This time-correlation approach can have major benefits over the phonon gas model when phonon velocities are ill-defined, such as in highly disordered materials and complex unit cell materials, common in the field of thermoelectrics [51]. However, interpreting these simulations can become a challenge since post processing or controlled wave packet simulations [55] must be performed to extract mode specific properties. We will discuss the Green Kubo formalism in the context of specific phonon scattering problems, such as the calculation of a thermal boundary resistance in Section 5.3.2.

CHAPTER 3

Phonon–Point-Defect Scattering**3.1. Introduction: Approaches to Point Defect-Phonon Scattering**

Point defects are ubiquitous in the engineering of materials, often as a route to tailor properties like strength or charge carrier concentration. These point defects are known to scatter vibrational modes and impact the thermal conductivity, which can be especially important in thermoelectrics, microelectronics, and thermal barrier coatings.

Klemens established a theory for vibrational mode scattering due to static imperfections in a lattice, and provided closed-form expressions for thermal conductivity versus defect concentration still utilized today [56–58]. These analytical expressions based on low order perturbation theory are useful for routine interpretation of experimental results to determine the dominant phonon scattering sources in a material. By calculating the relative contribution of independent scattering mechanisms such as mass disorder and local strain effects, one can determine the dominant mechanisms of scattering in a defective system to guide the design of thermal materials [59–62].

First-principles techniques have been developed recently to compute the impact of point defects on thermal transport. These simulations have shown very good quantitative agreement with experiments for a range of materials and have provided useful insights regarding the mechanisms of phonon-defect scattering [63, 64]. However, multiple calculations are required to compute defect structures, evaluate scattering strengths, and solve the Boltzmann transport equation for the thermal conductivity [65–68]. Often, these techniques are too expensive and system dependent for routine modelling used to determine the dominant scattering mechanisms in a system [69]. While the first-principles methods are essential to understanding vibrational mode properties, and in many cases elucidate limitations of analytical phonon theories, the Klemens point defect model

has proven to be highly descriptive across material systems and therefore continues to be widely used [67, 69–71].

The Klemens equations are defined within the ostensibly limiting approximation of a single atom unit cell and the Debye model, or linear phonon dispersion (see Section 2.1.1). However, by comparing to both first-principles results as well as experiment, the predictive quality of this model is demonstrated even for complex unit cell materials.

This chapter provides a functional guide for understanding the influence of point defects on phonon transport and applying the Klemens equations to model thermal conductivity data. We start by presenting the lattice perturbation due to point defects using the framework presented in Section 2.2.2 and deriving a phonon scattering rate due to point defect interactions. We then present a more generalized and conceptually clear expression for the scattering strength due to point defects in a multiatomic lattice. Section 3.3.1 resolves discrepancies between popular representations of the mass difference model, which have led to consistent errors in model inputs that may yield large factor differences in the predicted lattice thermal conductivity (κ_L). This section also re-evaluates whether these expressions are limited to the Debye model dispersion. A mechanism is demonstrated for how the model’s sensitivity to dispersion relation is, in practice, lifted, justifying the use of the model in systems with arbitrary dispersion relations. The previous literature discrepancies may obscure the exceptional scattering strength of off-stoichiometric defects such as vacancy and interstitial sites, which are discussed in Section 3.3.3. In Section 3.4 we highlight the impact that phonon-dopant interactions have on the thermoelectric figure-of-merit using the full-Heusler VFe_2Al as an example. Finally, we revisit the breakdown of the phonon paradigm at the highly disordered limit in Section 3.5.

3.2. Lattice Perturbation Due to Point Defects

In this section, we will focus on a mass defect (following the convention of Klemens [56]), in which the perturbation stems from an atom with a mass of $M' = M_0 + \Delta M$ sitting at site \mathbf{R} . The perturbation due to force constant fluctuation and strain are similar in form. The real-space

energy perturbation ($E'(\mathbf{R})$) to the lattice due to mass difference comes in through the kinetic energy term, where $\dot{\mathbf{u}}(\mathbf{R})$ signifies the time derivative of the unit cell displacement.

$$(3.1) \quad E'(\mathbf{R}) = \frac{1}{2} \Delta M(\mathbf{R}) \dot{\mathbf{u}}^2(\mathbf{R})$$

The definition of $\dot{\mathbf{u}}^2(\mathbf{R})$ is written here as a double sum over the normal modes supported by the lattice (i.e. \mathbf{q} and \mathbf{q}') of the normal mode amplitude $A_{\mathbf{q}}$, the element of the polarization vector corresponding to lattice site $\mathbf{e}_{\mathbf{q}}(\mathbf{R})$ (Note: the polarization vector, in this case, is not mass-weighted as in the convention by Dove [25]), and the phase factor. The branch index s is suppressed here for simplicity, and will not impact our overall conclusions.

$$(3.2) \quad \dot{\mathbf{u}}^2(\mathbf{R}) = -\frac{1}{N} \sum_{\mathbf{q}, \mathbf{q}'} A_{\mathbf{q}} A_{\mathbf{q}'} \omega_{\mathbf{q}} \omega_{\mathbf{q}'} [\mathbf{e}_{\mathbf{q}}(\mathbf{R}) \cdot \mathbf{e}_{\mathbf{q}'}(\mathbf{R})] \exp(i[(\mathbf{q} + \mathbf{q}') \cdot \mathbf{R} - (\omega_{\mathbf{q}} + \omega_{\mathbf{q}'})t])$$

In this double sum, terms $\mathbf{q} = -\mathbf{q}'$ produce a shift in phonon frequencies, resulting in the following change in vibrational energy per lattice site, where N is the number of sites in the lattice:

$$(3.3) \quad \Delta E = \frac{1}{2N} \frac{\Delta M}{M} E$$

In the original work by Klemens, terms of this form were neglected because they did not describe transitions between different phonon modes. However, following the approach described in Section 2.2.2, ΔE determines the scattering potential, which for a point defect, should be centered on the defect site. Therefore $V(\mathbf{R})$ should have the following form (see Figure 2.3):

$$(3.4) \quad V(\mathbf{R}) = \frac{V_0}{2} \frac{\Delta M}{M} \hbar \omega \delta(\mathbf{R})$$

Here, V_0 is the volume per atom such that the $V_0 \delta(\mathbf{R})$ is unitless and therefore $V(\mathbf{R})$ has appropriate units of energy [22]. The calculation of $\tilde{V}(\mathbf{Q})$ is trivial because the Fourier transform of $\delta(\mathbf{r})$ simply

goes to 1 in this case. In order to calculate the phonon lifetime, we then need to calculate the squared scattering matrix element using Equation 2.23 and compute the scattering probability $W_{\mathbf{q},\mathbf{q}'}$ using Equation 2.20.

$$(3.5) \quad W_{\mathbf{q},\mathbf{q}'} = \frac{2\pi}{\hbar^2} \frac{1}{V_{\text{tot}}} \frac{V_0}{V_{\text{tot}}} \frac{V_0}{4} \left(\frac{\Delta M}{M} \right)^2 \hbar^2 \omega^2 \delta(\Delta\omega)$$

Here, V_0/V_{tot} yields a factor of the spatial density of point defects n_d . Finally, we must apply Equation 2.21 to calculate the scattering rate by integrating over all possible final phonon states \mathbf{q}' . Assuming an isotropic phonon distribution and noting that the scattering probability lacks angular dependence, this spherical surface integral is evaluated noting that: (1) $d^3\mathbf{q}' = q'^2 \sin\Theta dqd\Theta d\phi$, (2) $\omega_{\mathbf{q}} = \omega_{\mathbf{q}'} = v_p(\omega)q'$, (3) $\int \sin\Theta dqd\Theta d\phi = 4\pi$, and (4) $\delta(\Delta\omega) = \delta(\Delta k)/v_g(\omega)$.

$$(3.6) \quad \tau_{\text{PD}}^{-1} = \frac{n_d V_0}{4\pi} \left(\frac{\Delta M}{M} \right)^2 \frac{\omega^4}{v_p^2(\omega)v_g(\omega)}$$

The relaxation time has a clear signature of the 3D phonon density-of-states g_{3d} , which is expected given the discussion in Section 2.2.2.

$$(3.7) \quad \tau_{\text{PD}}^{-1} = \frac{n_d V_0 \pi}{6} \left(\frac{\Delta M}{M} \right)^2 \omega^2 g(\omega)$$

The equation above exactly matches those derived in the models of Klemens (Equation 17 of Ref. [56]) and Tamura (Equation 19 of Ref. [72]). See Appendix Chapter B for full derivation by Klemens [56].

3.3. Callaway-Klemens Model of Point-Defect Scattering

The thermal conductivity reduction caused by point defects can be understood as a result of the perturbation of the kinetic energy ($\frac{1}{2}Mv^2$ for each atom) or potential energy ($\frac{1}{2}K\Delta r^2$ for each bond) of the lattice (Figure 3.1). The mass difference on the defect site (ΔM) results in

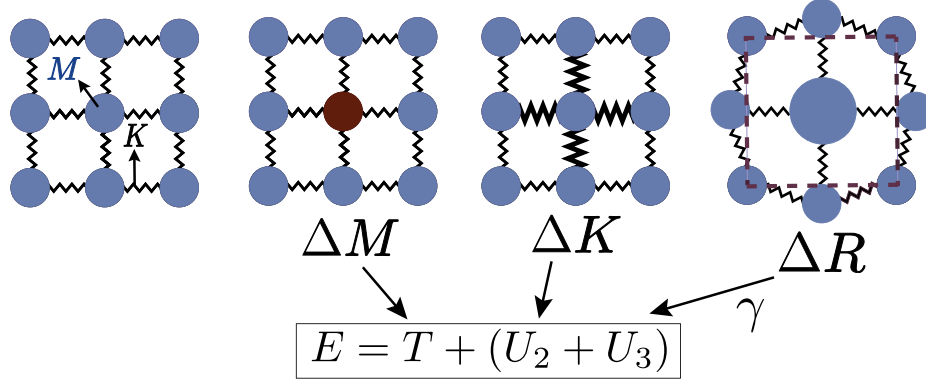


Figure 3.1. **Schematic of Point Defect Perturbations** The lattice perturbation mechanisms of a point defect include a mass difference (ΔM), harmonic force constant difference (ΔK), and strain scattering from site radius difference (ΔR). Each contribution perturbs the lattice Hamiltonian (E) through a different term. T is the kinetic energy of the lattice, and U_2 and U_3 are the harmonic and anharmonic contributions to the lattice potential energy.

the kinetic energy perturbation, while the potential energy distortion is due to both the harmonic force constant difference (ΔK) and a the structural distortion of nearest neighbors around the defect introduced by a site radius difference (ΔR) (see Figure 3.1). It is often the case that mass difference is the dominant effect, since large volume differences are energetically unfavorable for substitutional defects. For simplicity, the remaining equations in this section will be defined first for mass difference scattering alone (Γ_M) with potential energy terms discussed at the end.

The Klemens analytic model predicts the ratio of the defective solid's lattice thermal conductivity to that of a reference pure solid without defects (κ_L/κ_0)(Figure 3.2). This ratio is a function of the disorder parameter u which depends on properties of the pure material: its lattice thermal conductivity (κ_0), elastic properties through its average speed of sound (v_s)¹, the average volume per atom (V_0), as well as a scattering parameter to capture the influence of point defects ($\Gamma = \Gamma_M + \Gamma_K$),

¹Here, the speed of sound acts as a proxy for the Debye frequency. The equation: $\omega_D = (6\pi^2/V)^{1/3}v_s$ can be used to interconvert between the two, where V is the average volume per atom and v_s is the average speed of sound, or $v_s = \left(\frac{1}{3} \left[\frac{1}{v_L^3} + \frac{2}{v_T^3}\right]\right)^{-1/3}$ in terms of the transverse and longitudinal speeds of sound.

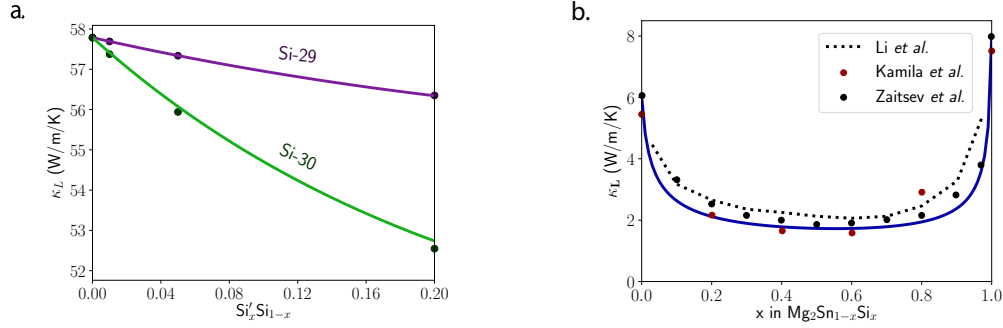


Figure 3.2. **Klemens Model Comparisons to Simulation and Experiment** Thermal conductivity reductions due to point defect scattering for two systems at 300 K: (a) Si based on DFT dispersions and \mathbf{T} matrix scattering theory (points) and the Klemens model (lines) and (b) $\text{Mg}_2\text{Sn}_{1-x}\text{Si}_x$ from experiment (points), \mathbf{T} matrix theory (dotted), and Klemens model (solid) [65, 73, 74]

$$(3.8) \quad \frac{\kappa_L}{\kappa_0} = \frac{\tan^{-1}u}{u} \quad u^2 = \frac{(6\pi^5 V_0^2)^{1/3}}{2k_B v_s} \kappa_0 \Gamma.$$

The Γ_M parameter is the average mass variance in the system ($\langle \overline{\Delta M^2} \rangle$) normalized by the squared average atomic mass ($\langle \overline{M} \rangle^2$) [60, 75–77]. Note that in the notation below, site averages are denoted by a bar while stoichiometric averages are denoted by angular brackets ($\langle \rangle$).

$$(3.9) \quad \Gamma_M = \frac{\langle \overline{\Delta M^2} \rangle}{\langle \overline{M} \rangle^2}.$$

In a compound, these averaged quantities are most easily calculated by treating each component of the compound separately. For example, a generic compound can be expressed with the formula unit: $A1_{c_1}A2_{c_2}A3_{c_3}\dots An_{c_n}$ (e.g. CaZn_2Sb_2), where An refers to the n^{th} component (e.g. Ca, Zn, or Sb) and c_n refers to the stoichiometry of that component (e.g. 1, 2, or 2).

For each site n in the compound, Equation 3.10 gives the average mass variance ($\langle \overline{\Delta M_n^2} \rangle$) and average atomic mass ($\langle \overline{M}_n \rangle$) specifically for that site, which can be occupied by a set of atomic species i , including the host atom and any substitutional defects.

$$(3.10) \quad \overline{\Delta M_n^2} = \sum_i f_{i,n} (M_{i,n} - \overline{M_n})^2 \quad \overline{M_n} = \sum_i f_{i,n} M_{i,n}$$

$\overline{\Delta M_n^2}$ is defined by a sum over i of the species site fraction ($f_{i,n}$) multiplied by the mass variance at each defect site, defined from the species mass $M_{i,n}$ and site average atomic mass $\overline{M_n}$ [78]. In vacancy scattering, where the perturbation emerges from both missing mass (M_{vac}) and missing bonds to nearest neighbors, a virial theorem derivation (see Section 3.3.3) suggests that the mass difference at the vacancy site should be $M_{i,n} - \overline{M_n} = -M_{\text{vac}} - 2\langle \overline{M} \rangle$. Finally, to derive the mass difference scattering parameter Γ_M , the stoichiometric averages of the $\overline{\Delta M_n^2}$ and $\overline{M_n}$ values are taken (Equation 3.9) [78].

$$(3.11) \quad \langle \overline{\Delta M^2} \rangle = \frac{\sum_n c_n \overline{\Delta M_n^2}}{\sum_n c_n} \quad \langle \overline{M} \rangle = \frac{\sum_n c_n \overline{M_n}}{\sum_n c_n}$$

We must then consider the bonding changes and size effects at the defect site. The full perturbation Hamiltonian including mass, bonding, and size effects is:

$$(3.12) \quad H' = \frac{1}{2} \Delta M \left(\frac{d\mathbf{u}(\mathbf{r})}{dt} \right)^2 + \sum_n \left[\frac{1}{2} \Delta K_{\mathbf{b}_n} + \gamma \eta(\Delta R) \right] [\mathbf{u}(\mathbf{r}) - \mathbf{u}(\mathbf{r} - \mathbf{b}_n)]^2.$$

The potential energy perturbation is expanded into the change in harmonic force constant (ΔK) and an anharmonic term with the anharmonic coefficient γ (related to the third order force constant) times the static strain due to a change in site radius ($\eta(\Delta R)$). Here, $\mathbf{u}(\mathbf{r})$ is the displacement at atom site \mathbf{r} through participation in phonon modes. The combined scattering parameter then has the final form below, where Q represents the number of distorted bonds around a point defect, equalling 4.2 for a cubic lattice with a strain field that decays with distance cubed,

$$(3.13) \quad \Gamma_n = \sum_i f_i \left(\frac{\Delta M^2}{\langle \overline{M} \rangle^2} + 2 \left(\frac{\Delta K}{\langle \overline{K} \rangle} - 2Q\gamma \frac{\Delta R}{\langle \overline{R} \rangle} \right)^2 \right) \quad \Gamma = \langle \Gamma_n \rangle$$

Abeles, noting observations in covalent crystal systems that elastic constants varied only with atomic volume, assumed a proportionality between ΔK and ΔR . Therefore, since ΔK is not an intuitive input value, the force constant difference and local strain terms are combined, and both are expressed through the average variance in atomic radius, defined analogously to the mass scattering parameter in Equation 3.10 and Equation 3.9. As before, the atomic radius variance on the n^{th} site is defined from the atomic radius of the i^{th} species which may occupy that site $R_{i,n}$ and the average atomic radius of the site \overline{R}_n . Since the relationships between force constants and atomic volumes are system dependent, these effects are captured in a phenomenological fitting parameter ϵ , which can vary in value between 1-500 in order to fit to experimental data.

$$(3.14) \quad \Gamma = \frac{\langle \overline{\Delta M^2} \rangle}{\langle \overline{M} \rangle^2} + \epsilon \frac{\langle \overline{\Delta R^2} \rangle}{\langle \overline{R} \rangle^2} \quad \langle \overline{\Delta R^2} \rangle = \left\langle \sum_i f_i (R_{i,n} - \overline{R}_n)^2 \right\rangle$$

In summary, the model of focus here predicts lattice thermal conductivity trends with defect concentration by capturing the perturbative effects of point defects in the scattering parameter Γ .

3.3.1. Origin of Discrepancy: Atomic Site versus Unit Cell Basis

In a phonon-based approach to thermal conductivity, one would ideally utilize the real Brillouin zone of the crystalline material. However, in efforts to create generalizable, analytic models, the Klemens model makes approximations to avoid inputs that depend highly on wave vector or atom position within the unit cell. Specifically, the monatomic lattice approximation and Debye approximation are invoked. Although these approximations are ostensibly limiting, this section demonstrates cancellations of error, which allow for a reasonable thermal conductivity prediction for many materials of interest.

Within in the monatomic lattice approximation (MLA), all the atoms of the primitive unit cell are combined into a single vibrating mass. In this scenario, the relevant Brillouin zone is confined by the volume of the primitive unit cell. As such, the original work of Klemens and other numerous works define the real space volume V_0 in Equation 3.8 as the volume of the primitive unit cell. Conceptually, this approximation is equivalent to ignoring the optical modes in the dispersion relation (as depicted in the schematic in Figure 3.3). To extend this idea fully, we treat the base unit of a primitive unit cell as a microstate of the system. Therefore, the scattering strength of the system is the ensemble average of the microstates which compose it. The unit cell model mass scattering parameter (Γ_M^{uc}) can be calculated from the fraction (P_c) of unit cells with a mass of M_c and their deviation from the average unit cell mass (\overline{M}). Finally, the mass differences are summed over all possible microstates in the lattice:

$$(3.15) \quad \Gamma_M^{\text{uc}} = \sum_c P_c \left(\frac{M_c - \overline{M}}{\overline{M}} \right)^2 .$$

While most model inputs are well-defined, it is not immediately clear what the fraction of unit cells (P_c) should be. When there is a random distribution of defects in the lattice, the fraction or probability of finding a unit cell of mass M_c can be determined from a binomial distribution function. In other instances, where defect complexes are likely, certain microstates could be weighted accordingly. A schematic of possible unit cells (microstates) for a 2-atom unit cell are shown in Figure 3.4.

However, for the case in which the defects are randomly dispersed and the binomial distribution treatment is suitable, the treatment in Equation 3.15 directly collapses into the virtual crystal approximation (VCA). Under the VCA, each atom in the material has the average mass and average volume of all the atoms in the system. Here, the relevant Brillouin zone is specified by the volume per atom, resulting in a larger Brillouin zone and larger acoustic branch that includes the phonon states previously included in the optical branch (Figure 3.3). Here, the V_0 in Equation 3.9 should then correspond to the volume per atom.

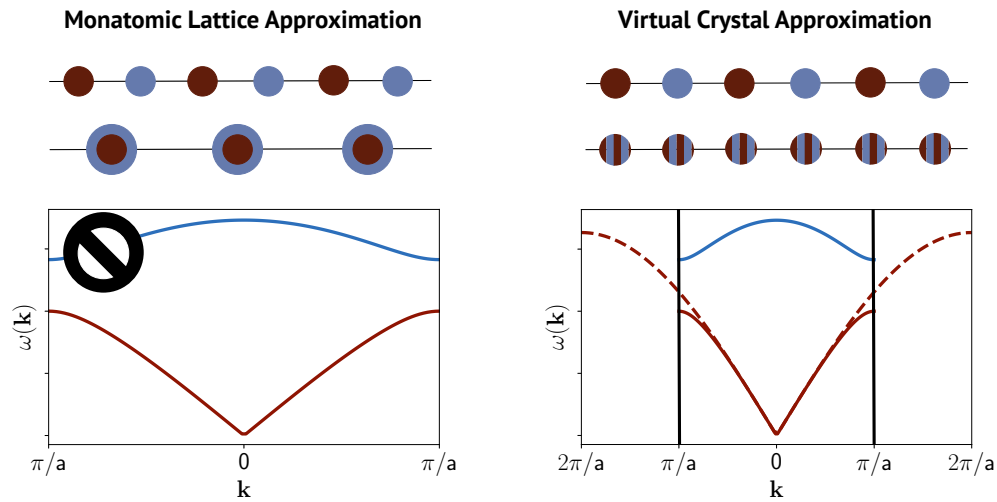


Figure 3.3. **Phonon Dispersion Diagrams Implied by the Virtual Crystal and Monatomic Lattice Approximations** The MLA and VCA represented in a 1D diatomic chain. In the MLA, the primitive unit cell is unaltered, but the atoms contained within are summed into a single, vibrating mass. As a result, there is no optical branch. In the VCA, the primitive unit cell is reduced to one atom, causing a tupling of the Brillouin zone. The large acoustic branch in this case includes the phonon states previously in the optical branch.

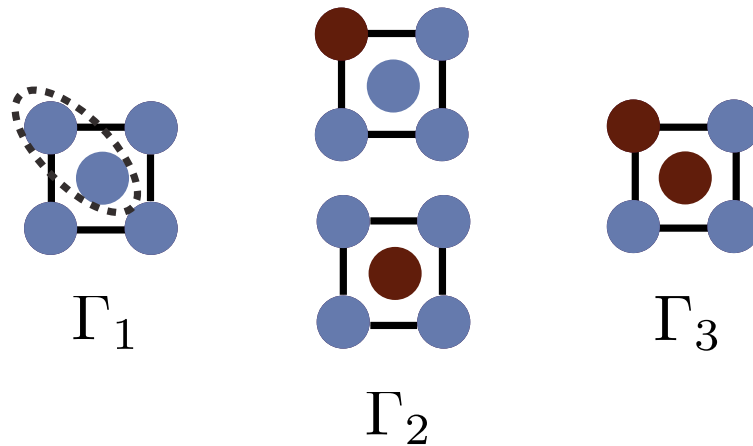


Figure 3.4. **Unit Cell Basis: Schematic of Microstates with Differing Scattering Strengths** In an example 2-atom primitive unit cell (shown in dotted line), three possible microstates exist, containing 0,1, or 2 impurity atoms. In the unit cell basis, each microstate would contribute a term to the overall scattering parameter (Γ).

The averaging scheme for the scattering strength implied by the VCA results in Equation 3.9. Due to the conflicting model representations in the literature, numerous sources use the VCA-based

expression (Equation 3.9), but define V_0 as the volume of the unit cell, as implied by the MLA. As a result, the disorder scaling parameter (u) is over-approximated by the number of atoms in the primitive unit cell. In thermoelectrics, where complex unit cells with 10-20 atoms are often favored, the resulting over-estimation is significant. The next section on vacancies and interstitials (Section 3.3.3) discusses a large majority of these over-estimated cases and a cancellation of errors which has routinely occurred.

The second approximation made is that of the Debye model, which drastically simplifies the phonon dispersion into a linear ω vs. q relation. However, the examples depicted of Si isotope scattering and $\text{Mg}_2\text{Si}_{1-x}\text{Sn}_x$ shown in Figure 3.2 both show excellent correspondence between the first principles methods and the Klemens model. Since both materials exhibit complex dispersions, which disagree with the Debye model dispersion implicitly assumed in Klemens theory, the suitability is surprising [33, 79].

Previous studies have explicitly compared the κ_L predictions of the Klemens model using various approximations of the phonon dispersion relation [69, 80]. For example, in a study of two Half-Heusler systems, three different approximations were used to describe the phonon structure of the two materials—the Debye model, a truncated Debye model, and a cubic polynomial fit of the full dispersion relation. The predicted κ_L versus defect concentration curve was plotted for each case and compared to experimental results. The study showed that the prediction of the pure thermal conductivity (κ_0) depended on the choice of dispersion. However, the ratio κ_L/κ_0 was shown to be independent of the dispersion relation choice, suggesting that while full features of the dispersion relation are required to model the thermal conductivity of pure solids, the suppression of κ_L due to point defects can be described more generally [69].

The dispersion relation dependence enters into the Klemens model through the factors of density of states and the frequency-dependent phonon velocities. In Equation 3.16 for lattice thermal conductivity, the relaxation times are re-written to isolate the density of states contribution ($\tau_{\text{PD}}^{-1} = a g(\omega)\omega^4$, $\tau_{\text{U}}^{-1} = b g(\omega)\omega^2$) with coefficients a and b combining any physical and material constants. The factor of $g(\omega)$ cancels in each of the relaxation times as well as the heat capacity,

softening the dispersion dependence of the expression.

$$(3.16) \quad \kappa_L = k_B \int_0^{\omega_m} v_g^2(\omega) g(\omega) \omega^2 \frac{(1/b g(\omega)) \omega^2}{1 + a g(\omega) \omega^2 / b g(\omega)} d\omega = \frac{k_B}{b} \int_0^{\omega_m} v_g^2(\omega) \frac{1}{1 + a \omega^2 / b} d\omega.$$

At this point, the factor of v_g^2 remains as a dispersion relation quantity in the model. Therefore, the dispersion dependence is not eliminated from the model, but softened given the cancellation in factors of density of states. Therefore, in the scenarios where phonon-phonon interactions are not largely impacted by symmetry constraints or large phonon band gaps, the ratio of point-defective to pure thermal conductivity can be well-described within Klemens theory.

3.3.2. Comparison to the Tamura Model

The mass difference model proposed by Tamura preserves the dependence of the phonon relaxation times on polarization vector and the spatial anisotropy of atomic sites within the primitive unit cell, and is frequently implemented in numerical Boltzmann transport equation solvers for thermal conductivity [47, 65, 67, 70–72, 77, 81–83]. The mass difference parameter in the Tamura model (Γ_M^T) involves performing a sum over all the atom sites s in a simulation cell, where i again labels the species that may occupy site s , including the host and substitutional atoms. In a similar fashion to previous expressions, $M_{i,s}$ and \overline{M}_s indicate the i^{th} species mass and the average mass on atomic site s , respectively. In this case, however, the mass difference term is weighted by the eigenvector components corresponding to atom s in the incident ($\mathbf{e}_{\mathbf{q}}(s)$) and final ($\mathbf{e}_{\mathbf{q}'}(s)$) vibrational mode.

$$(3.17) \quad \Gamma_M^T = \sum_s \sum_i f_{i,s} \left(\frac{M_{i,s} - \overline{M}_s}{\overline{M}_s} \right)^2 |\mathbf{e}_{\mathbf{q}}(s) \cdot \mathbf{e}_{\mathbf{q}'}(s)|^2$$

The eigenvectors are composed of the displacement vectors ($\mathbf{u}(\mathbf{q}, s)$) of each atomic site as it participates in a vibrational mode, weighted by the square root of the atomic mass ($\mathbf{e}_{\mathbf{q}} = [\sqrt{\overline{M}_1} \mathbf{u}(\mathbf{q}, 1) \dots \sqrt{\overline{M}_s} \mathbf{u}(\mathbf{q}, s)]$), and are finally normalized such that $|\mathbf{e}_{\mathbf{q}}|^2 = 1$. These eigenvectors can be calculated from the DFT (Density Functional Theory) force constant matrix [52]. The description of mass difference scattering here is general enough in its formalism that it could be

used to describe the perturbation induced to a vibrational mode regardless of its spatial extent. Therefore, in addition to plane wave phonons, the vibrational modes of diffusons, locons, and propagons within the Allen and Feldman formalism could be treated under the same point defect scattering theory [49, 84] (see Section 3.5).

Point defect scattering has been studied with first principles techniques by applying DFT to compute the full vibrational spectrum, using T-matrix scattering theory and the Tamura model to compute point defect scattering rates, and finally solving the linearized Boltzmann transport equation to get κ_L [64–67, 84, 85]. In several reported materials systems, an excellent correspondence is shown between the results attained from first principles methods described above and the analytical Klemens model (Figure 3.2) [65, 86]. It is important to remember that the Klemens model is fit to the end member thermal conductivity values, but still adequately predicts the suppression in thermal conductivity with compositional variation.

The Tamura model mass variance term converges to the analytic expression at the low frequency limit. The assumption made here is that the displacement (\mathbf{u}) of each atom in a low-frequency mode is roughly equal in magnitude; therefore, the magnitude of an eigenvector element is proportional to the square root of the atomic mass ($|\mathbf{e}(\mathbf{q}, s)| \propto \sqrt{M_s}$). This suggests that the squared polarization vector dot product ($|\mathbf{e}_{\mathbf{q}}(s) \cdot \mathbf{e}_{\mathbf{q}'}(s)|^2$) weights the mass difference on a site depending on its mass relative to the other atoms in the formula unit, or an approximate factor of $(\overline{M_s^2}/\overline{M}^2)$. This treatment results in Equation 3 and 4 suggested in the Introduction, as depicted below.

$$(3.18) \quad \Gamma_M^{\text{lf}} = \frac{1}{\overline{M}^2} \frac{\sum_n c_n \overline{M_n}^2 \sum_i f_i (1 - M_{i,n}/\overline{M_n})^2}{\sum_n c_n} = \frac{\langle \Delta M^2 \rangle}{\overline{M}^2}$$

3.3.3. Off-stoichiometric Point Defects

The Klemens/Callaway model is best defined for randomly dispersed substitutional defects. However, initial work on other off-stoichiometric defects, including vacancies and interstitials, have shown large phonon scattering effects and warrant further investigation.

Several investigations of thermoelectric compounds show large thermal conductivity reductions due to vacancy scattering [30, 87–93]. In several of these cases, the reduction in κ_L is attributed to mass difference scattering alone. However, we identified that the volume in Equation 3.6 was incorrectly defined as the volume of the unit cell rather than the volume per atom, leading to an over-prediction of the thermal conductivity change [59, 88–90, 93].

However, the large perturbation effects of vacancies are still well-described using Klemens theory [94, 95]. In this case, the lattice energy perturbation comes from missing kinetic energy (T') related to the mass of the removed atom and missing potential energy related to the removed bond between two atoms, or double the potential energy per atom ($2U'$). Within the harmonic approximation ($E = T + U_{2nd}$), the kinetic and potential energy perturbations of a single atom should be equal ($T' = U'$) according to the virial theorem, allowing one to relate the potential energy perturbation to the average atomic mass in the lattice ($\langle \overline{M} \rangle$). In the calculation of Γ , the perturbation at a vacancy site can be represented by the mass difference $M_{i,n} - \overline{M}_n = -M_{vac} - 2\langle \overline{M} \rangle$ in Equation 3.11 and Equation 3.17, where M_{vac} is the mass of the vacant atom [94, 95].

This simple treatment of vacancy scattering performs well in many defective solids, some of which are reproduced in Figure 3.5a. The experimental data shown would not be described by standard mass difference alone and requires the perturbation induced by a missing bond. The Appendix Section C compares results for the mass difference only curve versus the full inclusion of the broken bonds term, and depicts how an incorrect definition of volume can lead to a cancellation of errors.

The suitability of the vacancy model suggests, then, that interstitial atoms may be describable with an identical treatment. Interstitial or filler atoms represent the reverse situation, where an extra mass (M_{int}) is added onto a site and a new bond forms between the interstitial atom and a neighbor; therefore, a perturbation of $T' + 2U'$ should apply, yielding essentially the same mass difference as before ($M_{i,n} - \overline{M}_n = M_{int} + 2\langle \overline{M} \rangle$). It should be noted that the interstitial atom sites have a stoichiometry corresponding to the ratio of interstitial to lattice sites. While

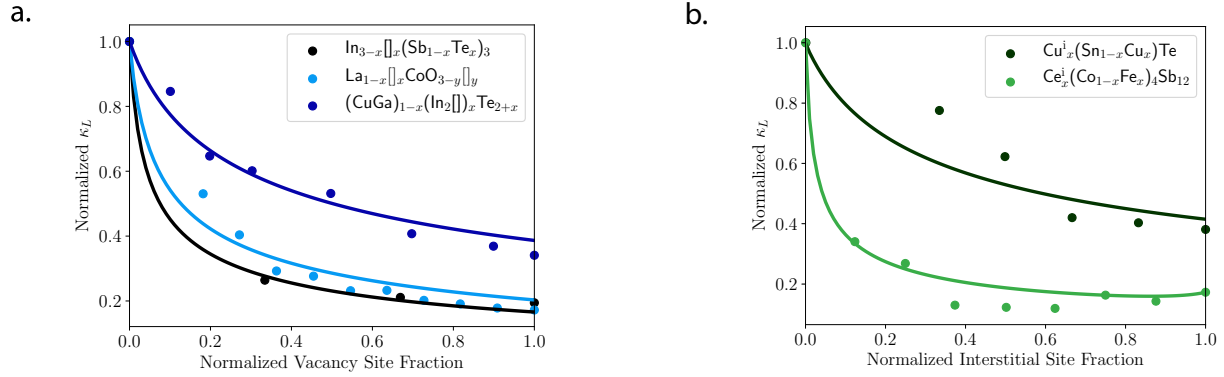


Figure 3.5. **Off-stoichiometric Defect Scattering Model Applied to Literature Data** Both vacancy and interstitial scattering data from literature (points) can be described using a simple treatment of broken (or added) bonds based on the virial theorem (line). Normalized thermal conductivity reductions for systems with (a) stoichiometric vacancies, where $[\square]$ represents a vacancy [88,89,91] and (b) stoichiometric interstitial atoms [59,96]

interstitial scattering requires more detailed study across additional materials systems, the initial data represented in Figure 3.5b, supports the application of the virial theorem treatment.

3.4. Lattice thermal conductivity versus n Trends in zT Predictions

In Section 1.2.1, we discuss the relationship between the thermoelectric figure-of-merit zT and the carrier concentration. Curves such as the one shown in Figure 1.1a are used to identify the optimal dopant concentration for a thermoelectric material. While dopants are assumed to primarily contribute charge carriers without greatly perturbing other transport properties, in several cases, this assumption breaks down. For example, several high-performance materials in the Heusler structure type are doped at high dopant concentrations [97–100], and the primary motive in doing so may be to reduce the thermal transport rather than seek improvements in electronic properties.

Here, we discuss this point using the full-Heusler VFe_2Al as an example [21]. This relatively stiff material has a large pristine lattice thermal conductivity of about 28 W/m/K. However, the mass and strain scattering introduced by dopants can cause 80% reductions in thermal conductivity as shown in Figure 3.6 below. Factors like doping efficiency, or the charge carriers contributed per dopant atom, tend to dictate dopant choice. However, the variability in point defect scattering

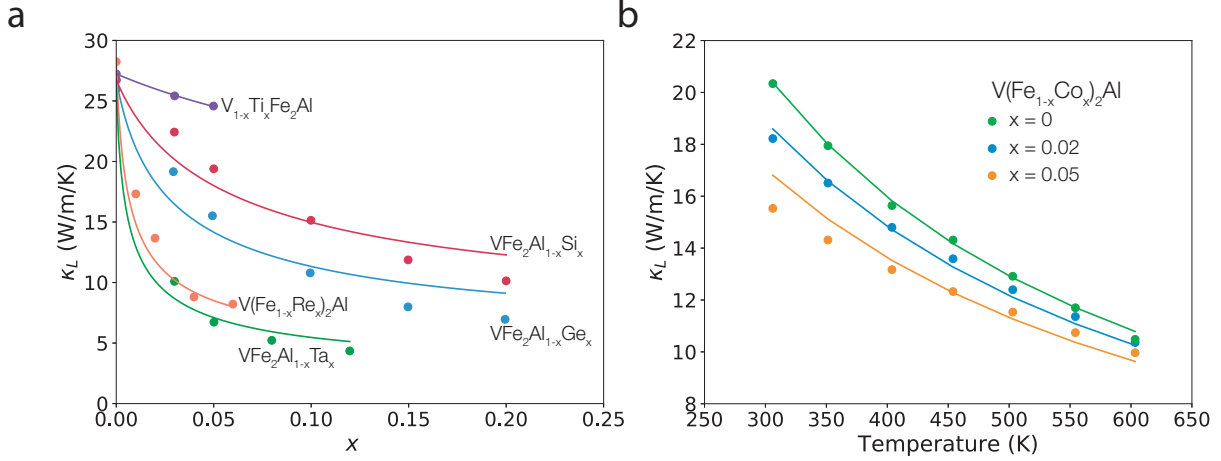


Figure 3.6. **VFe₂Al: Lattice Thermal Conductivity Trends with Composition and Temperature** κ_L trends with changes in composition are well described by analytic alloy scattering models. (a) κ_L versus composition curves from the literature [101–103] are modelled using the Klemens alloy scattering model. (b) κ_L versus temperature curves with varying Co dopant concentrations from Lu et al. [104] are modelled using point-defect and umklapp scattering theory fit with a single Grüneisen parameter of 2.78.

strength for various dopants can also be significant for a given compound, as depicted in Figure 3.6a.

Next, we plot the zT versus carrier concentration for full-Heusler VFe₂Al. This compound is a very narrow bandgap semiconductor ($E_g \approx 0.01$ eV) and is both n- and p-type dopable. We use a 2-band effective mass model to model the conduction and valence bands, with weighted mobility and Seebeck effective mass values fit to experimental S - σ and S - n relations, respectively. The two zT curves plotted in Figure 3.7 differ only in terms of their handling of the lattice thermal conductivity κ_L . The orange curve treats κ_L as a constant value equal to the pristine compound’s lattice thermal conductivity. In contrast, the blue curve incorporates the alloy scattering of phonons through the use of the Klemens model curves. The point defect scattering strength of a Ge dopant is chosen for the n-type side, and an Re dopant is chosen for the p-type side because these are the dopants with the highest reported zT values. Experimental zT values (scatter points) show a good correspondence to the 2-band model, which includes the impact of alloy scattering on κ_L . By comparing both models, it is clear that including the n -dependence of κ_L is important for predicting the correct magnitude of zT as well as identifying the optimal carrier concentration.

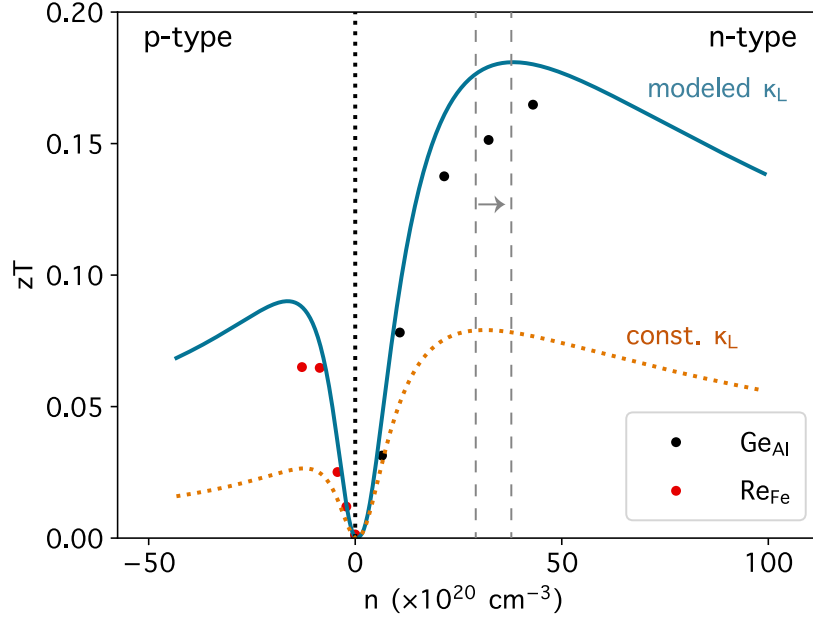


Figure 3.7. **Effect of κ_L on zT Trends with Carrier Concentration n** The zT versus carrier concentration (n) curves at 300 K from a two-band model for the valence and conduction band using a bandgap value of $E_g = 0.02$ eV. The blue curve includes the n -dependence of κ_L is included using the point defect scattering strength of Ge for n-type and Re for p-type. In contrast, the orange curve uses the constant pristine κ_L value of 28 W/m/K. Finally, we compare to experimental zT scatter points for both the Ge-doped [101] and Re-doped [103], which show good correspondence with the two-band model combined with the Klemens alloy scattering model for κ_L . Here, we emphasize that including the n -dependence of κ_L is important both for modelling the correct magnitude of zT , but also the correct n values at which it is optimized. The shift in optimal n value is signified by the dotted gray lines.

3.5. Beyond the Phonon Limit: Diffusons and Scattering Theory

Finally, we would like to acknowledge and comment on recent discussions on the suitability of the Klemens model and similar VCA-approaches to the topic of phonon scattering in alloys. The heart of the issue is that in constructing the virtual crystal, the plane-wave character of the phonon modes considered remains in tact. The mass and force constant disorder is then treated as a perturbation to these virtual crystal phonons. However, molecular dynamics (MD) simulations, which do not require assumptions about the lattice dynamics and form of the vibrational modes, have since showed that plane wave character (measured by an eigenvector periodicity parameter) rapidly decreases as compositional disorder is introduced into a solid [84]. In fact, Allen *et al.* [49]

famously ascribed a new nomenclature for vibrations in a disordered solid: propagons, diffusons, and locons. Propagons are extended modes that are phonon-like, meaning here that they have a well-described wave vector. Like phonons, propagons transfer heat ballistically between scattering events over a distance equal, on average, to the mean-free-path. Diffusons, are more localized and lack a well-defined wave vector but are still able to transfer heat through the lattice, diffusively. Finally, locons are highly localized and do not contribute to heat transport as they remain essentially tethered to a specific lattice site. Given this observed breakdown in phonon character, the suitability of the virtual crystal and perturbation theory approach may be surprising.

However, as noted in this thesis section and in Seyf *et al.* (See Figure 1 of [84]), VCA approaches such as the Klemens and Tamura models have been shown on numerous occasions to correspond well with experimental and MD results [63–66, 81]. There are a few clear examples of breakdowns in the VCA defect scattering model, which are often easiest to observe in the κ vs. T relation. Since the point-defect scattering rates derived in this chapter are temperature-independent, the T -dependence would be expected to simply follow that of phonon-phonon scattering (see Figure 2.2). In some materials, often with thermal conductivity values close to the minimum thermal conductivity limits, κ_L will be roughly constant with temperature. In these cases, which can include complex unit cell materials without compositional disorder, diffusons are likely to be the primary heat carrier, and the diffusive models described in Section 2.3.1 based on Einstein-like modes are more appropriate [33, 105].

However, the reason for the widespread suitability of the VCA models in regions of high compositional disorder and low “plane-wave” character of vibrational modes remains an open question. While we do not resolve this discrepancy in this section, the point can be elucidated further in the context of recent publications. Recent works by Simoncelli, Isaeva, and Hanus follow on from work by Allen and Feldman on harmonic disordered solids, which showed that the slightly off-diagonal terms in the heat flux operator (see Section 2.3.1), which describe the coupling between two normal modes, account for diffuson transport. Therefore, for a more unified description of the

thermal transport, the following equation for thermal conductivity is proposed, differing from the phonon gas model by instead requiring a double sum over normal modes n and m .

$$(3.19) \quad \kappa_{nm} = \sum_{nm} C_{nm} v_{nm}^i v_{nm}^j \tau_{nm}$$

Here, τ_{nm} is written in terms of the normal mode linewidths Γ_n (or spread in frequency). For the on-diagonal terms of the heat flux operator, which fit the phonon gas model, Γ_n is simply inversely related to the normal mode scattering rate $\Gamma_n = \tau_{nn}^{-1}$. The form of τ_{nm} is instead:

$$(3.20) \quad \tau_{nm} = \frac{\Gamma_n + \Gamma_m}{(\Gamma_n + \Gamma_m)^2 + (\omega_n - \omega_m)^2}$$

The Lorentzian form of τ_{nm} is such that off-diagonal terms $n \neq m$ are only significant if the normal modes are close in frequency (small $\omega_m - \omega_n$) and have sufficiently large linewidth (large $\Gamma_m + \Gamma_n$). In simpler terms, off-diagonal terms are related to the frequency overlap of normal modes once they have broadened due to anharmonic effects or disorder. In the context of this framework, the observed suitability of the VCA suggests that in many alloys and solid solutions, the disorder mainly causes a diminishing of diagonal terms of the heat current matrix without appreciable production of non-zero off-diagonal terms. Perhaps, instead, thermal conductivity lacks sensitivity to these changes in the heat current matrix because the majority of heat is carried by low-to-mid frequency acoustic branches, which are spaced out in frequency and tend to show a highly diagonal heat current matrix.

3.6. Conclusions

Analytic models of phonon–point-defect scattering have stood the test of time because of their straightforward inputs and, at times, surprising descriptiveness. Our deep dive into the expressions used in the literature and the physics they imply has led to the following insights:

- Conflicting descriptions of point defect scattering, the monatomic lattice and virtual crystal approximations have led to a common mishandling of the V_0 parameter, the essential volume of the defect. These model discrepancies have obscured the magnified scattering of off-stoichiometric defects such as vacancies and interstitials.
- We present a general formalism for calculating scattering parameter Γ , suitable for multiautomic lattices with an arbitrary number of defects occupying each sublattice.
- The widespread suitability of the analytic alloy model suggests that it is fairly dispersion relation independent. This reduced sensitivity to dispersion can be understood through a partial cancellation of the density of states in the phonon relaxation times and heat capacity.
- Phonon-dopant scattering effects should be considered when evaluating the optimum doping level for thermoelectric materials.

CHAPTER 4

Thermoelectric Transport in Multicomponent Alloys**4.1. Motivation: Unexplored Phase Space for Thermoelectric Materials**

High entropy alloy systems with multiple principal elements are considered attractive for thermoelectric materials because the mass and strain fluctuations introduced into the lattice can effectively scatter phonons and suppress the lattice thermal conductivity. Additionally, the multicomponent alloy space comprises a largely uncharted compositional territory for thermoelectric materials. Several recent reviews discuss the potential benefits of these multinary alloys to thermoelectric performance given their potential for unique, entropy-enabled characteristics [106–108]. For example, in addition to the substantial lattice distortions mentioned previously, entropy-stabilization also favors high crystal symmetry, which can lead to high electronic band degeneracy, and regions of extended solubility to facilitate doping. Some recent experimental investigations of multinary alloys have given way to highly alloyed phases which substantially out-perform end-member compounds. Androulakis *et al.* [109] demonstrated that the large lattice mismatch and strain effects in $\text{Pb}_{1-x}\text{Sn}_x\text{Te}$ -PbS alloys leads to phase separation which introduce phase boundaries with nanoscale separation that scatter phonons and induces an over 70% reduction in lattice thermal conductivity relative to PbTe. In other instances, large electronic bandstructure changes in the multinary alloy space can produce peaks in thermoelectric performance [110, 111].

However, both charge carriers and heat-carrying phonons are known to experience scattering due to alloying effects. Here, we apply analytic transport models, based on perturbation and effective medium theories, to predict how alloy scattering will affect the thermal and electronic transport across the full compositional range of pseudo-ternary and pseudo-quaternary alloy systems. For carrier mobility, the work of Makowski and Glicksman provides a straightforward expression for

alloy effects in a binary system, however, an extension to higher-order systems has not been presented. We develop a multicomponent extension to the alloy mobility model, based on straightforward materials inputs by applying computational thermodynamics techniques used to calculate excess Gibbs energy, namely the Redlich-Kister polynomial and Muggianu model. In these thermodynamic expressions, higher dimensional activity coefficients, describing the interactions between three or more alloying elements, can be expressed as a sum over binary, pairwise interaction terms. We show that within the virtual crystal approximations used in analytic alloy models, the same relationships exist, such that the excess resistivity in multinary alloys can be computed from the alloy scattering parameters fit to the binary systems.

In the case of thermal transport, a recent reformulation of the Klemens alloy model [13] (see Section 3.3) provides a straightforward route to compute the lattice thermal conductivity (κ_L) of multicomponent alloys. From our calculations, we find that the thermal conductivity is most frequently minimized along the binary system with the largest mass contrast such that adding additional alloying elements is not necessarily beneficial from the standpoint of alloy scattering. Therefore, the only way to reduce the κ_L when entering a multinary alloy space is to rely on introducing a scattering mechanism that acts orthogonally or independently of mass defect scattering such as dislocation strain or boundary scattering.

4.2. Theoretical Background

4.2.1. Electronic Transport Function

As introduced in Section 1.2.1, the electronic transport coefficient is correlated to the maximum achievable thermoelectric power factor ($S^2\sigma$) for an optimally-doped sample. The electronic transport function (σ_{E0}) can be fit directly to the Seebeck coefficient S versus conductivity σ relation (Jonker plot), using the following relationship [112]

$$(4.1) \quad \sigma_{E0} = \sigma \left[\frac{\exp \left[\frac{|S|}{k_B/e} - 2 \right]}{1 + \exp \left[-5 \left(\frac{|S|}{k_B/e} - 1 \right) \right]} + \frac{\frac{3}{\pi^2} \frac{|S|}{k_B/e}}{1 + \exp \left[5 \left(\frac{|S|}{k_B/e} - 1 \right) \right]} \right].$$

It is advisable to fit a single σ_{E0} coefficient to a series of S - σ pairs, measured at various carrier concentrations. Otherwise, computing the σ_{E0} from a the S - σ pair of an optimally doped sample (maximized $S^2\sigma$) is also suitable.

The Bardeen-Shockley equation predicts the carrier mobility by applying deformation potential theory, which considers the effect of phonon scattering on charge carriers. By treating phonons as a source of dilatational strain and calculating the shift in conduction band or valence band energies in response to this strain (neglecting higher order effects like the change in effective mass), the deformation potential Ξ is calculated in units of eV [113]. The expression for ${}^p\sigma_{E0}$ based on deformation potential theory of phonon scattering is given as:

$$(4.2) \quad {}^p\sigma_{E0} = \frac{2\hbar E_L N_v e^2}{3\pi m_I^* \Xi^2},$$

where E_L is the longitudinal elastic constant (often the bulk modulus is used), N_v is the valley degeneracy, and m_I^* is the inertial effective mass. Here we designate this coefficient with a superscript “p” to indicate that this is the value for the pure compound, prior to any alloying. Depending on whether the n-type or p-type ${}^p\sigma_{E0}$ is desired, the band properties of either the conduction or valence band are applied.

In our implementation of a σ_{E0} alloy model, we assume that the end-member compounds in the alloy systems are described by Equation 4.2. Alloy compositions will then have additional mobility effects due to alloy scattering of charge carriers. The alloying elements will be assumed to be isovalent substitutions and therefore uncharged. The scattering potential, in this case, will be determined solely from changes in the lattice potential at the defect site.

4.2.2. Alloy Scattering Potential for Charge Carriers

This work assumes that alloying produces a pure potential scattering, meaning no significant spin disorder. Here we will invoke the virtual crystal approximation once more, by comparing the disordered lattice to a reference, periodic lattice with the averaged lattice properties of the

alloy components. The coherent potential approximation (CPA) is also frequently applied to this problem, and involves self-consistently determining the self-energy of electronic states in an alloy to determine their scattering rates. In the limit of small perturbations (low defect concentration or low site energy change), the CPA also reduces down to the virtual crystal approximation [114]. It is common to evaluate the CPA correction to virtual crystal band energies, and if it is determined to be small, the virtual crystal approximation is appropriate to use for determining alloy scattering rates [115].

Unlike the previous section on phonon–point-defect scattering (see Section 3.3), in which the variance is atomic mass and radius defined the scattering strength, the lattice quantity defining the scattering strength in this case is U , the on-site potential in a tight-binding representation. The practical definition of U has been a source of discrepancy. The original work of Makowski and Glicksman [116] on III-IV zinc-blende compounds used the bandgap to define U , while subsequent work by Harrison and Hauser [117] defined U as the electron affinity, or the conduction band edge position relative to the vacuum level. However, neither definition has shown a very robust correspondence to binary alloy data, and so, in practice, the value of ΔU between two components is fit to the mobility data of binary alloy systems.

We will first show the relaxation time due to alloy scattering strength, and then discuss the expression σ_{E0} , which combines both phonon and alloy scattering of charge carriers using Matthiessen’s rule.

Analogous to the previous case of the mass defect (Section 3.2), we can write the real-space scattering potential at a defect site with a change in lattice potential ΔU :

$$(4.3) \quad V(\mathbf{r}) = V_0 \Delta U \delta(\mathbf{r}).$$

Following the procedure used previously, the alloy scattering rate includes the site fraction of point defects (n_d) and the 3D electronic density of states ($g(\epsilon)$) [118]:

$$\begin{aligned}
\tau_{\text{alloy}}^{-1} &= \frac{2\pi}{\hbar} n_{\text{d}} V_0 (\Delta U)^2 g(\epsilon) \\
(4.4) \qquad \qquad &= \frac{2\sqrt{2}}{\pi \hbar^4} V_0 (\Delta U)^2 m^{*3/2} (k_{\text{b}} T)^{1/2} \epsilon^{1/2}
\end{aligned}$$

As in the mass difference case, when this factor is generalized to multiple defects indexed by i with site fraction x_i and site potential U_i , it can be written as the average U variance compared to the virtual crystal site potential $\langle U \rangle = \sum_i x_i U_i$. Note that here we will use angular brackets $\langle \rangle$ to signify configurational averages over the component site potentials. A rearrangement of the average U variance puts it into a form particularly convenient for the charge carrier alloy scattering problem since $\Delta U_{ij} = U_i - U_j$ values between two components are nearly always fit to binary alloy data. The scattering parameter for the multicomponent alloy is written as a sum over “binary” terms, involving just two components in the alloy.

$$\begin{aligned}
\langle \Delta U^2 \rangle_c &= \langle (U - \langle U \rangle)^2 \rangle \\
&= \langle U^2 \rangle - \langle 2U \langle U \rangle \rangle + \langle U \rangle^2 \\
(4.5) \qquad \qquad &= \langle U^2 \rangle - 2\langle U \rangle^2 + \langle U \rangle^2 \\
&= \langle U^2 \rangle - \langle U \rangle^2 \\
&= \sum_{i,j \neq i} x_i x_j (\Delta U_{ij})^2
\end{aligned}$$

In Wang *et al.*, the following expression for σ_{E0} is derived by including the effects of deformation potential phonon scattering and alloy scattering, combined using Matthiessen’s rule. The resulting expression is then a modification of the reference pure ${}^{\text{P}}\sigma_{\text{E0}}$ value shown in Equation 4.2. Note that ${}^{\text{P}}\sigma_{\text{E0}}$ represents the properties of the virtual crystal, and is defined as the Vegard’s law interpolation between end-member values (similar to κ_0 in Equation 3.8).

$$(4.6) \quad \sigma_{E0} = {}^p\sigma_{E0} / \left(1 + A \sum_{i,j \neq i} x_i x_j (\Delta U_{ij})^2 \right), \text{ where } A = \frac{3\pi^2 E_L V_{\text{at}}}{\Xi^2 8k_B T}$$

In the coefficient A , quantities such as the longitudinal elastic constant E_L and average volume per atom V_{at} also vary according to Vegard's law between end-member values. Finally, to relate this problem back to the previous case on point defect scattering of phonons, let us define the electronic alloy scattering strength Γ_{el} as:

$$(4.7) \quad \Gamma_{\text{el}} = \sum_{i,j \neq i} x_i x_j (\Delta U_{ij})^2$$

In contrast to previous expressions presented by Makowski and Glicksman [116], Harrison and Hauser [117], and Mehrotra [119], Equation 4.6 is generalizable to multiple alloying elements. We additionally note that the final form of Equation 4.5 is similar to those used for excess Gibbs energy calculations in a multicomponent solution.

In the following section, we present an extrapolation scheme from binary alloy data to higher order systems based on the Muggianu model. A benefit of this extrapolation scheme is that it preserves the relationship between σ_{E0} and alloy composition shown in Equation 4.6 even if ΔU_{ij} , itself, is allowed to vary with composition. In thermodynamic terms, an activity coefficient with composition dependence represents a subregular solution model used first by Hardy to model certain binary metallic systems [120, 121]. In scattering terms, ΔU_{ij} values may vary in the terminal regions of the alloy if there are significant differences in bandstructure and host lattice properties between endmembers. So, rather than adopting a fixed ΔU_{ij} values over the entire alloy range, it maybe preferable to allow this alloy scattering potential to vary with alloy composition. The compositional variation in alloy scattering potential has only been rigorously investigated via first-principles for $\text{Si}_{1-x}\text{Ge}_x$ alloys, where changes in ΔU with respect to x , determined through DFT or tight-binding bandstructures, were fit to polynomial expressions. In this particular example,

only a light dependence on composition was observed such that the assumption of a uniform alloy scattering potential provided an adequate fit of mobility data [115,119].

4.3. Excess Thermodynamic Quantity Estimations: Redlich-Kister Polynomial and Muggianu Model

The Redlich-Kister polynomial is a simple change of variables that allows for the analytic calculation of excess Gibbs free energy (G^E) in a ternary, or higher order, alloy system. The method is especially useful in a subregular solution model, in which the interaction parameter (A_{ij}) between two components i and j is allowed to vary with composition. Here, we'll adapt the notation and convention of Hillert [120,122]. The standard regular solution model for G^E is shown below for constant binary interaction parameters:

$$(4.8) \quad G^E = \sum_{i,j \neq i} x_i x_j A_{ij}$$

As shown, higher order systems can continue to be written in as a sum of binary terms of the form $x_i x_j A_{ij}$ within the regular solution model. However, once A_{ij} is permitted to vary with composition, this relationship no longer holds true, largely because the symmetry of the problem is not maintained $1 - x_i \neq x_j$. To address this, in an example ternary composition ($x_1, x_2, x_3 = 1 - x_1 - x_2$), we can define a new set of parameters using a simple change of variables:

$$(4.9) \quad v_{12} = (1 + x_1 - x_2)/2$$

$$(4.10) \quad v_{21} = (1 + x_2 - x_1)/2.$$

In a binary system (where $x_1 + x_2 = 1$) these parameters reduce to simply x_1 and x_2 , but they retain the relationship $v_1 + v_2 = 1$ even for higher order systems. The interaction term A_{ij} can then be written as the following power series up to any arbitrary power n :

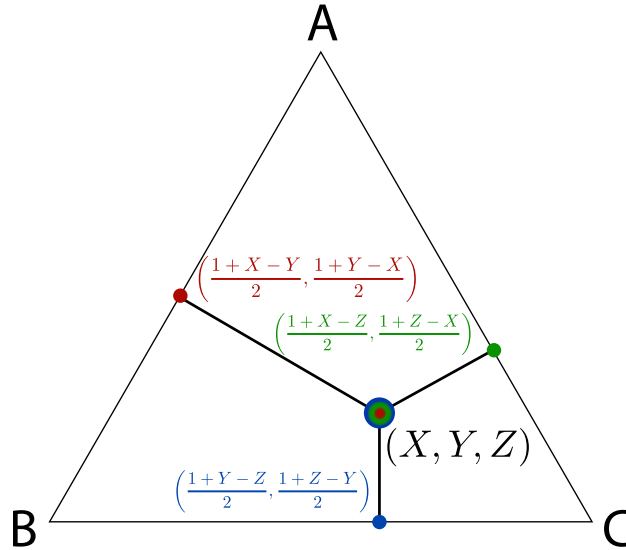


Figure 4.1. **Schematic of Muggianu Model** The geometric Muggianu model provides a method to determine a ternary excess quantity (multicolored center composition) from a weighted sum of corresponding binary excess quantities. Binary compositions are shown along binary systems as red, blue, and green scatter points.

$$(4.11) \quad A_{ij} = \sum_{k=0}^n {}^k C_{ij} v_{ij}^{n-k} v_{ji}^k$$

As before, the excess Gibbs energy can be described using Equation 4.8, using this more generalized form of A_{ij} :

$$(4.12) \quad G^E = \sum_{i,j \neq i} x_i x_j \sum_{k=0}^n {}^k C_{ij} v_{ij}^{n-k} v_{ji}^k.$$

To further simplify the model, we can apply the Muggianu method, referred to as a geometric model because it relies on the geometric construction illustrated in Figure 4.1, in which ternary excess quantities are a weighted sum of corresponding excess quantities along the binaries. Since each binary alloy system is well-defined by Equation 4.6, the Muggianu method provides the most straightforward extrapolation into the higher order space, even for composition-dependent alloy

scattering potentials. The Muggianu method defines high-dimensional (h.d.) excess alloy properties as:

$$(4.13) \quad G_{\text{h.d.}}^{\text{E}} = \sum_{i,j \neq i} \frac{x_i x_j}{v_i v_j} G^{\text{E}}(v_i, v_j)$$

In thermodynamic models for G^{E} , ternary interaction terms of the form $x_i x_j x_k A_{ijk}$, which involve three different components of the alloy, may also be used. In scattering problems, these terms would represent multiple scattering events present at clusters of defects. In our applications of the Redlich-Kister polynomial, these ternary interaction terms are neglected. Therefore, all terms in the scattering potential contain the site fractions and lattice properties of just two components in the alloy.

The Muggianu method reproduces the Redlich-Kister polynomial terms up to any power [120, 122]. Relating this expression back to the problem at hand, the working formula for the higher order extension of the electronic alloy scattering strength (Equation 4.7) is:

$$(4.14) \quad \Gamma_{\text{el}}(x_1, x_2, \dots, x_n) = \sum_i^n \sum_{j \neq i} \frac{4x_i x_j}{(1+x_i-x_j)(1+x_j-x_i)} \Gamma_{\text{el}}^{ij} \left(\frac{1+x_i-x_j}{2}, \frac{1+x_j-x_i}{2} \right).$$

Since the point defect scattering strength for phonons Γ_{ph} has the same form, we can apply the Muggianu method in the same fashion. If, perhaps, the strain scattering parameter ϵ (see Equation 3.14) describing the sensitivity of the force constants to strain varies over the alloy compositional range, the Muggianu method can be applied to perform the extrapolation to multicomponent alloys. In Section 4.4.2, we will discuss a quaternary reciprocal IV-VI semiconductor system in which the Redlich-Kister polynomials and Muggianu extrapolation are required to adequately describe the experimental data.

4.4. Results and Discussion

4.4.1. Pseudo-ternary half-Heusler Alloys

Half-Heusler compounds represent a large class of semiconducting, thermoelectric materials, which tend to be limited in their performance by relatively high κ_L values. As a result, alloying strategies to impede phonon transport are heavily sought after. We have investigated several pseudoternary half-Heusler systems with alloying on a single sublattice, including: (Ti,Zr,Hf)NiSn, (Ti,Zr,Hf)CoSb, (V,Nb,Ta)FeSb, and (V,Nb,Ta)CoSn. For simplicity, we will also label the alloying site as X . The methods described in Section 4.2 were applied to map out the transport function σ_{E0} , lattice thermal conductivity κ_L , and thermoelectric quality factor B over the full pseudoternary compositional space. These models require that the transport coefficients, elastic properties, and electronic bandstructure properties are well-defined for the end-member compounds, and literature values are used (see Appendix Section D).

Inspection of the κ_L maps for the four half-Heusler compound families shows that the lattice thermal conductivity is not, in fact, minimized at the center of the ternary, where maximal atomic disorder would be expected. Instead, κ_L is minimized along the pseudobinary with the greatest mass difference between components located along the right edge of each pseudoternary diagram shown. In fact, additional alloying with the intermediate mass component tends to reduce the overall point defect scattering.

These κ_L mappings suggest that multicomponent alloying does not by necessity lead to suppressed thermal conductivity, a result corroborated by recent first-principles thermal conductivity calculations. The X NiSn κ_L heatmap has been presented twice before from the standpoint of *ab initio* density functional theory (DFT) [123, 124]. Notably, these DFT studies continue to make the virtual crystal approximation when evaluating the alloy phonon bandstructures, using the compositional average of the atomic masses, harmonic, and anharmonic force constants. However, in contrast to the analytic expression here, the DFT-derived density-of-states, group velocities, anharmonic coefficients, and polarization vectors enter into the κ_L calculation. We observe good correspondence between our model prediction and the DFT studies. Contour lines from the work of Eliassen *et*

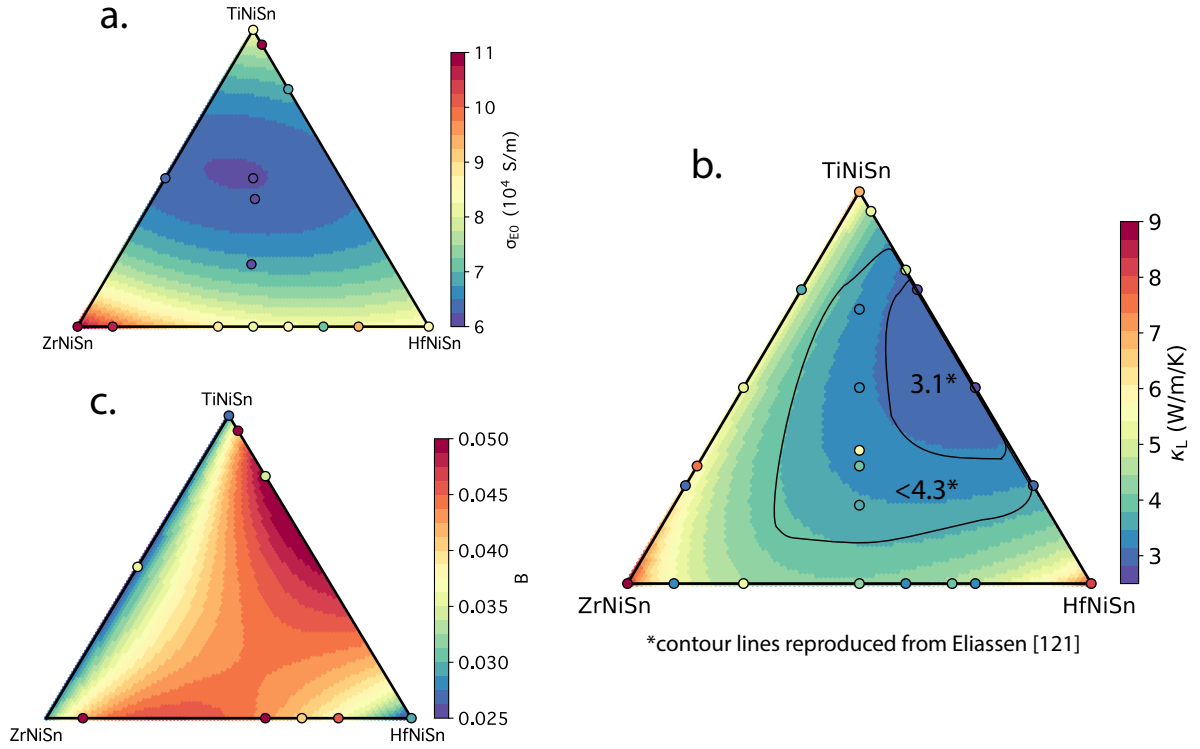


Figure 4.2. **Thermoelectric Transport Properties for (Ti, Zr, Hf)NiSn System** Alloy model predictions for the (a) electronic transport function σ_{E0} , (b) lattice thermal conductivity κ_L , and (c) quality factor B for the (Ti,Zr,Hf)NiSn system. Experimental scatter points are overlaid, and in cases where a composition was measured multiple times, the median value is plotted here. Contour lines from the DFT investigation by Eliassen *et al.* [123] are reproduced in panel (b) for comparison purposes. See Appendix Section D for full data.

al. [123] are reproduced in Figure 4.2c to highlight the minimized κ_L region. Both their work and our predictions (heatmap) show a wide basin of minimum thermal conductivity values centered around the binary alloy $\text{Ti}_{0.5}\text{Hf}_{0.5}\text{NiSn}$, with κ_L values < 4 W/m/K for a Ti content ranging from about 20 to 80% [123]. Additionally, deviating from the (Ti,Hf)NiSn pseudobinary through the addition of Zr only results in an increase of κ_L values. The same κ_L motif is shown in the computational work of Caro *et al.* [125], who used non-equilibrium molecular dynamics and the Green-Kubo method to evaluate the thermal conductivity of Lennard-Jones alloys between fictitious elements A , B , C and D , which are assigned distinct atomic mass, radius, and cohesive energy [125].

A benefit of this model is that it does not require any assumptions about the phonon bandstructure or the scattering mechanisms. The thermal conductivity mapping of the quaternary alloy still, however, shows the lowest κ_L along the binary with highest mass and radius contrast. Thus, there is strong evidence that increased compositional disorder does not, by necessity, yield a κ_L reduction.

In each of the half-Heusler alloy systems investigated, mass difference scattering alone appeared to adequately fit the experimental data, and the fitted value for the strain parameter ϵ was essentially equal to 0. This low strain scattering effect is compatible with conventional understanding of formation rules for multicomponent alloys. Large atomic size differences lead to insufficiently negative enthalpy of formation values and poor miscibility [126].

Despite the similarity in motif for the lattice thermal conductivity heatmaps, the quality factor plots for the four pseudoternary families (Figures 4.2 and 4.3) show different regions of high performance materials, arising from the trade-off between thermal and electronic transport coefficients. The magnitude of the quality factor predictions are similar between the four families, except for the $X\text{FeSb}$ system, with B values about a factor of $3\times$ higher than the other systems stemming from both high σ_{E0} and low thermal conductivity, particularly along the $(\text{Nb,Ta})\text{FeSb}$ pseudobinary (Figure 4.3(a-c)).

4.4.2. Quaternary Chalcogenide System: $\text{Pb}(\text{Sn})\text{Te}(\text{Se})$

We additionally apply this alloy model to the experimental mapping of thermoelectric transport properties performed by Ortiz *et al.* [111] of the quaternary p-type $\text{PbTe-PbSe-SnTe-SnSe}$ system. Although several previous works have investigated the 6 pseudobinary systems involving all pairs of these IV-VI compounds, this study is unique in that it reports on the multicomponent alloy space, and therefore lacks the data sparsity problem of the previous section. In our analysis, we exclude values in the vicinity of SnSe , which were shown in the original work to be the $Pnma$ rather than the $Fm\bar{3}m$ phase [111].

To perform the lattice thermal conductivity analysis, we first fit the Klemens alloy scattering model (Equation 3.8) to each of the pseudobinaries. The fit strain scattering parameters ϵ vary

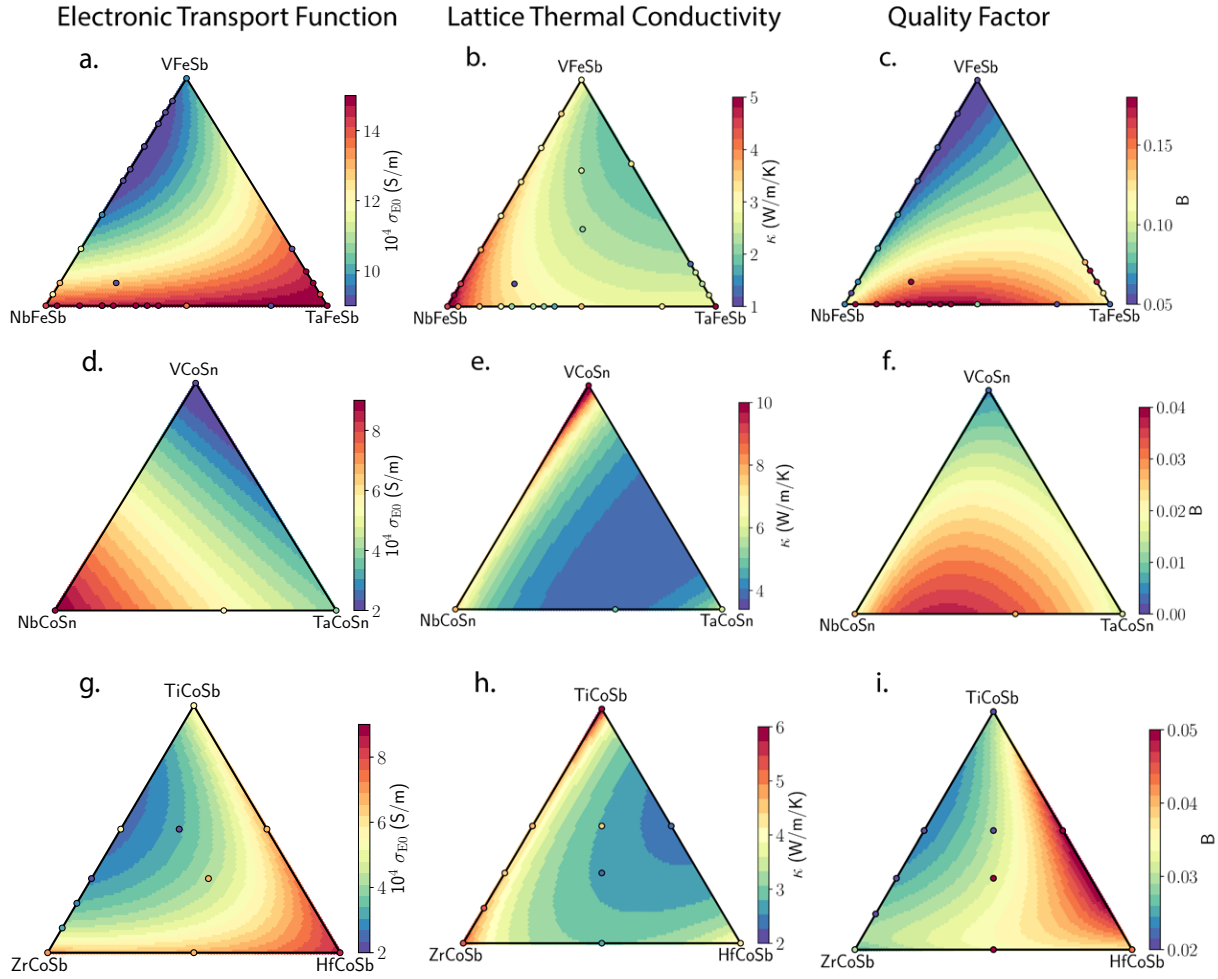


Figure 4.3. **Summary of Thermoelectric Modelling and Data for Remaining Compound Families** Alloy model predictions with overlaid experimental scatter points for three compound families: $X\text{FeSb}$, $X\text{CoSn}$, and $X\text{CoSb}$. For each system, the electronic transport function σ_{E0} , lattice thermal conductivity κ_L , and quality factor B are shown. Although each compound family has the same motif for lattice thermal conductivity, with κ_L minimized along the binary with highest mass contrast, the B factor plots show very different patterns of high and low performance regions. This speaks to the trade-off between thermal and electronic property variation with alloying.

greatly, ranging from $\epsilon = 1$ for the SnTe-SnSe system to $\epsilon = 84$ for the PbTe-SnTe system. This implies that the anharmonic and elastic properties of the lattice vary too greatly over the compositional range for a single value of ϵ to be suitable and it should instead vary with composition.

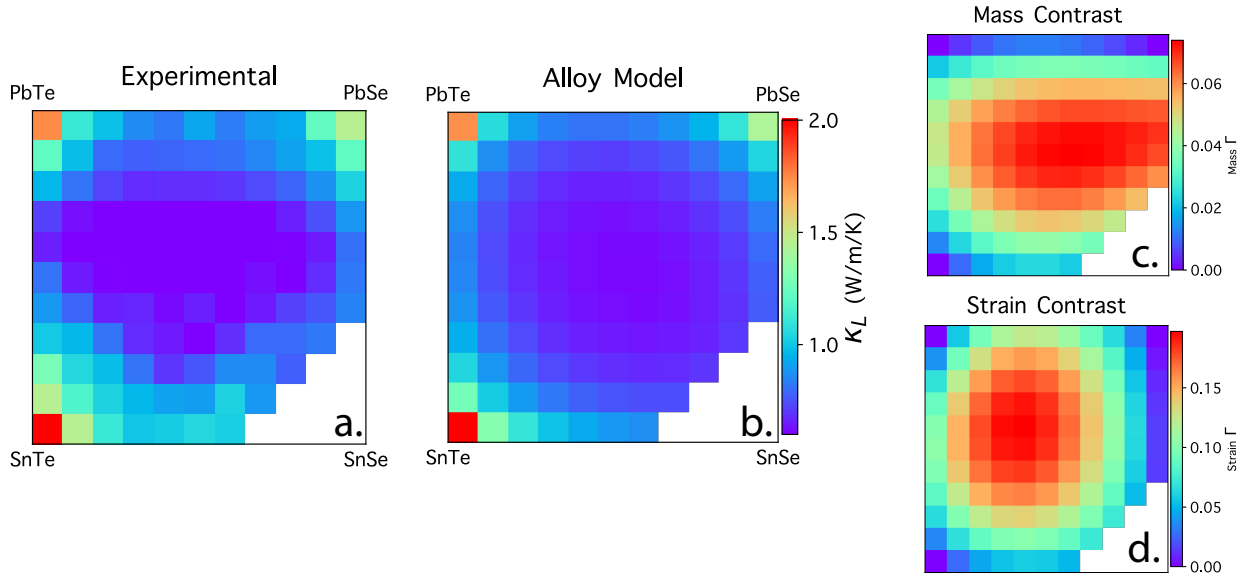


Figure 4.4. **Lattice Thermal Conductivity of IV-VI Reciprocal System** Lattice thermal conductivity heatmap in the quaternary IV-VI semiconductor system. Both the experimental measurements (a) and alloy model (b) show the thermal conductivity minimized near the equiatomic $\text{Pb}_{0.5}\text{Sn}_{0.5}\text{Te}_{0.5}\text{Se}_{0.5}$ composition. In this system, substitution on both the cation and anion site yields a peak mass and strain contrast (c,d) near the center of the compositional space.

In order to adequately fit the experimental data, it was important to use the Muggianu model to extrapolate the force constant scattering strength Γ_K from the pseudobinary to the pseudoquaternary space.

In doing so, we predict that the minimized lattice thermal conductivity κ_L occurs near the equiatomic $\text{Pb}_{0.5}\text{Sn}_{0.5}\text{Te}_{0.5}\text{Se}_{0.5}$ composition, correlating as expected with the region of maximal compositional disorder. In contrast to the previous half-Heusler examples, this reduction is achieved by alloying on different sublattices, in this case the cation and anion sites. The form of the Klemens model suggests that point defect substitutions on different sublattices should scatter independently such that an improvement from combining these orthogonal effects could be expected. In Section 4.5 we will expound upon the multi-sublattice substitution strategy and possible justifications for the improvement observed.

We additionally applied an alloy scattering model to the Hall mobility data for this p-type material. Visual inspection of the experimental data, alone, suggests that bandstructure changes independent of alloy scattering are likely at play. Rather following the expected U-shaped curve behavior predicted by Nordheim’s rule, there is a maintenance of relatively high mobility up to about 50% Sn content, after which there is an abrupt reduction in mobility that roughly corresponds in location to a documented band inversion along the PbTe-SnTe binary [111, 127]. The alloy scattering potential is, therefore, expected to change in the vicinity of different end-members. In the alloy scattering model fit to the data along the pseudobinaries, we allow the alloy scattering potential ΔU to vary with alloy composition as a Redlich-Kister polynomial up to the degree $n = 2$ in order to adequately describe the experimental data. The Muggianu method is then applied to extrapolate from the pseudobinary to pseudoquaternary space. In Figure 4.5c, we plot the deviation between the experimental and modelled mobility data. The correspondence is within $100 \text{ cm}^2/\text{V}/\text{s}$ except in the vicinity of PbSe, where the alloy model drastically underestimates the mobility. The deviation “hotspot” shown in Figure 4.5c may then be the result of large reductions in band mass that cannot be captured by an alloy scattering potential.

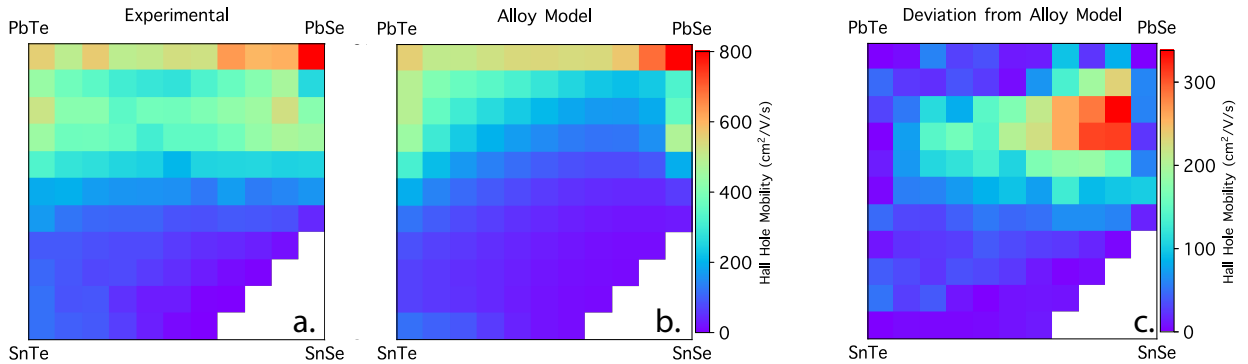


Figure 4.5. **Hall Hole Mobility of IV-VI Reciprocal System** Hall mobility heatmap in p-type quaternary PbTe-PbSe-SnTe-SnSe alloy system. The experimental data (a) is reproduced from Ortiz *et al.* [111] and is compared to the alloy mobility model extrapolated using the Muggianu method (b). Finally, we plot deviation between the experiment and mobility $|\mu_{\text{exp}} - \mu_{\text{alloy}}|$, which helps to isolate the effect of density-of-states variations (Δg) across the alloy range.

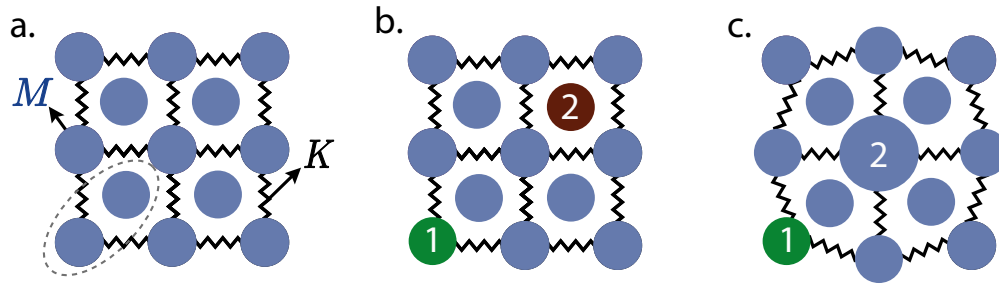


Figure 4.6. **Orthogonal Point Defect Scattering Strategies** Multicomponent alloy design strategies for reduced thermal conductivity due to point defect scattering should take advantage of orthogonal scattering effects. (a) Schematic of lattice with 2-atom primitive unit cell basis (encircled by dotted line). (b) Alloy elements, labelled 1 and 2, substitute on different sublattices. (c) Alloy element 1 contributes significant mass contrast while alloy element 2 contributes significant strain contrast.

4.5. Multicomponent Alloy Design Rules

The point defect perturbation theory approach to alloy thermal conductivity points to scenarios in which multicomponent alloying can be beneficial over a simple binary alloy. As demonstrated in several of the pseudoternary half-Heusler alloy systems, increasing configurational entropy by forming equiatomic multicomponent alloys is not always an effective strategy to reduce the thermal conductivity. In fact, introducing an alloy element of intermediate atomic mass and radius can reduce the overall mass and strain contrast scattering.

Instead, the additional alloy element should introduce an orthogonal scattering effect, i.e. a scattering effect that, to first order, acts independently of the ones already at play in the lower dimensional alloy system. Within the realm of point defect scattering, the following strategies exist:

- (1) Alloy on different sublattices of the compound (e.g. $\text{Pb}_{1-x}\text{Sn}_x\text{Te}_{1-y}\text{Se}_y$)
- (2) Use separate alloy elements to introduce mass and strain contrast into the system

The first strategy is demonstrated in the quaternary chalcogenide system discussed earlier, where the cation and anion site are both alloyed, and the minimum thermal conductivity occurs at the equiatomic $\text{Pb}_{0.5}\text{Sn}_{0.5}\text{Te}_{0.5}\text{Se}_{0.5}$ composition. This strategy suggests that the scattering along different sublattices should be uncorrelated, and confirms the importance of sublattice-specific models for phonon–point-defect scattering. The original proposed picture by Klemens of a

monatomic lattice, where the atoms in the primitive unit cell are treated as a single, large vibrating mass, is then notably misleading. The point-defect scattering expression of Tamura (Equation 3.17; reproduced below) provides insight into why individual sublattices are decoupled from standpoint of phonon scattering. Here, once again, $s = 1, 2, \dots, N$ indexes the atom sites in the primitive unit cell while i indexes the atomic species that can occupy that site, including the host atom and any impurity atoms.

$$\Gamma_{\text{M}}^{\text{T}} = \sum_s \sum_i f_{i,s} \left(\frac{M_{i,s} - \overline{M}_s}{\overline{M}_s} \right)^2 |\mathbf{e}_{\mathbf{q}}(s) \cdot \mathbf{e}_{\mathbf{q}'}(s)|^2$$

The mass contrast term is weighted by the dot product of the polarization eigenvectors of site s as it participates in the incident and final phonon mode. The monatomic lattice expression, in contrast, has no polarization vector dependence. This weighting by eigenvector overlap (related to vibrational amplitudes) causes there to be a frequency window for each sublattice in which point defect scattering is most effective. It is these unique frequency windows that can account for the decoupling (although not complete orthogonality) of the sublattices. As mentioned in Section 3.3.2, the eigenvector overlap factor approaches the squared sublattice mass (\overline{M}_s^2) at the low-frequency limit. Therefore, compounds with low mass contrast between sublattices will behave more like monatomic lattices and the orthogonality of sublattices will likely diminish. To illustrate this decoupling, the phonon bandstructure of NaCl is shown in colored by the eigenvector overlap factor $\phi_{\mathbf{q}}(s) = \frac{1}{N} \sum_{\mathbf{q}'} |\mathbf{e}_{\mathbf{q}}(s) \cdot \mathbf{e}_{\mathbf{q}'}(s)|^2$, for $s =$ the Na site. The plot for $s =$ the Cl site is exactly the opposite heatmap $\phi_{\mathbf{q}}(s = \text{Cl}) = 1 - \phi_{\mathbf{q}}(s = \text{Na})$. As shown, the frequency windows for scattering on the sublattice (indicated by a larger $\phi_{\mathbf{q}}(s)$ weighting) are separated such that the heavier element tends to dominate the lower frequency range.

The second alloying strategy of using separate alloying elements to introduce mass and strain contrast is likely more exotic, since atomic mass and size are often correlated within the same coordination environment. However, if mass and strain contrast are each maximized along different n -nary alloy systems, it is likely that entering an $n + 1$ -nary system will lead to a region of further suppressed thermal conductivity. Figure 4.8 shows a simple demonstration of this phenomenon

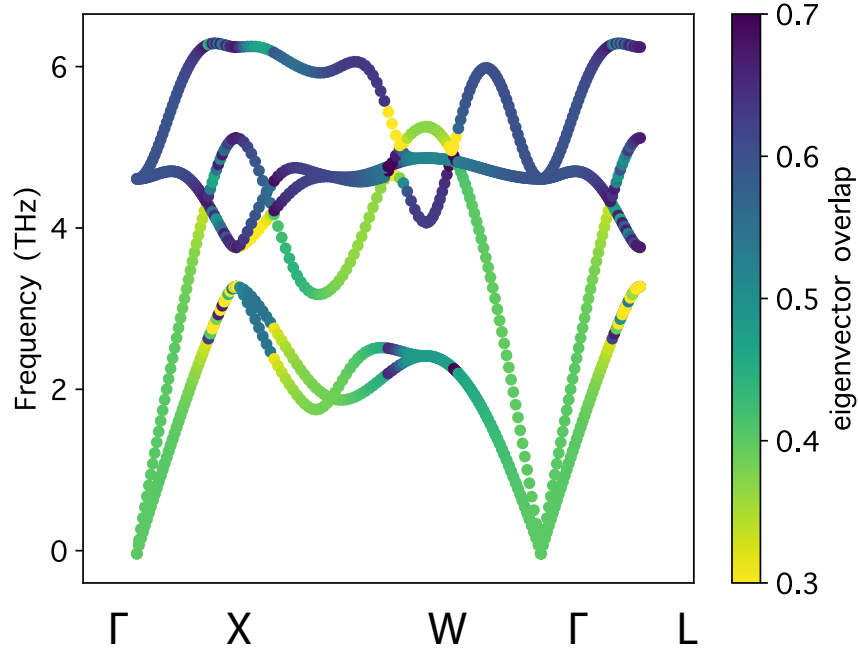


Figure 4.7. **Example Phonon Bandstructure Colored by Tamura Model Weighting Term** The phonon bandstructure of NaCl, in which phonon states are colored by the eigenvector overlap factor $\phi_{\mathbf{q}}(s)$, which weights the mass difference scattering term in the Tamura model. In this case, the bandstructure is colored by the $\phi_{\mathbf{q}}(s = \text{Na})$ term, and as the lighter element, Na follows the expected behavior by showing higher participation in the higher frequency range. The $s = \text{Cl}$ case is the exact negative of the heatmap shown, such that the scattering frequency window is in the lower frequency range.

in a toy alloy model. Here, we will consider a fictitious alloy with components A , B , and C . Each component has an equivalent pristine lattice thermal conductivity, speed of sound, and lattice parameter. The relationship between their atomic mass is: $A < B = (A + C)/2 < C$, such that the highest mass contrast exists between the $A - C$ binary. While the relationship between atomic radius is: $B < C = (A + B)/2 < A$, such that the highest strain contrast exists between the $A - B$ binary. As such, the total scattering parameter Γ is maximized near the equiatomic position, and a further reduction in thermal conductivity is achieved by entering the ternary alloy space.

However, beyond point defect scattering, additional phonon scattering effects can be modulated through alloying. Dislocation-point defect interactions have been shown to explain the high thermoelectric performance in numerous materials, as the lattice strain produced from high dislocation densities

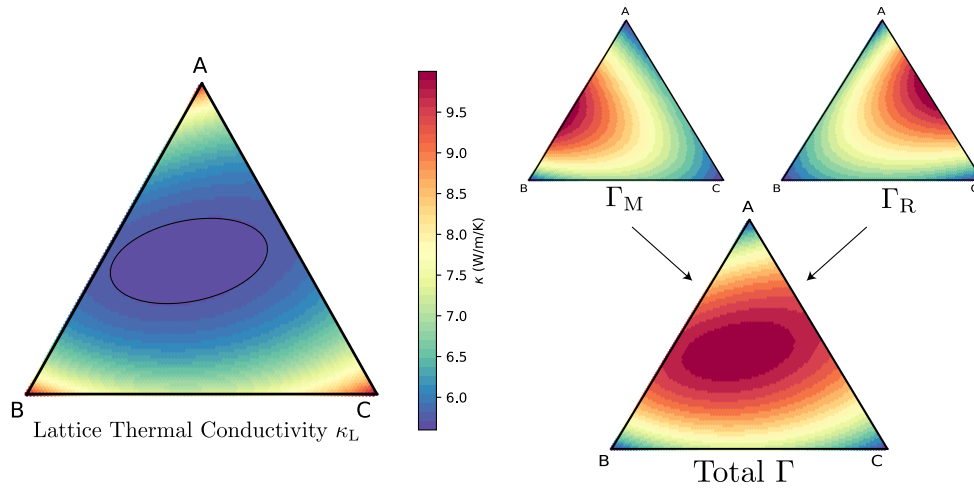


Figure 4.8. **Decoupled Mass and Strain Scattering in Multicomponent Alloy** Example ternary alloy in which the mass contrast (Γ_M) and strain contrast (Γ_R) are maximized along different binary systems. The total scattering parameter Γ is then peaked in the middle of the ternary alloy space, such that the minimum thermal conductivity region (encircled) is also centered around the equiatomic composition.

will lead to strong lattice softening and phonon scattering effects. Alloying elements can immobilize dislocations, preventing dislocation glide and annihilation, in order to maintain higher dislocation densities [128–131]. Since the perturbation to elastic constants in addition to the elastic strain around the defect is primarily responsible for this dislocation pinning, point defects with a high Γ_R parameter would be most effective for this strategy. In the case of PbTe, co-doping with Na and Eu appears to best maintain a high dislocation density even when dislocations become more mobile at elevated temperatures, performing better than samples with just a single dopant [128, 129]. This suggests, then, that multiple defects may better preserve dislocation strain.

Finally, alloying to achieve microstructural changes, through the formation of grain boundaries or even secondary phases can be an effective route to reduced thermal conductivity [132, 133]. For example, introducing MnTe into the PbTe–SrTe alloy was shown to produce low-angle grain boundaries which scattered phonons via interfacial dislocation arrays [134].

4.5.1. Physics-informed Gaussian Process Regression

The alloy scattering analytic methods will predict smooth variations of transport properties with increasing disorder. However, experimentally, we can occasionally observe discontinuous changes in properties, resulting from abrupt transitions due to electronic band convergence or phase separation. In order to retain these experimental insights, we combine the physical models described above with the statistical Gaussian Process Regression (GPR) method. A Gaussian process can be thought of as an infinite set of joint normal distributions, each describing some observable y that is indexed by a continuous variable x . Alternatively, a Gaussian process GP can be understood as a distribution of continuous functions $f(x)$, which can be sampled from to fit a set of observations [135]. A Gaussian process is specified by a mean function $\mu(x)$, defining the mean value of the GP for each value of x as well as a covariance function $k(x, x')$, describing the relationship between all possible pairs (x, x') .

In Gaussian process regression, Bayesian optimization is used to identify the function most likely to describe the observed data D as well as the variance in the prediction at each data point, through the use of Bayes Rule:

$$(4.15) \quad p(GP(\mu, k)|D) = p(D|GP(\mu^*, k^*))p(GP(\mu, k))$$

Here, $p(GP(\mu, k))$ is the prior or “initial guess” for the Gaussian process. The likelihood $p(D|GP(\mu, k))$ is the probability that the observed data D is described by the Gaussian process. As a final result, we get a final probability distribution for the Gaussian process with a mean and covariance function refined by the observed data provided (D).

It is most common to specify the prior means as simply 0 or some other constant. In this scenario, the only specified prior information is the functional form for the covariance, and the posterior probabilities only come from the refinement of the covariance matrix [136]. In this physics-informed Gaussian process regression (GPR), the transport models are used to specify the prior means of the Gaussian process. Especially in regions where no data is provided, the

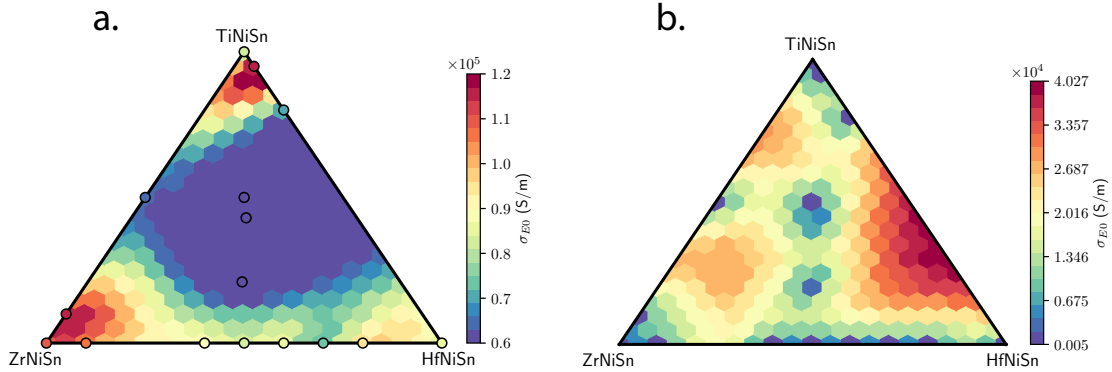


Figure 4.9. **Physics-Informed Gaussian Process Regression Transport Function Model** (a) Prediction values and (b) their associated standard deviations from the physics-informed Gaussian process regression model for σ_{E0} . The Ti-rich region with high σ_{E0} is reported to be the result of an increase in Seebeck effective mass [137]. This high-performance region is not captured by the physics-based alloy scattering models alone.

GPR refinement will rely heavily on the prior mean function. For the covariance function, we use the Matèrn kernel, as it allows for relatively discontinuous changes over shorter length scales in compositional space. Bayesian inference is then used to update the posterior distribution (which determines the prediction mean and variance) using all the available experimental data. As a result, we can acquire both predicted values and their associated uncertainties, informed both by the physics-based functional form of alloy scattering and the full corpus of experimental data available.

Figure 4.9 shows the σ_{E0} predictions and uncertainties (reported as the standard deviation) from the physics-informed GPR model. Figure 4.9a shows a region of high σ_{E0} in the vicinity of TiNiSn, which fits the measurement reported in Kim *et al.* [137] to be the result of an increase in the Seebeck effective mass. This region of large σ_{E0} is not, however, recovered in the alloy scattering model alone. The standard deviation heatmap in Figure 4.9b is straightforward to interpret—regions without experimental data exhibit higher uncertainties. Gaussian Process regression was implemented using the `gpcam` package in Python [136].

4.6. Conclusions

Multicomponent alloys formed between three or more thermoelectric compounds are an uncharted territory of high interest, primarily because of the large degrees of compositional disorder which should be effective in scattering heat-carrying phonons. Here, we show an extension of alloy scattering models for both charge carriers and phonons to higher order alloy systems. Our mapping of thermoelectric properties using analytic alloy scattering models has led to the following insights:

- Models of electronic and thermal conduction rely on the virtual crystal approximation to define a scattering parameter based off of the variance in lattice properties. In both cases, the scattering parameter can be written as a sum over “binary terms,” those which depend only on two components in the system. Their functional form mimics that of excess Gibbs free energy, allowing for an analogy to be made to computational thermodynamics literature. We are therefore able to apply the Redlich-Kister polynomial and Muggianu method to extrapolate alloy scattering models to higher dimensions.
- Additional alloying and introduction of configurational entropy does not, by necessity, reduce the thermal conductivity. To produce a thermal conductivity reduction through multicomponent alloying, the additional alloying element should introduce an orthogonal form of scattering. Within the realm of point defect scattering, this may include combining alloy elements that occupy different sublattices or using separate alloy elements to introduce mass and strain contrast into the system.
- Analytic alloy models will predict smooth changes in transport properties with respect to changes in composition. To capture more information from experimental data, we use a physics-informed Gaussian Process Regression (GPR) methodology, in which the alloy models specify the prior means in the Gaussian Process. The combined methodology preserves discontinuous changes in properties observed experimentally, which may emerge from phase separation or changes in band structure.

CHAPTER 5

Thermal Resistance of Grain Boundaries and Interfaces**5.1. Motivation: Thermal Management in Semiconductor Devices**

Self-heating is considered a major roadblock in the reliable implementation of high power nano- and microelectronic devices [5, 138]. As transistor sizes approach the few-nanometer range and the power density of integrated circuits continues to increase, thermal management issues become increasingly critical. These same semiconductor devices tend to contain a high density of grain boundaries and interfaces. Therefore, understanding how to design thermally conductive interfaces to adequately dissipate heat is of major interest. In a device-level model of GaN bonded to different substrates, a SiC substrate leads to a $\sim 1.5\times$ increase in thermal boundary conductance versus a classic Si substrate, resulting in a $> 2\times$ increase in the power density for a fixed maximum temperature of 250° across the device [4].

In contrast, thermoelectric materials benefit from suppressing heat transport, and intentionally introducing thermally resistive interfaces can be a materials design strategy. This concept is the basis of the “nanostructuring paradigm,” which suggests achieving high thermoelectric performance by designing nanoscale structural features such as nanoprecipitate phases or nanograins to scatter phonons, which additionally should not greatly disrupt charge carrier transport. In fact, major quality factor improvements have been achieved in already well-studied thermoelectric materials like bismuth antimony telluride [130, 139], lead chalcogenides [140], and CoSb_3 skutterudite [141] through the addition of low-angle interfaces composed of dislocations with nanometer-spacing.

While these two applications are opposite in terms of their material requirements, they both motivate the development of an integrated computational materials engineering (ICME) approach to thermal properties; part of which will require physical and scalable methods for modelling

interfacial thermal resistance. At the most basic level, the origin of interfacial thermal resistance stems from the atomic inhomogeneities at the interface and the mismatch in bulk, lattice properties between the materials on either side of the interface. In our work, we strive to forge an analytic link between interface type, structure, energy, and thermal resistance.

The organization of this section is as follows: Section 5.2 provides background into the definition of Kapitza or thermal boundary conductance, further details into the factors which affect its value, and an assessment of the long mean-free-path phonons we would expect to interact with interfaces. Section 5.3 reviews previous strategies used to predict Kapitza resistance based on interface properties. Section 5.4 outlines our proposed model for the thermal resistance at low-energy interfaces, which are composed of interfacial dislocations arrays and produce a form of phonon scattering that will be referred to as *diffractive scattering*. Finally, Section 5.5 reviews and attempts to quantify additional dislocation scattering effects not included in the results generated using the *diffractive scattering* model, such as dislocation core and fluttering dislocation scattering.

5.2. Phonon-Boundary Scattering Background

5.2.1. Landauer-Büttiker Formalism

It is natural to describe phonon-interface scattering through a transmission coefficient $\alpha_{ij}(\omega)$, defining the fraction of phonons of frequency ω that transmit from side i to side j of the interface. The Landauer-Büttiker formalism then relates the heat flux q_{ij} to the transmission coefficients of the incident phonons. The Landauer formalism is intended to be applied to strong, localized scatterers such as interfaces, in which the applied field is spatially concentrated at the scattering site. Here, there is a breakdown of the homogeneous Boltzmann transport equation assumptions of a uniform applied field and momentum distribution phonons throughout the specimen. The specular reflection of quantum particles at an interface was one of the earliest applications of the Landauer approach [142].

In this formulation, a given phonon mode will be described by a set of parameters: incident side (i), incident solid angle (θ, ϕ), frequency (ω), and branch (b). The heat flux can be computed

by integrating over the incident hemisphere at the interface, where the integrand is the product of: 1) the modal intensity η in terms of the phonon energy, group velocity v_g , and density of states g as: $\eta = \hbar\omega v_g(\omega, b)\cos\theta g(\omega, b)$, 2) the mode occupancy described by a Bose-Einstein factor f , and 3) the transmission coefficient α_{ij} from i to side j of the interface [143]:

$$(5.1) \quad q_{ij} = \sum_p \iiint_{\theta, \phi, \omega} \eta_i f_i \alpha_{ij} \phi \sin\theta d\theta d\phi d\omega.$$

The thermal boundary or Kapitza conductance ($h_K = 1/R_K$) is then defined at an interface using a thermal Ohm's law, relating the temperature drop at the interface (ΔT) to the heat flux across it:

$$(5.2) \quad q = -h_K \Delta T$$

To calculate the Kapitza conductance as a linear response coefficient ($h_K = \delta q / \delta(\Delta T)$), we can assume the limit of a small temperature drop at the interface as $\Delta T \rightarrow 0$. Then, h_K is equal to the temperature-derivative of the heat flux, resulting in the following dependence on heat capacity C_V :

$$(5.3) \quad \begin{aligned} h_K &= \frac{\partial q}{\partial T} = \sum_p \iiint_{\theta, \phi, \omega} \left(\hbar\omega \frac{\partial f}{\partial T} \right) v_g \cos\theta \alpha_{ij} \phi \sin\theta d\theta d\phi d\omega. \\ &= \sum_p \iiint_{\theta, \phi, \omega} C_V v_g \cos\theta \alpha_{ij} \phi \sin\theta d\theta d\phi d\omega. \end{aligned}$$

Finally, in the isotropic approximation, we can simplify this expression to an integral over spectral quantities:

$$(5.4) \quad 1/R_K = \frac{1}{4} \int_0^{\omega_m} C_i(\omega) v_{gi}(\omega) \alpha_{ij}(\omega) d\omega.$$

Of note, in this low ΔT limit, we can analyze h_K from the perspective of either side of the interface (i.e. the i and j indices can be flipped). Lastly, the current form of Equation 5.4 is subject to what's known as the Kapitza paradox, where the $\alpha_{12} = 1$ condition still yields a non-zero resistance. This can be resolved by considering the change in local equilibrium temperature of the incident and outgoing phonons [142–146]. Modifying the expression such that $\alpha(\omega)$ is replaced by $\frac{\alpha_{12}(\omega)}{1-\bar{\alpha}(\omega)}$, where $\bar{\alpha}(\omega) = (\alpha_{12}(\omega) + \alpha_{21}(\omega))/2$, addresses this issue. This modification is especially important for interfaces with high transmissivities, as the two expressions deviate considerably when $\alpha \rightarrow 1$. Therefore, our working expression for R_K is:

$$(5.5) \quad 1/R_K = \frac{1}{4} \int_0^{\omega_m} C_1(\omega) v_{g1}(\omega) \left(\frac{\alpha_{12}(\omega)}{1-\bar{\alpha}(\omega)} \right) d\omega.$$

However, in the interface perturbation approach taken in this work, we compute a phonon-interface scattering rate that modifies the overall phonon lifetime ($\tau(\omega)$) from the standpoint of the Peierls-Boltzmann Transport Equation (PBTE) for steady state transport in a system with a homogeneous temperature gradient (see red profile in Figure 5.1) [147, 148]. To relate the two descriptions (i.e. Landauer and homogeneous PBTE), let's consider a specimen with an average distance between interfaces of L_x (see Figure 5.1). The following expression relating $\alpha(\omega)$ and $\tau(\omega)$ can be derived by equating $\kappa(\omega)$ from the phonon gas model and $L_x h_K(\omega)$ [146]:

$$(5.6) \quad \alpha_{12} = \frac{v_{g1}\tau}{\frac{3}{4}L_x + v_{g1}\tau}.$$

This represents an approximate solution, ignoring the potential temperature dependence of α and the effect of the ΔT at the interface. In Section 5.4.2.2, we compare the transmission coefficients from a direct acoustic mismatch model, rooted in Landauer theory to that computed from Fermi's Golden Rule for the scattering rate, which is then converted to a transmission coefficient using Equation 5.6. We show that the two are consistent within a 5% difference up to an acoustic velocity mismatch of 50% at the interface.

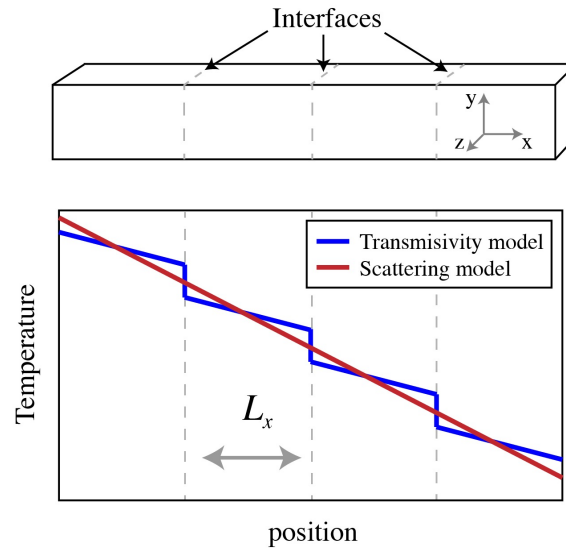


Figure 5.1. **Temperature Profiles for Landauer Transmissivity and Scattering Transport Theories** Temperature profiles in a sample with an average grain size L_x . In the scattering model, the interface perturbation modifies the overall phonon lifetime and maintains a uniform temperature gradient across the sample. Landauer theory allows for spatial variation of the applied field and supports temperature drops spatially localized at the interfaces.

5.2.2. Phonon Scattering Sources at an Interface

The discussion of phonon scattering at grain boundaries and interfaces tends to be difficult to define in a self-contained way, in part, because of the complexity of the defect structures and the numerous scattering effects that may be at play [22]. Here, we summarize the various scattering effects which may be present at internal boundaries. The scattering effects are separated into two major categories: elastic and inelastic processes. The elastic scattering processes treat the interface and its associated strain fields as a static defect which lacks the dynamical degrees of freedom to absorb or emit a phonon [56]. As such, the total momentum and energy of the incident phonon will be conserved across the interface. The inelastic scattering processes, by contrast, allow the incident phonon to absorb or emit energy at the interface by interacting with localized, interfacial vibrational modes or mobile interfacial defects.

Elastic Scattering Sources:

- Change in acoustic medium (i.e. acoustic impedance mismatch) [143, 149, 150]
- Interfacial Dislocations (strain fields or core scattering) [23, 38, 39, 56, 130, 151, 152]
- Coherency Strain [153]
- Compositional or Structural Disorder (point defects, interface roughness, alloying/amorphous layer with unique elastic properties) [154–156]

Inelastic Scattering Sources:

- Phonon coupling to interfacial vibrational modes [157, 158]
- Interactions with mobile dislocations (i.e. phonon-mediated dislocation drag) [159, 160]

5.2.3. Heat Carried By Long Mean-Free-Path Phonons

If the phonon mean free path is less than the average grain size in a material, boundary scattering would have a limited effect on thermal transport. Therefore, understanding the heat carried by long mean-free-path phonons is very relevant to the topic of boundary scattering. Cumulative thermal curves (CTCs) are typically used to quantify and understand how the distribution of phonons in a material contribute to thermal transport. While we often refer to the frequency distribution of phonons, phonons can also be codified in terms of the mean free path (Λ) when only phonon-phonon interactions are present in a bulk, pristine crystal. Phonons with a mean free path greater than or equal to the average grain size L ($\Lambda \geq L$) will be affected by boundary scattering, while the impact of grain boundaries and interfaces should be largely negligible when $L \gg \Lambda$ [22, 161]. The two regimes are portrayed in Figure 5.2 adapted from Aketo *et al.* [161]. Within the Debye model, Umklapp phonon-phonon interactions result in a $\Lambda \propto \omega^{-1}$, such that long Λ phonons are also low frequency, or long wavelength phonons. To predict whether nanostructuring will impact the thermal conductivity of a material, it is important to understand and quantify the heat carried by low-frequency phonons close to the Γ point.

Near the Γ point, we would expect the phonon dispersion to be fairly linear, described by a constant speed of sound as in the Debye model. By reviewing the frequency dependencies of the components of thermal conductivity, we see that $\kappa(\omega)$ should approach a non-zero constant value

in the limit of $\omega \rightarrow 0$: 1) $C_V \propto \omega^2$, 2) $v_s \propto \omega^0$, and 3) $\tau \propto \omega^{-2}$. In summary, near Γ point phonons carry very little heat, but have long lifetimes, such that theory predicts a non-zero spectral thermal conductivity at this frequency range. Using a Debye model and an analytic expression for the phonon-phonon interactions, the following expression for the spectral thermal conductivity can be derived, and, as expected, is a constant with respect to frequency:

$$(5.7) \quad \kappa_U(\omega) = \frac{(6\pi^2)^{2/3}}{8\pi^3} \frac{\overline{M}v_s^2}{TV^{1/3}\gamma^2}$$

However, because of the divergence of the phonon lifetime at the Γ point, most DFT-based thermal conductivity codes apply a special handling at the Γ point to enforce that the thermal conductivity equals 0 [47, 162]. This involves artificially setting the phonon velocity or even the lifetime to equal 0 at Γ , perhaps neglecting important heat contributions of phonons in this range. Additionally, most thermal conductivity codes calculate spectral quantities by performing a Brillouin zone integration over a uniform \mathbf{q} -mesh. As a result, high mesh densities are required to sample near the Γ point.

Experimental investigations instead show that a significant portion of heat is carried by very long-wavelength phonons. The harmonic and anharmonic properties of sub-terahertz phonons can be studied experimentally using inelastic X-ray and neutron scattering as well as pump-probe femtosecond laser methods. For example, measurements of sub-terahertz acoustic phonons in GaN show that 10% of heat is carried by phonons under 2 THz (about 6% of the maximum frequency) [163–165].

Here, we briefly analyze the Γ point handling in the open-sourced `phono3py` package for calculating thermal conductivity from DFT phonon bandstructures [47, 166]. The spectral thermal conductivity and its components (i.e. spectral heat capacity C_V , squared group velocity v_g^2 , and scattering rate Γ) were calculated for Si using an $11 \times 11 \times 11$ uniform \mathbf{q} -point mesh and the tetrahedron method for Brillouin zone integration. The tetrahedron method provided much more reasonable spectral curves in comparison to Gaussian smearing, with better performance around

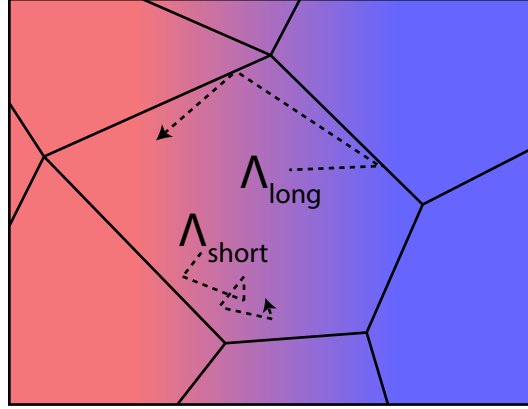


Figure 5.2. **Schematic of long and short mean-free-path phonons in a polycrystalline material** [modeled off of Figure 1 in Ref. [161]]. Short mean-free-path phonons will be scattered by mechanisms within the grain (phonon-phonon interactions, point defects) and will, therefore, not interact with grain boundaries and interfaces.

sharp features like van Hove singularities [167]. Figure 5.3 shows the computed spectral curves. Only the xx components are shown for v_g^2 and κ , which will be equal to the other principal components yy and zz in Si. Additionally, the analytic fitted trends expected near Γ are shown in red, and there is an observed correspondence between the DFT spectral curves and analytic trends for all spectral properties except for v_g^2 . The curve generated through `phono3py` is enforced to be 0 at the Γ point, while the analytic prediction would converge to a constant, equal to the squared average acoustic velocity. The Γ point $\kappa(\omega)$ calculated from these fit analytic curves is additionally shown, and indicates κ approaching a constant value of 4.95 W/m/K/THz. This value corresponds well with that calculated using Equation 5.7.

If we then modify the spectral thermal conductivity to approach a value of 4.95 W/m/K/THz, we see the expected change in the CTC curve near Γ . Phonon frequencies under 2 THz are shown to contribute additional heat, which is also reflected in an increased overall thermal conductivity, closer to the converged value achieved at higher k-point mesh densities.

We wish to emphasize the importance of developing accurate spectral thermal conductivity curves in the low-frequency range in the development of nanostructuring strategies for low thermal

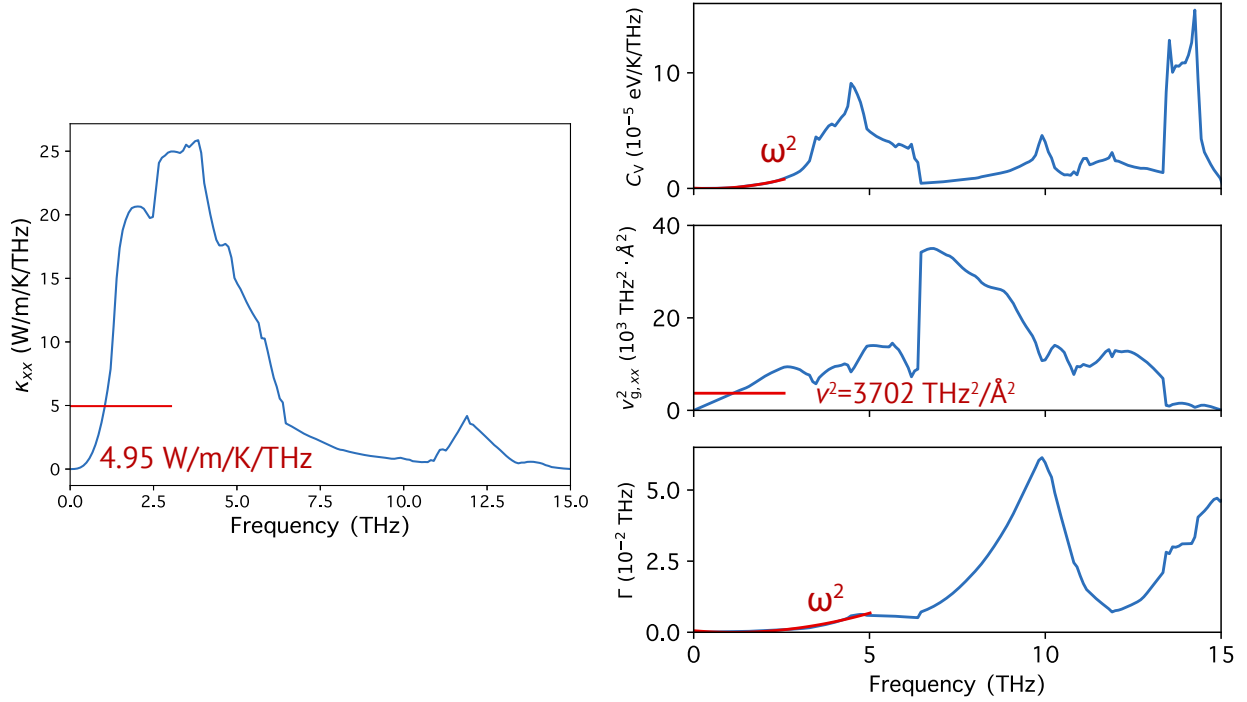


Figure 5.3. **Spectral Thermal Quantities Extrapolated to the Γ Point** Spectral thermal quantities (C_V , $v_{g,xx}^2$, $\tau^{-1} = \Gamma$) for Si are calculated using the tetrahedron method on an (11,11,11) mesh. The red curves near the Γ point reflect the frequency-dependencies based on a Debye model and umklapp phonon-phonon scattering. While the value for $v_{g,xx}^2$ is computed from DFT acoustic velocities at the Γ point, the red curves for C_V and τ^{-1} are fit. An extrapolated value for $\lim_{\omega \rightarrow 0} \kappa_{xx}$ is then computed using the phonon gas model. The value of 4.95 W/m/K is close to that estimated using Equation 5.7 of 4.16 W/m/K.

conductivity materials. Analytic corrections such as the one discussed in this section may be a route to adjust for current Γ point anomalies without adding computational cost.

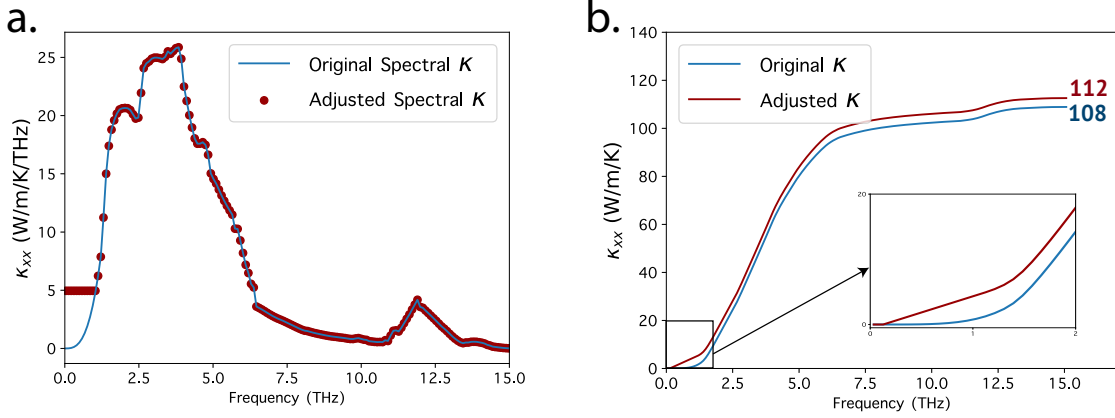


Figure 5.4. **Adjustment of Spectral Thermal Conductivity at Γ Point** (a) Rather than approaching zero at the Γ point, κ_L is modified to converge to a value of 4.95 W/m/K/THz. (b) The impact of the adjustment is shown in the cumulative thermal curve, which has a higher slope near Γ and a higher overall thermal conductivity, closer to the converged κ value attained using a higher mesh density.

5.3. Existing Approaches to Evaluating Phonon-Boundary Scattering

In this section, we will review existing theory and simulation-based approaches to calculate the phonon transmission coefficients $\alpha(\omega)$ at grain boundaries and interfaces, allowing for the prediction of Kapitza resistance (R_K).

5.3.1. Analytic Transmission Coefficients: Acoustic and Diffuse Mismatch Models

A common, but highly simplified approach to phonon-boundary scattering is the “gray” approximation, which suggests that the phonon mean free path is directly proportional to the average grain size (L). This assumption lacks any frequency-dependence and enforces that all phonons in the spectrum have the same mean free path. Some implementations may use a geometric factor as a constant of proportionality, but the essential form of the scattering rate is:

$$(5.8) \quad \tau^{-1} = v_s/L$$

Although this form is highly simplified, with no information about the interfacial structure or mismatch in properties at the interface, several multiscale thermal models currently implement the gray approximation because it is computationally cheap [168].

Two widely used formalisms to compute the transmission coefficient, which include information about the materials surrounding the interface, are the acoustic and diffuse mismatch models. They are discussed as comprising lower and upper bounds to the transmission coefficient [143, 155]. The acoustic mismatch model (AMM) implies a perfectly smooth interface, leading to a specular reflection or transmission of phonons. In contrast, the diffuse mismatch model (DMM) assumes a highly disordered interface, leading to completely diffuse scattering, in which only the energy of the phonon mode is conserved across the interface.

The acoustic mismatch model (see Figure 5.5a) is a solution to continuum elasticity equations at a smooth, abrupt junction between two different linear elastic solids. The transmission coefficient (Equation 5.3.1) is primarily defined from the mismatch in acoustic impedances across the interface, where the acoustic impedance is the acoustic velocity times the mass density (ρ), as shown [143, 169]:

$$(5.9) \quad \alpha_{12}(\omega)_{\text{AMM}} = \frac{Z_1 Z_2}{(Z_1 + Z_2)^2} \quad \text{where } Z_i = \rho_i v_i \cos \theta_i.$$

Here, the angles θ_1 and θ_2 describing the incident and outgoing phonon trajectories are related through an acoustic Snell's law, $v_2 \sin \theta_1 = v_1 \sin \theta_2$. The AMM notoriously underestimates thermal resistance, and several modifications have been proposed to improve its predictive power, including a “specularity coefficient” to account for interfacial roughness [155].

The diffuse mismatch model (see Figure 5.5b) has more widespread use, however, the origin of the scattering is not specified in this case, making it less interpretable. Instead, the scattering probability is set only by the available phase space on either side of the interface (from perturbation

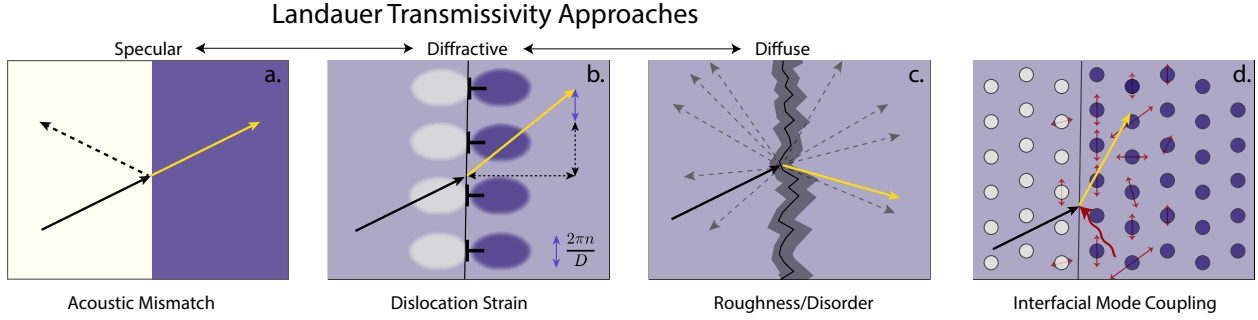


Figure 5.5. **Schematic of Interfacial Scattering Mechanisms and Implied Phonon Transitions** (a) The acoustic impedance mismatch across the interface can lead to a reflection or transmission probability in analogy to Snell’s law. (b) Many low-energy interfaces can be decomposed into periodic arrays of dislocations, which act as a diffraction grating for phonons. The dislocation array can impart quantized momentum in units of $2\pi/D$, where D is the dislocation spacing. (c) Interfaces serve as a sink for point defects, leading to additional roughness and compositional disorder. These effects are often modeled as a source of diffuse phonon scattering, in which only phonon energy is conserved at the interface. (d) Finally, if the vibrational basis set includes the interfacial vibrational modes, such as the localized mode portrayed here, coupling to interfacial modes can also enhance or diminish the interfacial thermal conductance through inelastic processes.

theory considerations [149]), captured by the 3D phonon density of states g mismatch for the incoming phonon frequency ω , as shown [149, 155]:

$$(5.10) \quad \alpha_{12}(\omega)_{\text{DMM}} = \frac{\sum_j g_{2,j}(\omega)v_{2,j}}{\sum_j g_{1,j}(\omega)v_{1,j} + \sum_j g_{2,j}(\omega)v_{2,j}}.$$

5.3.2. Atomistic Thermal Simulations

In this section we will discuss two common atomistic simulation approaches to thermal boundary conductance. Molecular dynamics, a real-space representation of heat transport, and the atomistic Green’s function, a reciprocal space approach.

5.3.2.1. Molecular Dynamics. Molecular dynamics (MD) simulations use classical mechanics to update atom positions and velocities in each time step of the simulation. Unlike the scattering frameworks described previously, individual scattering contributions do not have to be separately modelled or understood in an MD simulation, as they will be naturally captured as long as the

harmonic and anharmonic properties of the lattice are well-described by the MD interatomic potentials. Molecular dynamics (MD) simulations can be used to compute a Kapitza resistance R_K directly from the simulation temperature profile once steady state has been established. Much of the currently available data used to understand R_K trends between grain boundary type, angle, and orientation stem from MD investigations [170, 171]. Several similar strategies exist for extracting the Kapitza resistance from MD simulations [171, 172]. One common approach described by Schelling *et al.* [171], involves adding and subtracting energy $\Delta\epsilon$ from a thin slab of atoms on either side of the boundary, which fixes the thermal current. Then, the temperature discontinuity at the interface is computed from the temperature profile (ΔT) such that the R_K can be solved for using Equation 5.2.

MD simulations offer many advantages through being a real-space, time-domain technique. For example, using the Green-Kubo modal analysis method, the modal contributions to the atom positions and velocities can be determined, allowing one to then evaluate the modal contributions to the Hardy heat flux operator (\mathbf{j}) [51–53]. The Green-Kubo formalism can then be applied to evaluate the thermal conductivity from the time correlation of the heat fluxes as

$$(5.11) \quad \kappa = \frac{1}{Vk_B T} \int_0^\infty \langle \mathbf{j}(0) \cdot \mathbf{j}(t) \rangle dt.$$

This time-correlation approach can have major benefits over the phonon gas model when phonon velocities are ill-defined, which tends to occur in highly disordered materials and complex unit cell materials, common in the field of thermoelectrics [51]. However, interpreting these simulation can become a challenge since post processing or controlled wave packet simulations [55] must be performed to extract mode specific properties.

A similar modal analysis technique has been developed by Gordiz and Henry specifically for interface conductance, and is referred to as ICMA (interface conductance modal analysis) [173–175]. This technique has revealed that, in certain cases, a new set of vibrational eigenmodes, unique to the interface, must be included in the analysis to fully describe the heat flow across the

interface. In the case of a Si-Ge heterointerface, the interfacial modes were shown to contribute to heat transfer, increasing the h_B relative to the model that excluded these modes [175]. A more comprehensive survey of interfaces between different materials has since suggested that interfacial mode coupling may be a unique feature of interfaces between certain structure types, like the diamond cubic lattices of Si and Ge [158].

5.3.2.2. Atomistic Green’s Function. An increasingly popular alternative simulation approach is the atomistic Green’s function (AGF). As with lattice dynamics (Section 2.1), AGF is a reciprocal space approach and is useful for studying the spectral dependence of phonon transmission at an interface [55]. Physically, the Green’s function represents the response of the lattice dynamical equations to an impulse perturbation. The AGF can be applied to the interface scattering problem in a straightforward way by re-framing the system as two contact materials, each described by a separate Green’s function, which are then coupled at the interface. The system’s dynamical response to the perturbation caused by this coupling is captured by this approach and used to compute a spectral phonon transmission coefficient [176]. While this approach is known to perform efficiently in the ballistic regime, anharmonic scattering effects have been notoriously difficult to implement, although developing anharmonic extensions to the AGF is a rapidly progressing initiative [177,178].

5.4. Model for Low Energy Grain Boundaries and Interfaces

As mentioned in the introduction to this section, the thermal resistance of an interface is produced by both the change in atomic structure in the vicinity of the interface as well as the mismatch in bulk properties between the materials surrounding the interface. In this section, we will outline our model for phonon scattering at grain boundaries and interfaces with well-defined underlying dislocation arrays, which result in a net misorientation at the boundary. We focus on interface types which are described by the Read-Shockley model [179], an early success in the theory of grain boundaries. They developed a quantitative description for the energies of low-angle grain boundaries by suggesting that the interfacial energy per unit area came simply from the energies of the periodically spaced dislocations located at the interface. The excellent correspondence to

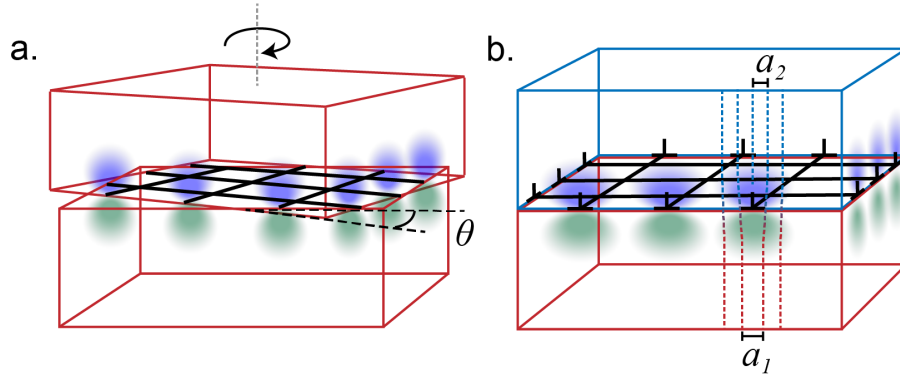


Figure 5.6. **Interfaces Described by a Grid of Linear Defects** (a) Schematic of a twist boundary with misorientation angle θ . The black lines indicate screw dislocations and the blue/green shading indicates shear strain. (b) A semicoherent heterointerface between two materials with lattice constants a_1 and a_2 . The black lines indicate edge dislocations and the blue/green shading indicates hydrostatic strain.

measured grain boundary energies solidified the dislocation model for low-angle grain boundaries and interfaces [179, 180]. The following boundary types will be considered in this section: 1) the symmetric tilt grain boundary, which is decomposed into a 1D array of edge dislocations, 2) the symmetric twist grain boundary, which is decomposed into a 2D grid of screw dislocations, and 3) the semicoherent heterointerface, which is decomposed into a 2D grid of misfit edge dislocations (extra half plane oriented perpendicular to the interface). The dislocation structure of the twist boundary and semicoherent heterointerface are diagrammed in Figure 5.6, and will be the focus of this section, as they are united by their similar dislocation grid structure. The tilt boundary case was studied in a previous work [181], but will be invoked here for comparison purposes.

Recent experimental work on grain boundaries and heterointerfaces suggests that insights into the role of interfacial dislocation structure on thermal resistance will be highly impactful. For example, the periodic dislocation structure present at low angle grain boundaries has been associated with significant thermal conductivity reductions and improvements in the thermoelectric performance of well-studied materials such as bismuth antimony telluride [130, 139]. While several experimental investigations exist for the ensemble average interface scattering in a polycrystal, individual grain boundary types are difficult to study. However, recent R_K measurements using

the 3ω method on fabricated twist bicrystals of Si [182] and Al_2O_3 [183] point to evidence of dislocation strain scattering as a dominant mechanism. For example, the thermal boundary resistance R_K of these twist boundaries is shown to depend on the grain boundary angle, or equivalently, the dislocation spacing, in addition to the interfacial strain energy. In both the Si and Al_2O_3 twist boundaries, TEM imaging has been used to verify the presence of dislocation arrays at the interface [182, 183]. Additionally, heterointerfaces are often intentionally created in thermal materials through a variety of nanostructural features including heterostructures, thin film superlattices, and nanoprecipitate boundaries [184, 185]. Thus far, it has been difficult to experimentally determine the effect of misfit dislocations—which can in some cases be controlled through annealing and interlayer thickness—on thermal resistance. Our model, which quantifies the relative importance of interfacial dislocation strain versus acoustic mismatch, can quantify the degree of disregistry at an interface required to suppress phonon transmission.

There are two major interface scattering effects described by this model: 1) the periodic strain fields from interfacial dislocations and 2) the mismatch in acoustic medium at the interface. These scattering contributions not only differ in terms of physical origin, but also in defect dimensionality, allowed scattering transitions, phonon frequency dependence, and regions of the phonon spectrum most impacted.

The first scattering effect, acoustic mismatch, is the basis of the classical AMM (discussed in Section 5.3.1), which comes from solving continuum elasticity equations at the abrupt junction between elastic media. In contrast, our treatment handles this mismatch scattering within quantum perturbation theory, and we show that the magnitude of the phonon transmission coefficient agrees well with the classical acoustic mismatch model. As in the classical case, the acoustic mismatch potential results in a specular reflection or transmission. More specifically, the momentum transfer parallel to the interface must be 0, since the acoustic mismatch potential does not include any atomic variation or disorder along the interface plane. Long-wavelength, low-frequency phonons, which remain agnostic to the underlying dislocation structure at this interface, will be scattered

by the acoustic mismatch potential. Finally, since this scattering potential holds the geometry of a planar defect, the phase space term is given by the 1D density of states (Section 2.2.2).

Phonons with wavelengths on the order of the dislocation spacing will interact with the periodic dislocation strain at the interface. The periodic variation of these strain fields parallel to the interface allows for momentum transfer in the direction of periodicity, but only in allowed increments proportional to the dislocation spacing. We term this *diffractive scattering*. Diffractive scattering stands as an intermediate step between specular and diffusive scattering (see Figure 5.5) in terms of available scattering phase space and, as a result, transmission coefficient. In addition, the geometry of this scattering effect is an array of linear defects, and as such it contributes to the frequency-dependent 2D density-of-states as the phase space term in the scattering rate.

To help understand these scattering contributions further, we show in Figure 5.7 the analytically calculated dilatational component ϵ_{yy} of the strain tensor for a simplified heterointerface in which there is lattice mismatch in one direction only and thus only one array of misfit dislocations. The dilatation behaves asymptotically like a step function, but the large nonzero value of ϵ_{yy} as $|x| \rightarrow \infty$ is spurious, since it is being defined with reference to a fictitious average lattice. The actual reference lattice differs on the two sides of the interface. The true or *physical strain*, ϵ_{eff} , must be defined with respect to the true reference lattice, and is obtained by subtracting off the dilatation step function. This strain is much more localized to the vicinity of the interface. As highlighted in Figure 5.7b, the physical strain scatters via the lattice anharmonicity, while the step function change in lattice parameter and the harmonic properties of the lattice is treated as an acoustic impedance mismatch. One benefit of our approach is the ease of separating the relative scattering contributions of the acoustic mismatch and dislocation strain in each grain boundary type.

In the following section, we first discuss the scattering kinematics for the periodic scattering potential at the interface. Then, in Section 5.4.2 we describe the origins of the scattering potential for both dislocation strain and the acoustic mismatch. Next, we apply the framework to analyze and compare the scattering properties of Si-Si symmetric tilt and twist grain boundaries (Section 5.4.3).

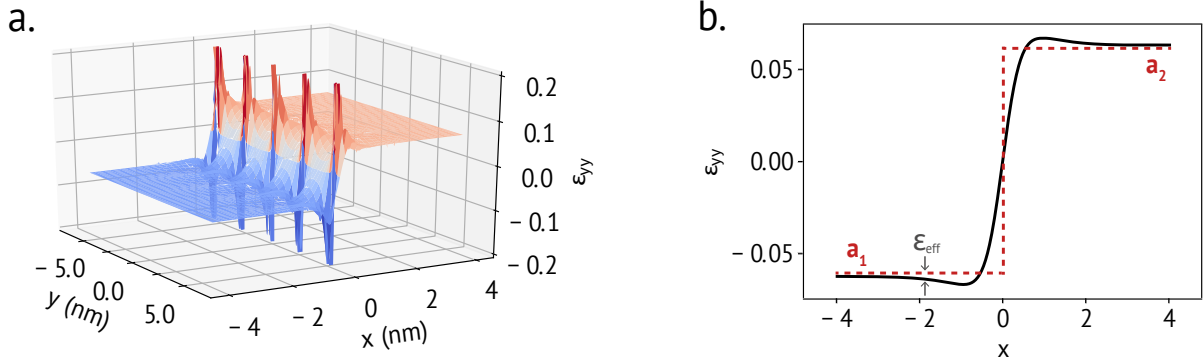


Figure 5.7. **Two Interfacial Scattering Effects Addressed: Acoustic Mismatch and Dislocation Strain** Scattering at a semicoherent heterointerface stems from the periodic strain fields at a misfit dislocation array as well as the step function change in acoustic impedance. (a) Analytic solution for the dilatational strain field component ϵ_{yy} from an infinite array of misfit dislocations periodically spaced along the y -axis [180, pp. 695-697]. (b) Cross-section of 3D dilatational strain field, showing an underlying step function (dotted red line). This is indicating a change in lattice parameter (a) from material 1 to 2, rather than long-range strain. We subtract off the step function in strain, and instead treat this effect with an acoustic mismatch scattering term. This leaves the physical strain (ϵ_{eff}), which we treat with an anharmonic strain scattering potential.

In addition, we predict the thermal resistance to the already well-studied Si-Ge heterointerface and show a close correspondence between our results and those from first-principles methods.

5.4.1. Dislocation Array Scattering Kinematics

Both symmetric twist boundaries and semicoherent heterointerfaces are composed of two dislocation arrays forming a cross-grid. In the twist boundary case, for example, two sets of screw dislocation arrays each shear the crystal to induce a full rotation (see Figure 5.8) [186]. We adopt the configuration in Figure 5.9a, with the x -direction normal to the interface, and two orthogonal dislocation arrays with dislocation lines in the y and z direction. We will refer to the first dislocation array as the YZ array, where the first label (y) indicates the direction of periodicity, and the second label (z) indicates the direction of the dislocation line (see Figure 5.9a). The second array is likewise

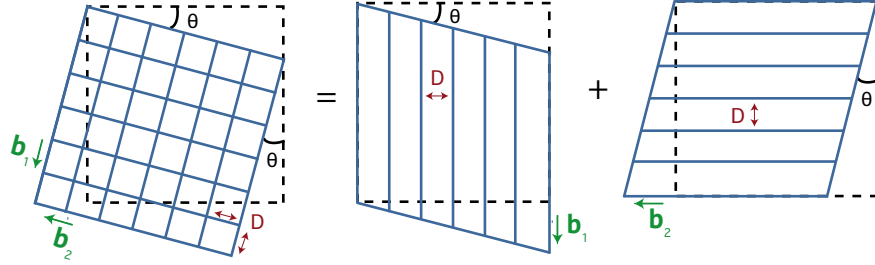


Figure 5.8. **Dislocation Structure of a Symmetric Twist Grain Boundary** Schematic of two orthogonal screw dislocation arrays, with Burgers vectors \mathbf{b}_1 and \mathbf{b}_2 , respectively, producing a twist misorientation (θ) at an interface.

called the ZY array. The scattering potential of the cross-grid is given by summing over the single-dislocation-line scattering potentials (V_1 ; see Section 5.4.2.1) for each array and then combining both:

$$(5.12) \quad V(\mathbf{r}) = \sum_{n=-\infty}^{\infty} V_1(x, y - nD) + \sum_{m=-\infty}^{\infty} V_1(x, z - mD).$$

Here, n and m can assume all integer values from $-\infty$ to $+\infty$. The infinite sums over n and m can be obtained analytically for both the twist and heterointerface cases [180, 187] and are shown in Appendix E. The tilt boundary, instead, is composed of just a single array of edge dislocations, in either the YZ or ZY orientation.

For simplicity, we'll focus on the contribution of the YZ array in the following steps, but analogous expressions can be written for the ZY array, by instead enforcing periodicity in the z -direction. The Fourier transform of this sum of dislocation scattering potentials is:

$$(5.13) \quad \begin{aligned} \tilde{V}_{YZ}(Q_x, Q_y) &= \iint dx dy \sum_{n=-\infty}^{\infty} V_1(x, y - nD) e^{-i(Q_x x + Q_y y)} \\ &= \sum_{n=-\infty}^{\infty} e^{-iQ_y nD} \tilde{V}_1(Q_x, Q_y). \end{aligned}$$

We show the Fourier transform of the scattering potential (\tilde{V}_1) as a function of only Q_x and Q_y , because the scattering vector along the line of the dislocation (Q_z) is necessarily 0. The Poisson summation formula is then applied to explicitly show the Dirac comb:

$$(5.14) \quad \sum_{n=-\infty}^{\infty} e^{-iQ_y nD} = \frac{2\pi}{D} \sum_{n'=-\infty}^{\infty} \delta(Q_y - Q_{n'}), \quad \left(Q_{n'} = \frac{2\pi n'}{D}\right).$$

Hence, \tilde{V}_{YZ} can be written as:

$$(5.15) \quad \tilde{V}_{YZ} = \frac{2\pi}{D} \sum_{n'=-\infty}^{\infty} \delta(Q_y - Q_{n'}) \tilde{V}_1(Q_x, Q_y)$$

$$(5.16) \quad = \frac{2\pi}{D} \sum_{n'=-\infty}^{\infty} \delta(Q_y - Q_{n'}) \tilde{V}_1(Q_x, Q_{n'}).$$

As noted in Hanus *et al.* [181], this equation shows that phonon diffraction peak conditions will occur whenever the magnitude of the scattering wavevector component Q_y equals $2\pi n'/D$ in an infinite interface [188, 189].

The full grid Fourier transformed scattering potential $\tilde{V}(\mathbf{Q})$ is then equal to:

$$(5.17) \quad M(\mathbf{Q}) = 2\pi\delta(Q_z)\tilde{V}_{YZ}(Q_x, Q_y) + 2\pi\delta(Q_y)\tilde{V}_{ZY}(Q_x, Q_z).$$

As enforced by the δ -functions, the scattering due to the YZ array is only non-zero when $Q_z = 0$, while scattering due to the ZY array is only non-zero when $Q_y = 0$. As a result, except when $Q_y = Q_z = 0$, the two dislocation arrays scatter independently (see Figure 5.9b). The Van der Merwe method for calculating interfacial strain energies [187] makes a similar assertion, namely that the energy of both arrays can be reasonably computed separately and then superposed. Specifically analyzing the $Q_y = Q_z = 0$ condition reveals that this scenario must represent either a non-resistive forward scattering case or a mirror-like reflection. The underlying, periodic structure of the interface is washed out at this long-wavelength limit. We treat this scattering separately in

terms of the acoustic impedance mismatch (see Section 5.4.2.2). The total scattering rate Γ is then the sum of the rates due to the YZ and ZY array, as well as that due to acoustic mismatch (AM) (see Equation 5.30):

$$(5.18) \quad \Gamma_{\text{tot}} = \Gamma_{\text{YZ}} + \Gamma_{\text{ZY}} + \Gamma_{\text{AM}}.$$

Here, Γ_{YZ} entails only $|\tilde{V}_{\text{YZ}}|^2$, Γ_{ZY} entails only $|\tilde{V}_{\text{ZY}}|^2$, and Γ_{AM} entails only $|\tilde{V}_{\text{AM}}|^2$ (see Equations 5.24 and 5.30). To avoid misunderstanding, we note that the resemblance of Equation 5.18 to Matthiessen's Rule is superficial. The Γ_{AM} component does not represent a separate scattering channel but rather a completely independent kind of interface scattering, which is, in addition, activated at a different frequency regime.

Finally, invoking Equations 2.22 and 2.23 from the Introduction Section 2.2.2, the scattering rate Γ_{YZ} due to periodic strain from the YZ array is:

$$(5.19) \quad \Gamma_{\text{YZ}}(\mathbf{q}) = \frac{n_b}{\hbar^2 D^2} \sum_{n'=-\infty}^{\infty} \iiint d^3 \mathbf{q}' \delta(Q_z) \delta(\omega_{\mathbf{q}} - \omega_{\mathbf{q}'}) \left| \tilde{V}_{\text{YZ}}(Q_x, Q_y) \right|^2 (1 - \hat{\mathbf{q}} \cdot \hat{\mathbf{q}}').$$

Here, n_b is equal to $1/L_x$, and represents the linear density of boundaries in the material. The result for Γ_{ZY} is similar.

The phase space term is implicitly enforced by the momentum and energy conservation laws imposed by the δ -functions. These conservation rules restrict this integral to a discrete set of available \mathbf{q}' states. Equations S42 - S48 of Hanus *et al.* [181] re-express these δ -functions explicitly in terms of \mathbf{q}' to arrive at the final expression for Γ :

$$(5.20) \quad \Gamma_{\text{YZ}}(\mathbf{q}) = \frac{n_D}{\hbar^2 v_g D^2} \sum_{n'=-\infty}^{\infty} \sum_{\sigma=\pm} \frac{(q_x^2 \mp q_x(q_x^2 + 2q_y Q_{n'} - Q_{n'}^2)^{1/2} + q_y Q_{n'})}{q(q_x^2 + 2q_y Q_{n'} - Q_{n'}^2)^{1/2}} \left| \tilde{V}_1(Q_{x,n'\sigma}, Q_{n'}) \right|^2.$$

This is the working formula that we use for numerical calculation of scattering rate due to the YZ-array of dislocations, and equivalently for the ZY-array by switching the y and the z components.

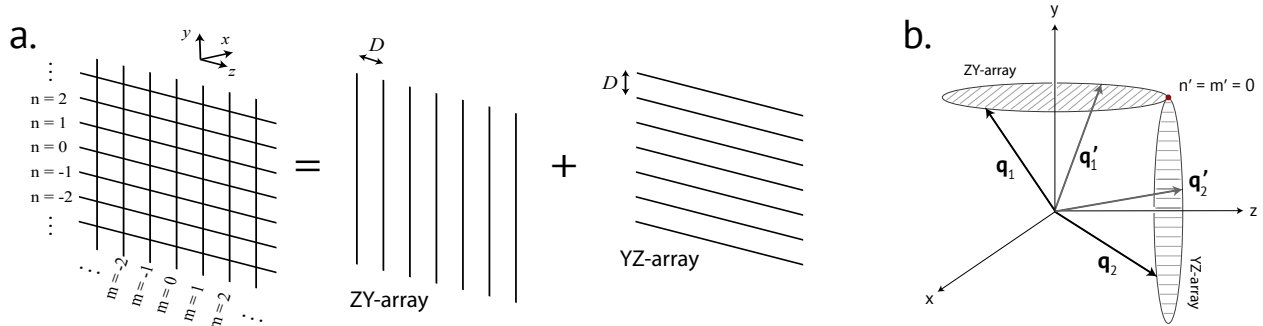


Figure 5.9. **Diagrams of Dislocation Grid and Associated Scattering Phase Space** (a) Diagram of orthogonal YZ and ZY arrays in dislocation cross-grid. In this case, equal D spacing is assumed for both. (b) Phase space diagram portraying the independent scattering of the YZ and ZY dislocation array, which overlap only at the $\mathbf{Q}_{\parallel} = 0$ ($n' = m' = 0$) condition.

Finally, to get the spectral relaxation time, we must average over the incident phonon wavevector direction \hat{q} . We compute $\tau(\omega)$ as the weighted orientational average of the inverse scattering rate,

$$(5.21) \quad \tau(\omega) = \frac{\iint \Gamma^{-1} q_x^2 d\Omega}{\iint q_x^2 d\Omega} = \frac{3}{4\pi} \iint \Gamma^{-1} \frac{q_x^2}{q^2} d\Omega,$$

This section handled the scattering constraints imposed by defect geometry, and the final step is to define scattering potentials from the interface properties. In the next section, we derive an anharmonic scattering potential from the interfacial dislocation strain fields, as well as a scattering potential from acoustic mismatch, which couples to phonons via harmonic elastic constants.

5.4.2. Scattering Potentials

5.4.2.1. Dislocation Strain Potential. The real-space strain scattering potential or lattice energy perturbation is directly related to the induced internal strain $\epsilon(\mathbf{r})$ at the interface via an anharmonic coefficient, which in this case is the Grüneisen parameter ($\gamma = (1/\omega)d\omega/d\epsilon$). A single Grüneisen parameter approximation is made wherein γ is frequency and mode-independent, so that the change in phonon frequency due to internal strain is $\omega\gamma\epsilon(\mathbf{r})$. This approximation may lead to an underestimation of the phonon scattering, but trends with misorientation and comparisons of

grain boundary geometry should still hold [56, 181]. The scattering potential due to the strain from a single interfacial dislocation, $\epsilon_1(\mathbf{r})$, is:

$$(5.22) \quad V_1(\mathbf{r}) = \hbar\omega\gamma\epsilon_1(\mathbf{r}).$$

We use the dislocation strain fields from continuum elasticity theory as given, for example, by Hirth and Loethe [190, pp. 60, 76]. As discussed in the previous section, the sum over single-line-dislocation potentials is facilitated in Fourier space, so all we require is the Fourier transformed strain fields for a single screw and misfit-edge dislocation.

Starting with the symmetric twist boundary, we will maintain the geometry of the previous section with the x -direction normal to the interface and dislocation arrays with sense vectors oriented along the y and z directions. The strain state of a twist boundary is pure shear, such that all components ϵ_{ii} are 0. Only two independent components of the strain tensor are non-zero for each dislocation array. Table 5.1 lists the strain component Fourier transforms for a constituent screw dislocation in either the YZ or ZY array:

Table 5.1. **Twist Boundary Fourier Strain Field Components**

YZ array	ZY array
$\tilde{\epsilon}_{13} = \frac{ibQ_y}{2(Q_x^2 + Q_y^2)}$	$\tilde{\epsilon}_{12} = -\frac{ibQ_z}{2(Q_x^2 + Q_z^2)}$
$\tilde{\epsilon}_{23} = -\frac{ibQ_x}{2(Q_x^2 + Q_y^2)}$	$\tilde{\epsilon}_{23} = \frac{ibQ_x}{2(Q_x^2 + Q_z^2)}$

The semicoherent heterointerface will also be defined in the yz -plane with two interpenetrating arrays of dislocations with misfit edge character [191]. As in the symmetric tilt boundary case outlined in Ref. [181], the deformation tensor is broken down into dilatational strain (ϵ_Δ), shear strain (ϵ_S), and rotation (ϵ_R), which act as independent scattering sources. Table 5.2 lists the Fourier strain components for a single misfit edge dislocation in both the YZ and ZY arrays.

Table 5.2. **Heterointerface Fourier Strain Field Components**

YZ array	ZY array
$\tilde{\epsilon}_\Delta = \frac{ib(1-2\nu)}{(1-\nu)} \frac{Q_x}{(Q_x^2 + Q_y^2)}$	$\tilde{\epsilon}_\Delta = \frac{ib(1-2\nu)}{(1-\nu)} \frac{Q_x}{(Q_x^2 + Q_z^2)}$
$\tilde{\epsilon}_S = \frac{-ib}{(1-\nu)} \frac{Q_y Q_x^2}{(Q_x^2 + Q_y^2)^2}$	$\tilde{\epsilon}_S = \frac{-ib}{(1-\nu)} \frac{Q_z Q_x^2}{(Q_x^2 + Q_z^2)^2}$
$\tilde{\epsilon}_R = \frac{-2ibQ_y}{(Q_x^2 + Q_y^2)}$	$\tilde{\epsilon}_R = \frac{-2ibQ_z}{(Q_x^2 + Q_z^2)}$

These strain fields are related to those of the tilt boundary by a simple rotation, which places the extra half plane along the x -axis, perpendicular to the boundary. For example, a tilt boundary perpendicular to the x -direction with dislocations spaced along the y -direction, could be described by the YZ-array strain fields if Q_x and Q_y are exchanged.

Figure 5.7 shows a normal component of the strain field from a single misfit dislocation array, and the cross-section reveals a step function change in the dilatation at the interface [180, pp.695-697]. In fact, setting $Q_y = 0$ in the YZ array or $Q_z = 0$ in the zy array, yields $\tilde{\epsilon}_\Delta \propto i/Q_x$, which is precisely the Fourier transform of the Heaviside step function. This long range dilatational strain effect is artificial, since the reference lattice parameter differs on either side of the interface. Therefore, the dilatational strain at the long-wavelength limit is subtracted and treated via the acoustic impedance mismatch term described by Equation 5.24.

Recently, Varnavides *et al.* introduced the strain mismatch model (SMM) [38], providing an *ab initio* framework for inelastic phonon scattering due to an interfacial strain perturbation. The SMM method is applied to treat a similar physical system, studying the dilatational strain scattering from a misfit dislocation array. By following the treatment of Carruthers (Eq. 4.91 of Ref. [188]), the derived scattering rate is found to be independent of the dislocation spacing, and as far as we can interpret, neglects the periodic strain fields local to the interface, which we find to be important in this work. Both previous works [38, 188] additionally treat the step-change in dilatation at a

misfit dislocation array as a source of anharmonic strain scattering, which differs from the acoustic mismatch approach taken here and described in the following section.

5.4.2.2. Acoustic Mismatch Scattering Potential. The origin of the acoustic mismatch differs between a hetero- and homointerface. In the case of the semicoherent heterointerface, the acoustic impedance mismatch stems from the change in material, and resulting change in elastic tensor, across the interface. In a tilt or twist boundary, the long-range rotational deformation induces acoustic mismatch through the anisotropy of the acoustic properties. The rotation at a grain boundary is described by a single misorientation angle θ (see Figure 5.8), which in the Read-Shockley model, relates to the magnitude of the Burger's vector (b) and the dislocation spacing (D) as: $2\tan(\theta/2) = b/D$ [180, p. 688]. For a fixed phonon angle of incidence, the crystal rotation can be interpreted as a change in the acoustic impedance stemming from the rotation of the stiffness tensor.

For both grain boundaries and heterointerfaces, we can derive an acoustic mismatch scattering potential in order to compute a squared scattering matrix element and scattering rate via Fermi's Golden Rule following the basic procedure outlined in Section 2.2.2. This scattering potential is grounded in the same physics as the classical acoustic mismatch model (AMM; see Section 5.3.1) [171].

We define the scattering potential as the change in energy of a phonon as it traverses an interface, which can be expressed in terms of the change in phonon phase velocity Δv_p and incident phonon wavevector magnitude q ,

$$(5.23) \quad V_{AM}(\mathbf{r}) = \hbar\Delta\omega(\mathbf{r}) = \hbar\Delta v_p(\mathbf{r})q.$$

The spatial dependence of $\Delta v_p(\mathbf{r})$ is taken as $\Delta v \Theta(x)$ where $\Delta v = v_2 - v_1$ is the magnitude of the phonon velocity change from side 1 to side 2, and $\Theta(x)$ is the Heaviside step function. Since

its Fourier transform is $\tilde{\Theta}(Q_x) = i/(Q_x)$,

$$(5.24) \quad \tilde{V}_{\text{AM}} = \hbar \Delta v q \tilde{\Theta}(Q_x) = \hbar \Delta v \frac{iq}{Q_x}.$$

The magnitude of the velocity change Δv depends on the phonon angle of incidence and the degree of misorientation at a grain boundary or homointerface, and, at a heterointerface, the additional change in elastic tensor. The Christoffel equations relate the stiffness matrix to the direction-dependent acoustic velocities in a material. The equation is essentially the classical limit of the lattice dynamical matrix diagonalization. The Christoffel matrix C is obtained from the rank 4 stiffness tensor c_{ijkl} for a unit vector \hat{n} denoting the phonon direction of propagation as follows [27]:

$$(5.25) \quad C_{ij} = \sum_{jk} n_j c_{ijkl} n_k.$$

From this, one can then evaluate the following eigenvalue problem to arrive at the phase velocity v_p of an acoustic phonon travelling in the direction \hat{n} with polarization vector \hat{s} :

$$(5.26) \quad \sum_{ij} (C_{ij} - \delta_{ij} v_p^2) s_j = 0.$$

By solving this equation for different \hat{n} , it is possible to generate a slowness surface, or diagram of the direction-dependent group (v_g) or phase velocity (v_p) of the acoustic phonons in a material. As discussed in Jaeken *et al.* [27], the acoustic v_g and v_p differ slightly in terms of direction alone, as described by the power flow angle Ψ , where $v_p = v_g \cos \Psi$. The group velocity direction indicates the direction in which energy travels, which can deviate from the wavefront propagation direction described by the phase velocity. Using the `christoffel` Python package [27], we compute the group velocity slowness surfaces for the three phonon polarizations of Si (Figure 5.10).

From these direction-dependent velocities, we can calculate Δv for an incoming phonon and capture the acoustic mismatch due to any grain boundary misorientation or change in elastic

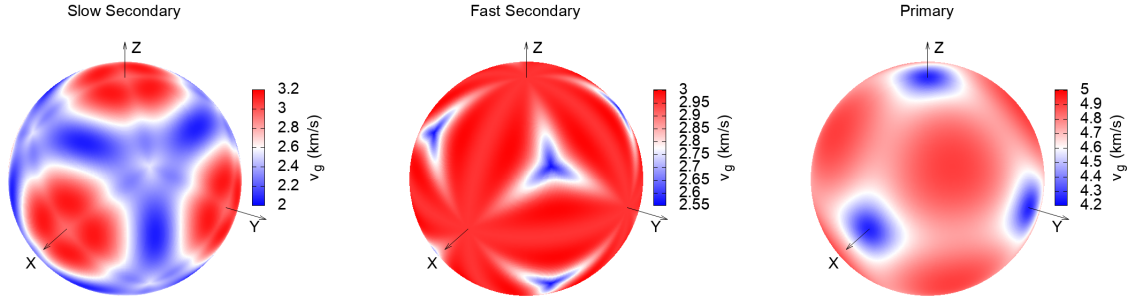


Figure 5.10. **Group velocity Slowness Plots for Silicon** Direction dependence of the acoustic phonon group velocities plotted on a unit sphere. Fast/slow secondary correspond approximately to the two transverse branches, and primary is approximately the longitudinal branch. Produced using the `christoffel` package [27].

coefficients, regardless of crystal symmetry. Our implementation lies within the continuum, long-wavelength limit, and so V_{AM} computed using the magnitude of either the group or the phase velocity yields the same result given that the perturbation is set only by the change in phonon frequency. The acoustic mismatch constitutes planar defect scattering and, as mentioned previously, will produce a specular reflection. Since forward scattering does not contribute to the scattering rate, Q_x in Equation 5.24 will simplify to $2q_x = 2|q|\sin\theta\cos\phi$.

As discussed in Section 5.2.1, the Kapitza resistance is a quantity defined through the Landauer formalism, in which each heat-carrying phonon is assigned a transmission coefficient at the interface. As a result of this interfacial resistance, a heat flux across the interface will cause a proportional temperature drop ΔT localized to the interface (blue temperature profile in Figure 5.11a). In contrast, the perturbation potential derived in this section produces a scattering rate that influences the overall phonon lifetime and affects the thermal conductivity of the sample homogeneously (red temperature profile in Figure 5.11a). Given these unique descriptions, it is worth comparing the phonon transmission coefficients produced by our perturbation theory treatment to that of the classical acoustic mismatch model (described in Section 5.3.1). We first derive a scattering rate due to the acoustic mismatch scattering potential (Equation 5.24). Note that the phase space term is the phonon density of states on side 1 of the interface, since the incident phonon will reflect back to the same side it originated from.

$$\begin{aligned}
\tau^{-1}(\mathbf{q}) &= n_d |S|^2 g_1(\omega_{\mathbf{q}}) \\
&= [1/L_z] \left[i\hbar \frac{\Delta v}{\cos\theta \sin\phi} \right]^2 \left[\frac{1}{\pi v_1} \right] \\
(5.27) \qquad &= \frac{2\Delta v^2}{v_1 (\cos\theta \sin\phi)^2}
\end{aligned}$$

Then, Equation 5.21 is used to arrive at the spectral scattering rate, yielding the expression:

$$(5.28) \qquad \tau_{12}(\omega) = \frac{3}{2} L_x v_1 \Delta v^2.$$

which is finally converted to a spectral transmission coefficient using Equation 5.6 to yield the final expression:

$$(5.29) \qquad t_{\text{Pert}} = \frac{1}{\frac{1}{2} \left(\frac{\Delta v}{v} \right)^2 + 1}.$$

This transmission coefficient is compared to Equation 5.3.1 for the classical acoustic mismatch model [143, 150] in Figure 5.11b. The two approaches differ by less than 5% up to fractional acoustic velocity changes of $|\Delta v/v| = 0.5$, which typically exceeds the acoustic mismatch present at solid-solid interfaces.

Finally, the square of the Fourier space scattering potential must be taken in the calculation of the matrix element (M). In the work of Brown [192], it was shown that symmetry constraints in the cubic crystal enforce that strain and rotation contribute independently to the scattering potential. We reach the same conclusion in our work by noting the distinct scattering physics of strain (diffractive scattering) and rotation (specular reflection). As a result, there are no non-zero cross-terms when we take the square and the full, squared scattering potential can be written as,

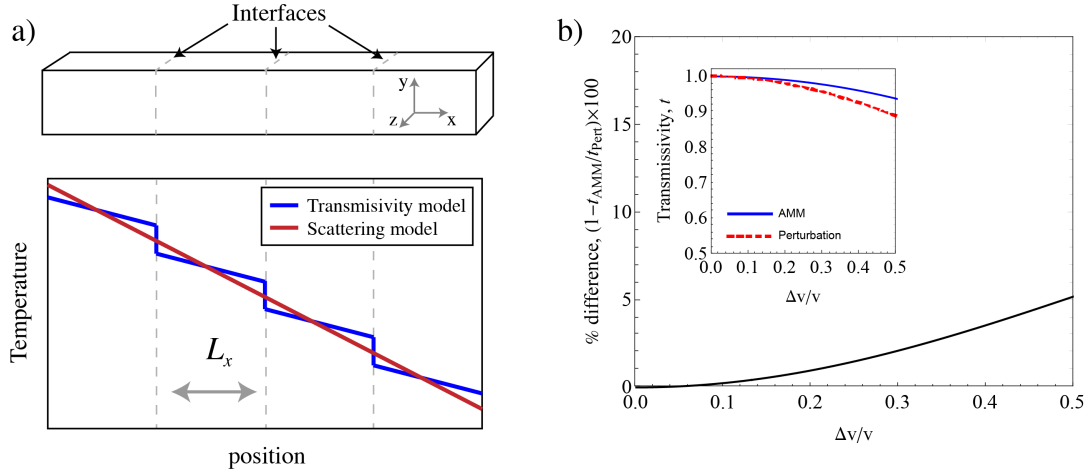


Figure 5.11. **Comparison between Acoustic Mismatch Perturbation Potential and Classical Method.** a) (copy of Figure 5.1) A schematic illustration of two common models used to describe heat conduction in materials with interfaces. The blue line depicts the Landauer based model where a thermal boundary resistance arising from the conduction channel having a interfacial transmission probability or $t(\omega) > 0$, induces a sharply localized drop in temperature. The red line depicts a model based on phonon scattering theory and Matthiessen's rule, where each scattering mechanism contributes a scattering rate $(\tau(\omega)^{-1})$, and together modify the materials thermal conductivity homogeneously. b) A comparison between the transmissivity calculated using classical acoustic mismatch (AMM) theory and the interface perturbation theory, showing that the two cases differ by no more than 5% up to $\Delta v/v = 0.5$.

$$(5.30) \quad |\tilde{V}(\mathbf{Q})|^2 = |\hbar\omega\gamma\tilde{\epsilon}(\mathbf{Q})|^2 + |\hbar\Delta v\tilde{\Theta}(x)q|^2.$$

Our treatment agrees with the conceptual conclusions from the work of Brown [192], which suggests that rotations of the crystal scatter phonons via harmonic elastic constants (e.g. v_s) while strain scatters via third order, anharmonic constants (e.g. γ) [192].

5.4.3. Symmetric Tilt and Twist Grain Boundaries

The results discussed here describe Si-Si symmetric twist and tilt. boundaries with various twist angles θ , and were calculated using the Si parameters in Table E.1.

The previous investigation of tilt grain boundaries showed a cross-over in the frequency-dependence of the phonon lifetime from frequency-independent scattering at long wavelengths to $\tau \propto \omega^{-1}$ at shorter wavelengths [181]. This frequency-dependence is in stark contrast to other classical theory such as the grey model (see Section. 5.3.1), which suggests that the lifetime should be primarily limited by the average grain size, and therefore frequency independent. However, the $\tau \propto \omega^{-1}$ relation was essential to explain the anomalous low-temperature thermal conductivity trend of $\kappa \propto T^2$ in polycrystalline materials (in contrast to the $\kappa \propto T^3$ expected for single crystals or ω -independent scattering) [181, 193–195].

Here, we show that the twist boundary exhibits the same cross-over in the frequency-dependence of the relaxation time (τ) [181]. Long-wavelength phonons view the boundary as a planar defect defined by the rotational deformation, leading to the expected frequency-independent scattering. Note the the phase space for planar defect scattering is the frequency-independent 1D density-of-states (Figure 2.3). The relaxation time at this long wavelength, or low frequency, limit is plotted versus grain boundary angle in Figure 5.13c and is seen to vary periodically with angle θ . This periodic relationship has been predicted previously and is a result of the symmetry of the Si acoustic properties [192]. Short wavelength phonons, however, interact with the underlying periodic strain from the dislocation grid and pick up a phonon frequency dependence approaching $\tau \propto \omega^{-1}$ (Figure 5.13b). Again, note that dislocations, as linear defects, contribute a phase space term to the scattering rate equal to the 2D density of states, which scales with frequency (Figure 2.3). At the short wavelength limit, the lifetime varies monotonically with misorientation angle. As a net result, the overall thermal boundary resistance increases linearly with grain boundary angle because of the increasing strain scattering effects.

Figure 5.12 shows the phonon scattering rate plotted versus the incident angle of the incoming phonon for a twist boundary. It provides a visual representation of the rotation versus strain scattering effects. At high frequency, the diffraction effects stemming from the periodic dislocation array are visible as patterns in the directional plot of scattering rate. Whereas at low frequency,

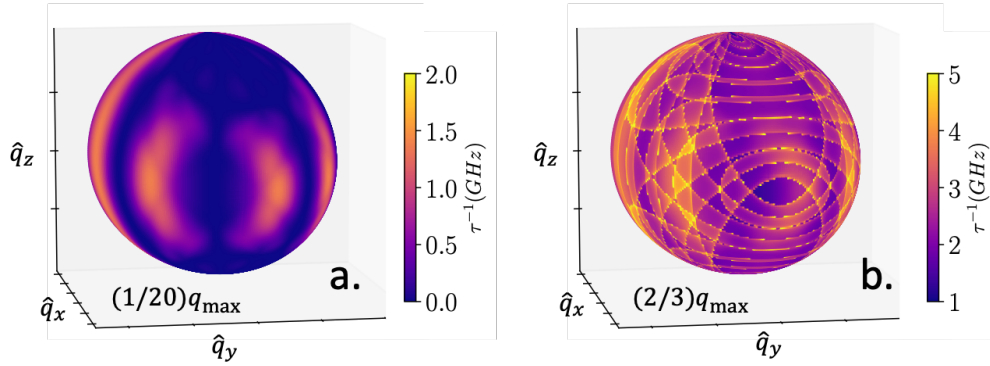


Figure 5.12. **Relaxation Time versus Incident Phonon Direction** Three-dimensional polar plots of the scattering rate $\tau^{-1}(\mathbf{q})$ (in GHz) versus incident angle (θ_i, ϕ_i) of an incoming phonon, holding phonon frequency constant. The results shown correspond to a twist boundary with $\theta = 5^\circ$ at the (a) long wavelength limit ($q = q_{\max}/20$), where acoustic mismatch scattering dominates and the (b) short wavelength limit ($q = (2/3)q_{\max}$), where the periodic strain field scattering effect is picked up.

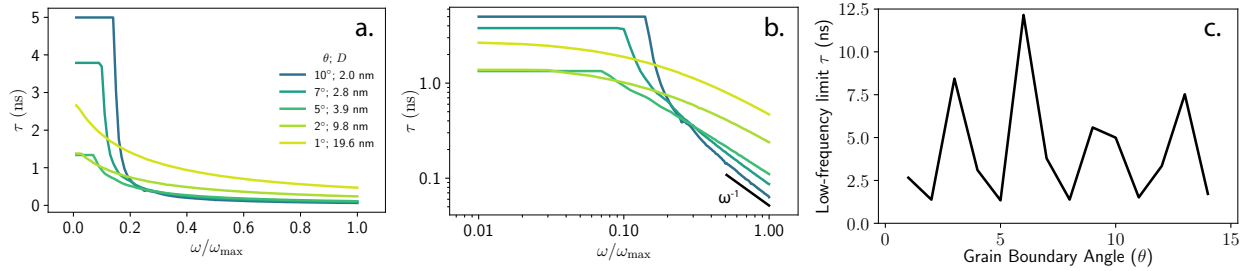


Figure 5.13. **Si Twist Boundary Phonon Lifetime Predictions** (a) Spectral phonon lifetimes for a Si-Si twist interface at various misorientation angles (b) The log-log plot of this relaxation time shows a power law crossover from ω -independent to $\sim \omega^{-1}$, indicating a transition from planar-defect to linear-defect scattering. (c) The long-wavelength limit of the relaxation time is plotted against grain boundary angle, revealing a periodic variation stemming from the symmetry of the acoustic velocities.

there are more isolated and broad scattering “hot spots” corresponding to ranges in the phonon angle of incidence which undergo large scattering due to an acoustic impedance mismatch.

In Figure 5.14, we compare the scattering properties from a twist and tilt grain boundary. In both grain boundary types, the rotational scattering is calculated from Equation 5.24 using the grain boundary angle θ to determine the phonon velocity change at the interface. It should be kept in mind, however, that in the tilt case, the rotation is perpendicular to the plane of the interface. The spectral τ in both cases is approximately equal at the long-wavelength limit as a result of the cubic

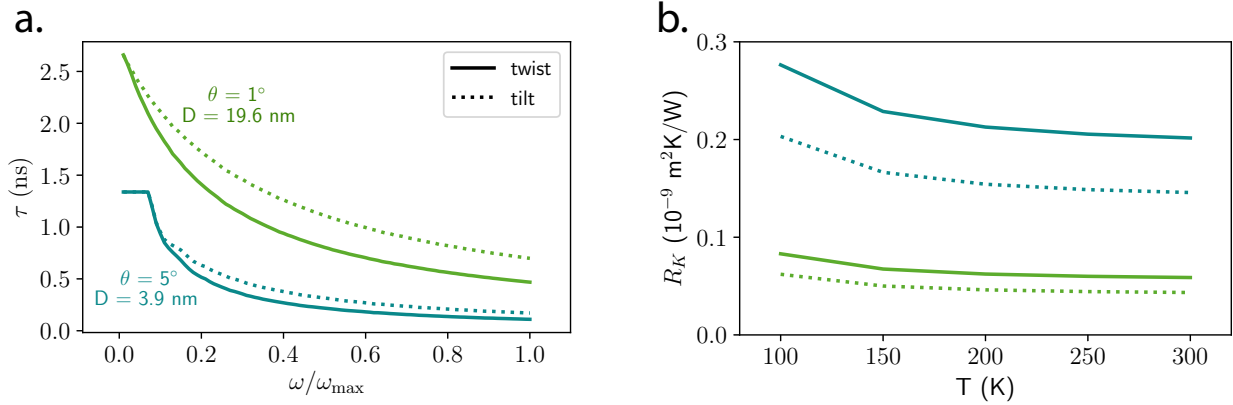


Figure 5.14. **Comparison of Si Tilt and Twist Grain Boundary Scattering** (a) The spectral relaxation time (τ) converges at the long-wavelength limit, but decreases faster in the frequency-dependent regime for the twist boundary, when dislocation strain scattering is activated. (b) The twist boundary, therefore, is predicted to have about $1.3\times$ the thermal boundary resistance (R_K).

symmetry of the Si stiffness matrix and acoustic velocities (Figure 5.10). However, for the twist boundary, the relaxation time decreases more rapidly with frequency in the dislocation scattering regime (Figure 5.14a). In the work of Van der Merwe [187], a linear elasticity model for interfacial stresses and energies is applied to a generic material with cubic or tetragonal symmetry, and shows that for the same misorientation angle θ , twist boundaries exhibit slightly higher strain energy than tilt boundaries. The higher strain energy of the twist boundary can explain the reduced relaxation times at high phonon frequency, which leads to about $1.3\times$ the thermal boundary resistance of the tilt boundary (Figure 5.14b). Additionally, previous works comparing individual screw and edge dislocation scattering show that screw dislocations have higher strain energy and are therefore more thermally resistive [196].

The R_K from the Si-Si twist boundary model (Equation 5.4) is close to, although consistently lower than, previously reported molecular dynamics simulation results (see Table 5.3). We also compare model predictions against R_K measurements of Si-Si twist boundaries using the 3ω method, an AC technique suited for thermal conductivity measurements of films, reported in Xu *et al* [182]. In both cases, the magnitude of the thermal resistance depends on twist angle, and the R_K ratio between the 6.9° and 3.4° twist boundaries is similar. However, the measured thermal resistance

is more than an order of magnitude larger than the model predictions. The model assumes a clean interface, while the interface in the physical material serves as a sink for additional defects and may contain roughness or oxidation effects [197, 198]. In this particular experiment, a Si thin film was bonded to a Si substrate at varying twist angles. TEM images revealed a nanometer-thick disordered region at the boundary, which contributed additional thermal resistance [182, 199, 200].

A detailed modeling of these contributions is necessary to understand the experimental results.

A benefit of our approach is the ability to differentiate between the scattering contributions of the rotational deformation and the dislocation strain. The percentage contribution of the acoustic mismatch effect to R_K is only about 4-5% for most symmetric twist boundaries, and dislocation strain accounts for the rest of the scattering. This breakdown illustrates the significant role of the interfacial dislocation structure in the thermal resistance, and may also help to explain the very low R_K values observed for twin boundaries both experimentally [201] and in non-equilibrium molecular dynamics [202]. Twin boundaries are special coherent interfaces, which have a misorientation without dislocations or disregistry. Based on the R_K breakdown determined here, we might expect twin boundaries to have just 5% of the R_K exhibited by twist or tilt grain boundaries.

Table 5.3. **Si Twist Boundary Thermal Boundary Resistance** Thermal boundary resistance (R_K ; $\text{m}^2\text{K}/\text{GW}$) comparison to previous theoretical and experimental literature results for the Si-Si symmetric twist boundary.

		Literature R_K	This Study R_K
T (K)	Angle θ	MD [171, 203, 204]	Born von Karman
500	11.42°	0.61, 0.76, 1.1	0.30
		Experimental [182]	
300	6.9°	9.0	0.21
300	3.4°	6.7	0.13
300	$\frac{R_K(6.9^\circ)}{R_K(3.4^\circ)}$	1.3	1.6

Finally, experimental investigations of twist boundary R_K show a correlation with the Read-Shockley grain boundary energy [179], which captures the strain energy produced by the dislocation structure at the grain boundary [182, 183]. This observation corroborates the idea that dislocation

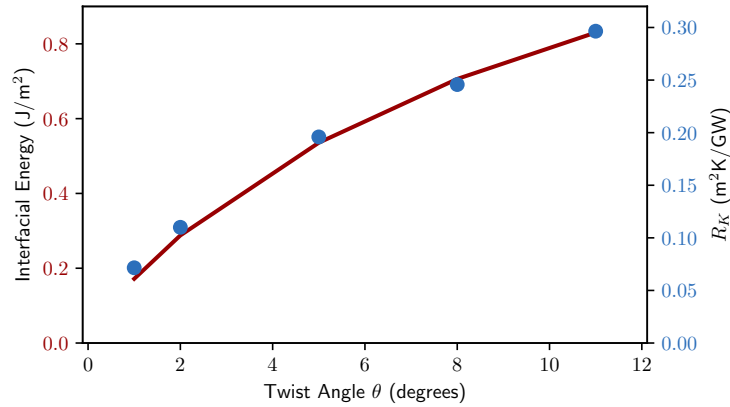


Figure 5.15. **Thermal Boundary Resistance correlates with Read-Shockley (R-S) Grain Boundary Energy** Twist boundary model predictions of the thermal boundary resistance (R_K) are shown as blue scatter points (mapped to right axis) and closely follow the Read-Shockley interfacial energy (red line; mapped to left axis). Both additionally trend with misorientation angle θ for low angle grain boundaries. Similar trends between R_K , R-S energy, and θ have also been shown through experiment and simulation [170, 183].

strain is essential to understand the origins of interfacial thermal resistance. The Read-Shockley grain boundary energy is given by:

$$(5.31) \quad E = \frac{Gb}{4\pi(1-\nu)}\theta(A - \ln(\theta)),$$

with dependencies on the misorientation angle θ , Burgers vector b , bulk modulus G , and Poisson ratio ν . The A factor captures the ratio between the dislocation core energy and strain energy contributions at the grain boundary. We set A equal to 0.23, following the previous work of Tai *et al.* [183], for the simple purposes of demonstrating the correlation with R_K . As shown in Figure 5.15, R_K from the twist boundary model closely trends with the Read-Shockley strain energy, as expected.

5.4.4. Semicoherent Heterointerfaces

The calculations below are performed for a Si-Ge interface using the parameters found in the Appendix Table E.1. As in the tilt and twist boundary examples, the heterointerface relaxation

time crosses over between planar-defect and linear-defect scattering. However, as expected due to the larger acoustic mismatch, the thermal resistance is significantly larger than in the twist boundary case. The acoustic mismatch effect alone, however, contributes only about 50% of the full thermal boundary resistance (see Figure 5.16) predicted by the model, indicating a significant contribution of misfit dislocation strain scattering to the thermal resistance.

Table 5.4 shows the thermal boundary resistance (R_K) results of our method assuming a Born-von Karman (BvK) model for the phonon dispersion. The results show good agreement with previous calculations on Si-Ge heterojunctions using the diffuse mismatch model (DMM) and molecular dynamics (MD) simulations [149]. In the diffuse mismatch model, the overlap in the phonon density of states on either side of the interface determines the transmission probability. In contrast, the molecular dynamics simulation uses no model or assumption about the phonon scattering mechanism. We compare to the results from the largest simulation cell trialled in each of the previous MD studies [205,206]. Our results are also in line with the atomistic Green's function (AGF) approach, which circumvents the lattice dynamical matrix equation, and instead studies the impulse response of the system [65]. The AGF work additionally studied the influence of alloying at the interface and observed that R_K doubles with an alloy layer of just 1 nm. Finally, in the scattering mismatch model (SMM) [38], phonon transmission coefficients are evaluated through an iterative solution of the phonon Boltzmann transport equation to predict R_K . The SMM predicts a larger R_K , likely due to the first-principles anharmonicity treatment and differences in the treatment of the dilatation at the interface (see Section E.3).

The thermal boundary resistance R_K of the Si-Ge interface has also been investigated experimentally. The through-film thermal conductivity of superlattice films can be converted to a value for R_K by assuming that bulk phonon scattering is negligible [38], and the results for the largest reported period L (i.e. thickness of interlayers) are summarized in Table 5.4. While the R_K calculated here is comparable to the superlattice measurements, it is important to note that its value is affected by the coherent phonon dynamics present in superlattices. Additionally, Wang *et al.* [154] measured the R_K of a Si film bonded to a Ge substrate using the 3ω method, and report an order of magnitude

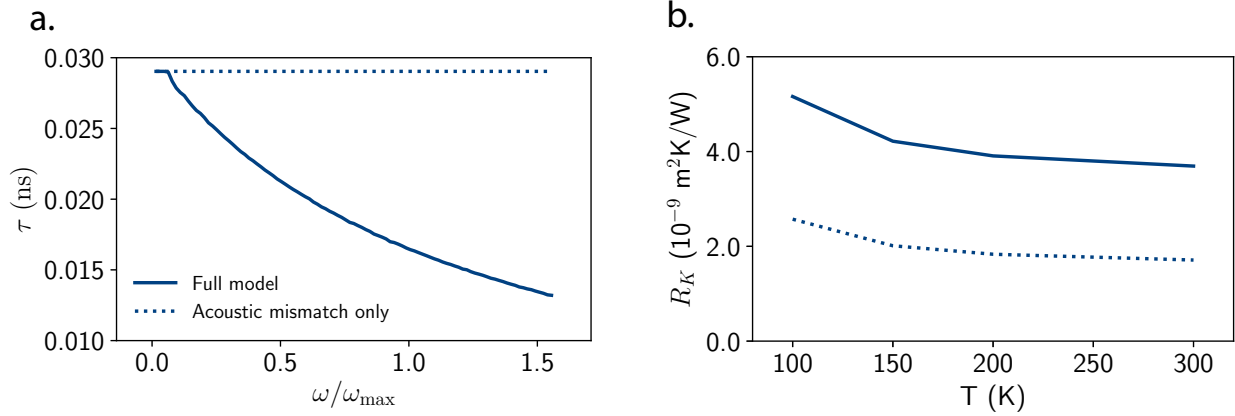


Figure 5.16. **Si-Ge Heterointerface Phonon Lifetime and Kapitza Resistance Predictions** Si-Ge heterointerface scattering using a Born-von Karman phonon dispersion (a) Spectral lifetime for a Si-Ge heterointerface with a misfit dislocation spacing of 7 nm, comparing model with acoustic mismatch and dislocation strain (solid) to the model with acoustic mismatch alone (dotted) (b) Thermal boundary resistance predictions versus temperature from the heterointerface model with (solid) and without (dotted) dislocation strain scattering. Dislocation strain accounts for 50% of the overall thermal resistance.

larger thermal boundary resistance. In their study, however, a ~ 3 nm alloy layer is shown to form with additional interdiffusion persisting for ~ 10 nm around the interface, and this alloying effect predominates the interfacial thermal resistance. Interface quality can therefore have order of magnitude effects on the thermal transport [207].

Table 5.4. Room temperature thermal boundary resistance (R_K ; $\text{m}^2\text{K}/\text{GW}$) with comparison to theoretical and experimental literature results for Si-Ge heterointerface

Computational or Theoretical							
This work	Ref. [150]	Ref. [205]		Ref. [206]		Ref. [38]	Ref. [208]
BvK	AMM	MD	DMM	MD	DMM	SMM	AGF
3.75	1.8	2.83	2.40	3.00	3.71	5.22	3.36
Experimental (3ω method)							
Ref. [182]		Ref. [209]		Ref. [210]			
Bonded Films		Superlattice ($L = 14$ nm)		Superlattice ($L = 15$ nm)		Superlattice ($L = 27.5$ nm)	
31.4		2.14		3.62		6.28	

5.5. Additional Interfacial Dislocation Scattering Effects: Core Scattering and Phonon Drag

5.5.1. Dislocation Core Scattering

Thus far, the discussion of dislocation scattering has focused only on the dislocation strain fields present at the interface, neglecting the impact of the atomic disregistry at the center of the dislocation, or the dislocation core. Original works by Klemens and Carruthers suggest that dislocation core scattering at the interface is negligible, since dislocation strain scattering dominates for most of the phonon frequency spectrum, except perhaps close to the Debye frequency, such that the majority of phonons are scattered at some distance from the dislocation core [39, 56, 188]. To verify that dislocation core scattering does not impact our model predictions, we compute the core scattering potential for an interfacial dislocation array.

To calculate the scattering from a dislocation core, the core can be modelled as a line of vacancies with mass contrast $\Delta M = 3M$ [56]. For a YZ array of dislocations (i.e. periodically spaced along the y-direction and with sense vectors along the z direction) the scattering potential due to this source of mass contrast would be:

$$(5.32) \quad V_1(x, y, \omega) = \frac{1}{2} \frac{\Delta M}{M} \hbar \omega S_0 \delta(x) \delta(y) = \frac{3}{2} \hbar \omega V_0^{2/3} \delta(x) \delta(y - nD)$$

The perturbation potential takes the form of a Dirac comb with a period of D . By invoking the Poisson summation formula just as before, we can show that the Fourier transform is also a Dirac comb with a period of $\frac{2\pi}{D}$:

$$(5.33) \quad \tilde{V}_{YZ}(\mathbf{Q}) = \sum_{n'} \delta(Q_y - \frac{2\pi n'}{D}) \frac{3}{2} \hbar \omega V_0^{2/3}$$

The scattering potential can then be input into Equation 5.19 to calculate the scattering rate due to interaction with the array of dislocation cores.

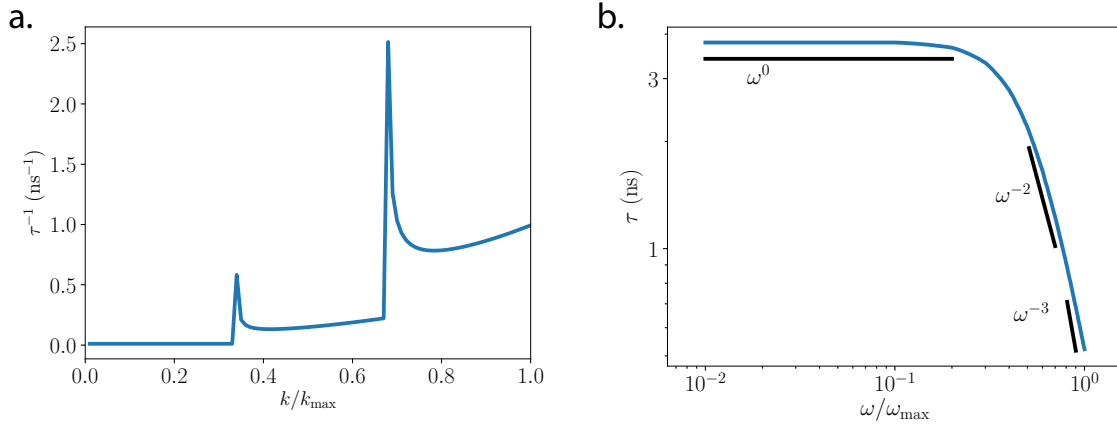


Figure 5.17. **Diffraction Effects and Dimensionality Crossover in Dislocation Core Arrays** Phonon lifetimes including the effects of dislocation core and acoustic mismatch scattering for a 7° symmetric Si twist boundary. (a) Scattering rate plot for a phonon of normal incidence to the interface. Diffraction peaks occur at intervals of $|k| = 2\pi n/D$, where there is a spike in the number of allowed phonon transitions. (b) The log-log plot of the spectral relaxation time depicts smooth cross-over between ω -independent scattering (signature of planar acoustic mismatch scattering) and ω^{-3} scattering (signature of dislocation core scattering). An intermediate regime with ω^{-2} scattering may also be present, in which long wavelength phonons view the array of dislocation cores as a planar mass defect.

Just as before with the periodic dislocation strain problem, the array of dislocation cores can exchange quantized amounts of momentum with incident phonons in the direction of periodicity, yielding another case of diffractive scattering (Figure 5.17a).

Once again, we might anticipate a case of dimensionality crossover. Phonons with wavelengths on the order of the dislocation spacing will resolve the individual dislocation cores, a case of linear defect scattering, which scatters into the 2D phonon density of states. Longer wavelength phonons would instead interact with the grid of dislocation cores as a planar mass contrast defect, which scatter into the frequency-independent 1D density of states. Once Equation 5.33 is squared when calculating the squared matrix element, we see that the matrix element term for this mass contrast defect characteristically contributes a factor of ω^2 to the scattering rate. After including the phase space terms, we would anticipate a $\tau^{-1} \propto \omega^3$ dependence at the short-wavelength, linear-defect scattering regime, and a $\tau^{-1} \propto \omega^2$ dependence at the long-wavelength, planar-defect scattering regime. Stacking faults are an interruption in stacking order than can occur when a dislocation

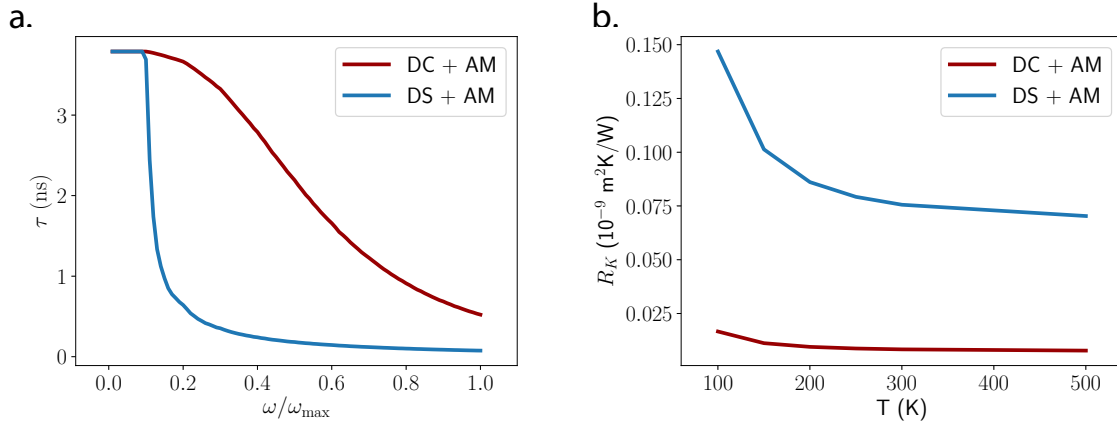


Figure 5.18. **Dislocation Core versus Strain Scattering Comparison** Comparison between the dislocation core and dislocation strain scattering effects in a 7° symmetric Si twist boundary. Phonon lifetimes (a) and Kapitza resistance (b) are compared between 1) a model including dislocation core and acoustic mismatch scattering (DC + AM) and 2) a model including dislocation strain and acoustic mismatch scattering (DS + AM). The strain scattering is shown to be the dominant effect at the interface, such that the contribution from dislocation core scattering can be ignored.

splits into two partial dislocations with a plane of atoms forming the stacking fault in between. It can similarly be discussed as a 2D mass imperfection, and is therefore expected to display $\tau^{-1} \propto \omega^2$ scattering behavior as with the plane of dislocation cores [24].

Figure 5.17b highlights the frequency dependence of the dislocation core array scattering. The acoustic mismatch effect is included, as this assures a finite scattering rate at $\omega = 0$. The transition is smooth from ω -independent acoustic mismatch scattering to $\tau \propto \omega^{-3}$ dislocation core scattering. However, there may be an intermediate region displaying the planar mass defect scattering signature of $\tau \propto \omega^{-2}$, although a clear transition frequency is not visible.

We can then compare the dislocation core to dislocation strain scattering to check whether the dislocation core plays a comparable role in the overall thermal resistance. The spectral relaxation times are compared in Figure 5.18a for a 7° twist boundary (with both instances including acoustic mismatch scattering), and the dislocation strain scattering is found to dominate over the full phonon frequency such that the Kapitza resistance is approximately $10\times$ higher for dislocation strain versus core scattering. Therefore, we confirm through this work that dislocation strain is the dominant scattering effect at grain boundaries and interfaces.

5.5.2. Phonon Drag at Mobile Dislocations

Finally, we have focused thus far on the lattice perturbation of a stationary dislocation array, resulting in a fully elastic scattering theory. However, dislocations additionally have dynamic degrees of freedom, allowing them to absorb and re-radiate phonons. Typically, this has been studied from the perspective of dislocation motion rather than thermal resistance, and the phonon dissipation effects are expected to impact dislocation glide through a viscous force, proportional to the dislocation velocity and a drag coefficient B [211]. These dissipative phonon processes are typically referred to as “phonon drag” and are further codified into two major categories: phonon wind [160, 211] and fluttering [212–214]. Phonon wind is similar to the anharmonic strain scattering discussed in detail in this chapter, however it accounts for the impact of the moving reference frame as dislocations glide. It has been shown the dislocation fluttering, or the localized oscillations along the dislocation line, plays a more significant role in inelastic phonon scattering [212].

The role of fluttering dislocation arrays in interfacial thermal resistance still remains an open question. However, analytic expressions have thus far quantified the effect in materials with “giant plasticity” such as solid He, where dislocations are expected to be incredibly mobile. In this case, unlike dislocation strain or core scattering, fluttering dislocation scattering is expected to be frequency-independent where all phonons in the spectrum transfer momentum between the vibrating dislocation lines. The scattering rate due to fluttering dislocations in a highly plastic material is reported in Amrit *et al.* as [215]:

$$(5.34) \quad \tau_{\text{fl}}^{-1} = \frac{(4.95 \times 10^7)b^2v_s^3}{D^2T^3}$$

Given the temperature dependence of the scattering rate, the low-temperature thermal conductivity signature for fluttering dislocation scattering would be $\kappa \propto T^6$. If we directly use the parameters for the 7° twist boundary used for comparison in the previous section, the scattering rate predicted by this equation is about an order of magnitude higher at room temperature when compared to our

model. These fluttering interactions may play a significant role in the interfacial thermal resistance, and realistic values based on the plasticity of the material should be used to quantify this effect.

5.6. Conclusions

To achieve device-level thermal modelling, scalable models, which contain the necessary physics to capture experimentally-observed trends in Kapitza resistance R_K , are required. We first review the scattering sources at an interface as well as the analytic and simulation-based approaches to evaluating Kapitza resistance. We then extend a previous model for scattering at a 1D array of edge dislocations (basic structure of a symmetric tilt grain boundary) to present a consistent method for modelling both symmetric tilt and twist grain boundaries as well as semicoherent heterointerfaces. The two main scattering contributions addressed in this model are: 1) the acoustic mismatch present at the interface, and 2) the periodic strain fields localized to the interface, which stem from the interfacial dislocation structure. This model allows for R_K comparisons between grain boundary type, energy, and structure. The main outcomes of this analysis are as follows:

- Previous analytic models describe either fully specular (AMM) or fully diffuse (DMM) scattering at an interface. The dislocation strain model lies in between these limits, the dislocation array can impart quantized momentum, and so we refer to this phenomenon as *diffractive scattering*. Diffraction peaks are visible in plots of the scattering rate.
- Phonon lifetimes for all three types of interfaces show a cross-over in frequency dependence, first reported on in Hanus *et al.* [181]. Low-frequency phonons show an ω -independent lifetime, indicative of planar defect scattering, while high-frequency phonons show a $\tau \propto \omega^{-1}$ dependence indicative of linear defect scattering.
- Kapitza resistance in the Si symmetric twist and tilt grain boundaries correlated closely with the Read-Shockley grain boundary energy. For a fixed grain boundary angle, Si twist boundaries were calculated to be about $1.3\times$ more resistive than Si tilt boundaries.
- The Kapitza resistance of the Si-Ge heterointerface was about an order of magnitude higher than that predicted for the Si grain boundaries. Additionally, our model showed a

close correspondence to atomistic simulation results, performing better than the AMM or DMM.

- Our Kapitza resistance model allows us to weight the relative contribution of acoustic mismatch and dislocation strain to the overall resistance at the interface. This distinction carries important implications in thermal engineering because the acoustic mismatch is fixed for a given interface, while the dislocation strain can be tailored through annealing, for example. Dislocation strain accounts for $\sim 95\%$ of the total R_K in symmetric tilt and twist grain boundaries, but only $\sim 50\%$ of the total R_K in semicoherent heterointerfaces.
- Dislocation core scattering is often viewed as negligible, since dislocation strain is expected to dominate for the majority of the frequency spectrum. We confirm this to be the case in our dislocation array scattering model. The dislocation core scattering may also show a frequency cross-over from $\tau \propto \omega^{-2}$ at low-frequency, a signature of a 2D mass contrast defect, to $\tau \propto \omega^{-3}$, a signature of a 1D mass contrast defect (the common description of individual dislocation core defects).

CHAPTER 6

Conclusions and Future Directions: Bridging Atomistic and Continuum Methods

The complexity of structure-property relations in thermoelectric materials is perhaps best highlighted in the Process-Structure-Property-Performance (PSPP) diagram shown in Figure 6.1 [216]. Notably, even this transport-focused PSPP diagram is simplified because it omits other pertinent information about thermoelectric performance such as mechanical properties like fracture toughness and creep resistance or the temperature range of peak performance, which should be tailored for a specific application. In an ideal integrated computational materials engineering approach, each linkage in the PSPP diagram can be explained by a physical model, and so it provides perspective on the role of this thesis work and the areas where progress is required. Chapters 3 and 4 of this thesis primarily describe the effects that dopant and alloying elements have on the carrier mobility and the lattice thermal conductivity. Moving forward, better analytic considerations for the deformation potential and alloy scattering potential are required for modelling carrier mobility data. While these quantities can be computed rigorously via first-principles, as a function of electron wavevector, these calculations are both expensive and difficult to interpret. Given the wealth of thermoelectric transport property data now housed in databases such as the StarryData2 [217], it may be possible to develop machine learning models to evaluate “transport relevant” deformation and alloy scattering potentials, which enter into the analytic expressions discussed in Chapter 4.

Chapter 5 discusses the influence on thermal transport of grain boundary structures as well as some nanoprecipitate interfaces, which can be described as semicoherent heterointerfaces. Specifically,

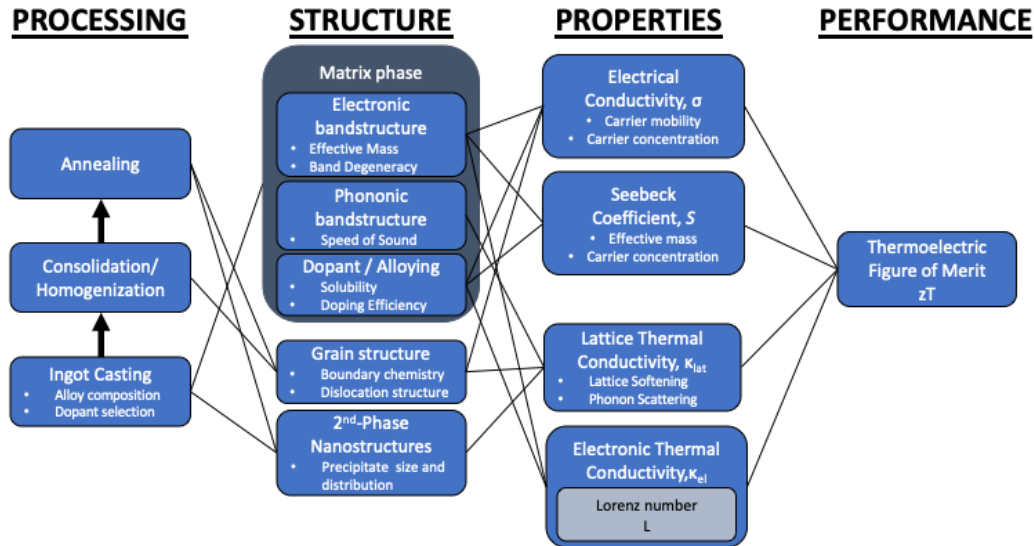


Figure 6.1. **Process-Structure-Properties-Performance Diagram for Thermoelectrics** Relationships between sample preparation, characteristics, properties, and performance are highlighted for bulk thermoelectric compounds. In an integrated computational materials engineering (ICME) approach, the linkages are described through analytic or simulation-based methods.

we highlight the role of interfacial dislocation strain on the thermal boundary resistance R_K of low-energy grain boundaries and interfaces. The interfacial dislocation strain scattering is shown to have a dominant effect, compared to the change in elastic medium at the interface, which is the effect treated by the standard acoustic mismatch model. More broadly, our approach to interface scattering provides a route to address spatially varying perturbations, which can be difficult to handle in atomistic simulations that are limited by small simulation sizes and periodic boundary conditions. The study of interface and dislocation-phonon scattering has perhaps the most room to grow, as current microstructure design for thermal materials tends to use highly simplified models. As a next step from this thesis work, the field may benefit from the development of semi-empirical models, which continue to treat defect strain fields using continuum elasticity theory, but use DFT-inputs to describe mode-dependent phonon properties, rather than the simplified Debye or Born von-Karman dispersion models.

Another useful next step would be to understand how these R_K trends with grain boundary dislocation structure and degree of coherency may impact the microstructure design of thermal

materials. For example, a recent work by Zhang and Minnich [218] has investigated the optimum size distribution of Ge precipitates in polycrystalline Si for full spectrum phonon scattering, assuming a fixed Ge volume fraction (a similar analysis is described in Mingo *et al.* [219]). In this analysis, however, information about the interface surrounding the precipitate phase is neglected. For the Si grain boundaries, the simple gray model relationship equating phonon mean-free-path to average grain size is used. The Ge precipitates are then treated with a simple model that interpolates between two regimes: short wavelength phonons exhibit a geometric scattering with a lifetime phonon dependence of $\tau(\omega) \propto \omega^0$, while long wavelength phonons with wavelengths on the order of the precipitate size undergo Rayleigh scattering with a phonon lifetime dependence of $\tau(\omega) \propto (\Delta\rho/\rho)^2\omega^4$. Here, $\Delta\rho$ is the density mismatch between the particle and matrix phase. The ideal particle distribution was determined to have discrete peaks at highly specific precipitate sizes instead of a broad, continuous distribution similar to the phonon spectrum.

Our work, however, suggests that microstructure optimization can be better informed by focusing on the interface around the precipitate. Connecting this back to the issue of precipitate size distribution, particle size not only influences the interface density, but also its coherency. Continuum elasticity theories and finite element method implementations show a critical radius of a nanoprecipitate required for the formation of misfit dislocation arrays [220]. In our work, these misfit dislocations are shown to be critical to scatter mid-frequency phonons with wavelengths on the order of the dislocation spacing. In the Si-Ge interface example, the misfit dislocation strain contributed about half of the interfacial thermal resistance. An additional variable to consider is the chemical composition near the interface, as solute segregation is shown to be two times greater at semicoherent versus coherent interfaces [221]. We anticipate that the consideration of interface structure will greatly impact nano- and microstructure design of thermal materials. We would expect an optimal microstructure for phonon scattering to maximize interface density while allowing for the formation of misfit dislocation loops. Another potentially important consideration is the relationship between misfit strain and phonon softening, or a reduction in elastic constants and phonon velocity. Phonon softening, in addition to scattering, is a route to achieve low lattice

thermal conductivity [222]. Therefore, in the context of thermal engineering, a trade-off may exist between misfit strain, which can promote phonon softening, and misfit dislocation formation, which can scatter mid-frequency phonons.

References

- [1] US energy use rises to highest level ever. <https://flowcharts.llnl.gov/>. Accessed on: 2020-04-10.
- [2] Meng Zhao, Wei Pan, Chunlei Wan, Zhixue Qu, Zheng Li, and Jun Yang. Defect engineering in development of low thermal conductivity materials: A review. Journal of the European Ceramic Society, 37(1):1–13, 2017.
- [3] Jayant Gopal Thakare, Chandan Pandey, M. M. Mahapatra, and R. S. Mulik. Thermal Barrier Coatings—A State of the Art Review. Metals and Materials International, 27(7):1947–1968, 2021.
- [4] Zhe Cheng, Fengwen Mu, Luke Yates, Tadatomo Suga, and Samuel Graham. Interfacial Thermal Conductance across Room-Temperature-Bonded GaN/Diamond Interfaces for GaN-on-Diamond Devices. ACS Applied Materials & Interfaces, 12(7):8376–8384, feb 2020.
- [5] Zhe Cheng, Fengwen Mu, Xiaoyang Ji, Tianguai You, Wenhui Xu, Tadatomo Suga, Xin Ou, David G Cahill, and Samuel Graham. Thermal Visualization of Buried Interfaces Enabled by Ratio Signal and Steady-State Heating of Time-Domain Thermoreflectance. ACS Applied Materials & Interfaces, 13(27):31843–31851, jul 2021.
- [6] Bo Sun, Georg Haunschild, Carlos Polanco, James (Zi Jian) Ju, Lucas Lindsay, Gregor Koblmüller, and Yee Kan Koh. Dislocation-induced thermal transport anisotropy in single-crystal group-III nitride films. Nature Materials, 18(2):136–140, 2019.
- [7] Robert Freer and Anthony V. Powell. Realising the potential of thermoelectric technology: A Roadmap. Journal of Materials Chemistry C, 8(2):441–463, 2020.
- [8] HVAC energy breakdown. energy.gov.au. Accessed on: 2020-04-10.
- [9] G. Jeffrey Snyder, Saniya LeBlanc, Doug Crane, Herschel Pangborn, Chris E. Forest, Alex Rattner, Leah Borgsmiller, and Shashank Priya. Distributed and localized cooling with thermoelectrics. Joule, 5(4):748–751, 2021.
- [10] Diana Enescu and Elena Otilia Virjoghe. A review on thermoelectric cooling parameters and performance. Renew. and Sus. Energy Rev., 38:903–916, 2014.

- [11] Fiscal Year (FY) 2022 Administration Research and Development Budget Priorities and Cross-cutting Actions. Technical report, Executive Office of the President (OMB, OSTP), 2020.
- [12] G Jeffrey Snyder and Eric S Toberer. Complex thermoelectric materials. Nature Materials, 7(February):105–114, 2008.
- [13] Ramya Gurunathan, Riley Hanus, and G. Jeffrey Snyder. Alloy scattering of phonons. Materials Horizons, 7, 2020.
- [14] Tyler J. Slade, Shashwat Anand, Max Wood, James P. Male, Kazuki Imasato, Dean Cheikh, Muath M. Al Malki, Matthias T. Agne, Kent J. Griffith, Sabah K. Bux, Chris Wolverton, Mercouri G. Kanatzidis, and G. Jeffrey Snyder. Charge-carrier-mediated lattice softening contributes to high zt in thermoelectric semiconductors. Joule, 5(5):1168–1182, 2021.
- [15] Alex Zevalkink, David M. Smiadak, Jeff L. Blackburn, Andrew J. Ferguson, Michael L. Chabinyo, Olivier Delaire, Jian Wang, Kirill Kovnir, Joshua Martin, Laura T. Schelhas, Taylor D. Sparks, Stephen D. Kang, Maxwell T. Dylla, G. Jeffrey Snyder, Brenden R. Ortiz, and Eric S. Toberer. A practical field guide to thermoelectrics: Fundamentals, synthesis, and characterization. Applied Physics Reviews, 5(2), 2018.
- [16] Andrew F May and G Jeffrey Snyder. Introduction to Modeling Thermoelectric Transport at High Temperatures. In Rowe D. M., editor, Thermoelectrics and its Energy Harvesting, volume 1, pages 1–20. CRC Press, 2011.
- [17] Zachary M Gibbs, Francesco Ricci, Guodong Li, Hong Zhu, Kristin Persson, Gerbrand Ceder, Geoffroy Hautier, Anubhav Jain, and G Jeffrey Snyder. Effective mass and Fermi surface complexity factor from ab initio band structure calculations. npj Computational Materials, 2017(Feb):1–6, 2017.
- [18] Junsoo Park, Maxwell Dylla, Yi Xia, Max Wood, G Jeffrey Snyder, and Anubhav Jain. When band convergence is not beneficial for thermoelectrics. Nature Communications, 12(1):3425, 2021.
- [19] Eric S Toberer, Alex Zevalkink, and G Jeffrey Snyder. Phonon engineering through crystal chemistry. Journal of Materials Chemistry, 21:15843–15852, 2011.
- [20] Ramya Gurunathan, Riley Hanus, Maxwell Dylla, Ankita Katre, and G. Jeffrey Snyder. Analytical models of phonon–point-defect scattering. Phys. Rev. Applied, 13:034011, Mar 2020.
- [21] Shashwat Anand, Ramya Gurunathan, Thomas Soldi, Leah Borgsmiller, Rachel Orenstein, and G. Jeffrey Snyder. Thermoelectric transport of semiconductor full-Heusler VFe₂Al. J. Mater. Chem. C, 8:10174–10184, 2020.

- [22] Riley Hanus, Ramya Gurunathan, Lucas Lindsay, Matthias T. Agne, Jingjing Shi, Samuel Graham, and G. Jeffrey Snyder. Thermal transport in defective and disordered materials. Applied Physics Reviews, 8(3):031311, 2021.
- [23] Ramya Gurunathan, Riley Hanus, Samuel Graham, Anupam Garg, and G. Jeffrey Snyder. Thermal resistance at a twist boundary and a semicoherent heterointerface. Physical Review B, 103(14):144302, apr 2021.
- [24] G.P. Srivastava. The Physics of Phonons. IOP Publishing, 1990.
- [25] Martin Dove. Introduction to Lattice Dynamics. Cambridge University Press, 1993.
- [26] Max Born and Kun Huang. Dynamical Theory of Crystal Lattices. MIT Press, 1964.
- [27] Jan W. Jaeken and Stefaan Cottenier. Solving the Christoffel equation: Phase and group velocities. Computer Physics Communications, 207:445–451, 2016.
- [28] Matthias T. Agne, Kazuki Imasato, Shashwat Anand, Kathleen Lee, Sabah K. Bux, Alex Zevalkink, Alexander J.E. Rettie, Duck Young Chung, Mercuri G. Kanatzidis, and G. Jeffrey Snyder. Heat capacity of Mg₃Sb₂, Mg₃Bi₂, and their alloys at high temperature. Materials Today Physics, 6:83–88, 2018.
- [29] J.M. Ziman. Electrons and Phonons. Clarendon Press, Oxford, 1960.
- [30] Gangjian Tan, Shiqiang Hao, Riley C. Hanus, Xiaomi Zhang, Shashwat Anand, Trevor P. Bailey, Alexander J.E. Rettie, Xianli Su, Ctirad Uher, Vinayak P. Dravid, G. Jeffrey Snyder, Chris Wolverton, and Mercuri G. Kanatzidis. High Thermoelectric Performance in SnTe-AgSbTe₂ Alloys from Lattice Softening, Giant Phonon-Vacancy Scattering, and Valence Band Convergence. ACS Energy Letters, 3:705–712, 2018.
- [31] David G. Cahill, S. K. Watson, and R. O. Pohl. Lower limit to the thermal conductivity of disordered crystals. Physical Review B, 46(10):6131–6140, 1992.
- [32] David R. Clarke. Materials selections guidelines for low thermal conductivity thermal barrier coatings. Surface and Coatings Technology, 163-164:67–74, 2003.
- [33] Matthias T. Agne, Riley Hanus, and G. Jeffrey Snyder. Minimum thermal conductivity in the context of diffuson-mediated thermal transport. Energy and Environmental Science, 11(3):609–616, 2018.
- [34] W. Ashcroft and David Mermin. Solid state physics. Brooks/Cole, 1976.
- [35] Matthias T. Agne, Peter W. Voorhees, and G. Jeffrey Snyder. Phase Transformation Contributions to Heat Capacity and Impact on Thermal Diffusivity, Thermal Conductivity, and Thermoelectric Performance. Advanced Materials, 31(35):1–7, 2019.

- [36] Olle Hellman and I. A. Abrikosov. Temperature-dependent effective third-order interatomic force constants from first principles. Phys. Rev. B, 88:144301, Oct 2013.
- [37] P. G. Klemens. Thermal Conductivity and Lattice Vibrational Modes. Solid State Physics - Advances in Research and Applications, 7(C):1–98, 1958.
- [38] Georgios Varnavides, Adam S. Jermyn, Polina Anikeeva, and Prineha Narang. Nonequilibrium phonon transport across nanoscale interfaces. Physical Review B, 100(11):115402, 2019.
- [39] Peter Carruthers. Scattering of Phonons by Elastic Strain Fields and the Thermal Resistance of Dislocations. Physical Review, 114(4):995–1001, 1959.
- [40] Yi Xia, Vinay I. Hegde, Koushik Pal, Xia Hua, Dale Gaines, Shane Patel, Jiangang He, Muratahan Aykol, and Chris Wolverton. High-throughput study of lattice thermal conductivity in binary rocksalt and zinc blende compounds including higher-order anharmonicity. Phys. Rev. X, 10:041029, Nov 2020.
- [41] Fei Tian, Bai Song, Xi Chen, Navaneetha K. Ravichandran, Yinchuan Lv, Ke Chen, Sean Sullivan, Jaehyun Kim, Yuanyuan Zhou, Te-Huan Liu, Miguel Goni, Zhiwei Ding, Jingying Sun, Geethal Amila Gamage Udalamatta Gamage, Haoran Sun, Hamidreza Ziyadee, Shuyuan Huyan, Liangzi Deng, Jianshi Zhou, Aaron J. Schmidt, Shuo Chen, Ching-Wu Chu, Pinshane Y. Huang, David Broido, Li Shi, Gang Chen, and Zhifeng Ren. Unusual high thermal conductivity in boron arsenide bulk crystals. Science, 361(6402):582–585, 2018.
- [42] Joon Sang Kang, Man Li, Huan Wu, Huuduy Nguyen, and Yongjie Hu. Experimental observation of high thermal conductivity in boron arsenide. Science, 361(6402):575–578, 2018.
- [43] Sheng Li, Qiye Zheng, Yinchuan Lv, Xiaoyuan Liu, Xiqu Wang, Pinshane Y. Huang, David G. Cahill, and Bing Lv. High thermal conductivity in cubic boron arsenide crystals. Science, 361(6402):579–581, 2018.
- [44] A. A. Maznev and O. B. Wright. Demystifying umklapp vs normal scattering in lattice thermal conductivity. American Journal of Physics, 82(11):1062–1066, 2014.
- [45] J. Callaway. Model for lattice Thermal Conductivity at Low Temperatures. Physical Review, 113(4):1046–1051, 1959.
- [46] G.P. Srivastava. Calculation of anharmonic. Pramana - Journal of Physics, 6(1):1–18, 1976.
- [47] Atsushi Togo and Isao Tanaka. First principles phonon calculations in materials science. Scripta Materialia, 108:1–5, 2015.
- [48] Charles Kittel and Herbert Kroemer. Thermal physics. W.H. Freeman and Company, 1998.

- [49] Philip B Allen, Joseph L Feldman, Jaroslav Fabian, and Frederick Wooten. Diffusons, locons and propagons: character of atomic vibrations in amorphous. Philosophical Magazine B, 79(11/12):1715–1732, 1999.
- [50] R. Peierls. Quantum Theory of Solids. Oxford University Press, 1955.
- [51] Wei Lv and Asegun S. Henry. Examining the validity of the phonon gas model in amorphous materials. Scientific reports, page (under review), 2016.
- [52] Freddy Deangelis, Murali Gopal Muraleedharan, Jaeyun Moon, Hamid Reza, Austin J Minnich, Alan J H Mcgaughey, and Asegun Henry. Thermal Transport in Disordered Materials. Nanoscale and Microscale Thermophysical Engineering, 00(00):1–36, 2018.
- [53] Robert J. Hardy. Energy-Flux Operator for a Lattice. Physical Review, 132(1):168–177, 1963.
- [54] Masoud H. Khadem and Aaron P. Wemhoff. Comparison of Green–Kubo and NEMD heat flux formulations for thermal conductivity prediction using the Tersoff potential. Computational Materials Science, 69:428–434, 2013.
- [55] Sridhar Sadasivam, Yuhang Che, Zhen Huang, Liang Chen, Satish Kumar, and T S Fisher. The Atomistic Green’s Function Method for Interfacial Phonon Transport. Annual Review of Heat Transfer, 17, 2014.
- [56] P G Klemens. The Scattering of Low-Frequency Lattice Waves by Static Imperfections. Proceedings of the Physical Society. Section A, 68:1113–1128, 1955.
- [57] P. Klemens. Thermal Resistance due to Point Defects at High Temperatures. Physical Review, 119(2):507–509, 1960.
- [58] H J Goldsmid. Recent Studies of Bismuth Telluride and Its Alloys. Journal of Applied Physics, 32:2198, 1961.
- [59] G P Meisner, D T Morelli, S Hu, J Yang, and C Uher. Structure and Lattice Thermal Conductivity of Fractionally Filled Skutterudites: Solid Solutions of Fully Filled and Unfilled End Members. Physical Review Letters, 80(16):3551–3554, 1998.
- [60] J Yang, G P Meisner, and L Chen. Strain field fluctuation effects on lattice thermal conductivity of ZrNiSn-based thermoelectric compounds. Applied Physics Letters, 85(7):1140, 2004.
- [61] Max Wood, Umut Aydemir, Saneyuki Ohno, and G. Jeffrey Snyder. Observation of valence band crossing: The thermoelectric properties of CaZn_2Sb_2 - CaMg_2Sb_2 solid solution. Journal of Materials Chemistry A, 6(20):9437–9444, 2018.

- [62] Eric S Toberer, Andrew F. May, Brent C. Melot, Espen Flage-Larsen, and G. Jeffrey Snyder. Electronic structure and transport in thermoelectric compounds AZn_2Sb_2 ($A = Sr, Ca, Yb, Eu$). Dalton Transactions, 39(4):1046–1054, 2010.
- [63] Ankita Katre, Jesús Carrete, and Natalio Mingo. Unraveling the dominant phonon scattering mechanism in the thermoelectric compound in ZrNiSn. Journal of Materials Chemistry A, 4:15940–15944, 2016.
- [64] Ankita Katre, Jesús Carrete, Tao Wang, Georg K H Madsen, and Natalio Mingo. Phonon transport unveils the prevalent point defects in GaN. Physical Review Materials, 2:050602, 2018.
- [65] Wu Li, L. Lindsay, D. A. Broido, Derek A. Stewart, and Natalio Mingo. Thermal conductivity of bulk and nanowire $Mg_2Si_xSn_{1-x}$ alloys from first principles. Physical Review B - Condensed Matter and Materials Physics, 86(17):174307, 2012.
- [66] Ankita Katre, Jesús Carrete, Bonny Dongre, Georg K. H. Madsen, and Natalio Mingo. Exceptionally Strong Phonon Scattering by B Substitution in Cubic SiC. Physical Review Letters, 119(7):075902, 2017.
- [67] Carlos A. Polanco and Lucas Lindsay. Thermal conductivity of InN with point defects from first principles. Physical Review B, 98(1):014306, 2018.
- [68] Natalio Mingo, K. Esfarjani, D. A. Broido, and D. A. Stewart. Cluster scattering effects on phonon conduction in graphene. Physical Review B - Condensed Matter and Materials Physics, 81(4):045408, 2010.
- [69] Matthias Schrade and Terje G. Finstad. Using the Callaway Model to Deduce Relevant Phonon Scattering Processes: The Importance of Phonon Dispersion. Physica Status Solidi (B), 1800208:1–6, 2018.
- [70] Takuma Shiga, Takuma Hori, and Junichiro Shiomi. Influence of mass contrast in alloy phonon scattering. Japanese Journal of Applied Physics, 53:021802, 2014.
- [71] Tianli Feng, Bo Qiu, and Xiulin Ruan. Coupling between phonon-phonon and phonon-impurity scattering: A critical revisit of the spectral Matthiessen’s rule. Physical Review B - Condensed Matter and Materials Physics, 92(23):235206, 2015.
- [72] Shin-ichiro Tamura. Isotope scattering of dispersive phonons in Ge. Physical Review B, 27(2):858–866, 1983.
- [73] V.K. Zaitsev, E.N. Tkalenko, and E.N. Nikitin. Lattice thermal conductivity of Mg_2Si - Mg_2Sn , Mg_2Ge - Mg_2Sn , and Mg_2Si - Mg_2Ge solid solution. Sov. Phys. Solid State, 11(221), 1969.

- [74] Hasbuna Kamila, Prashant Sahu, Aryan Sankhla, Mohammad Yasseri, Hoang-ngan Pham, Titas Dasgupta, Eckhard Mueller, and Johannes de Boor. Analyzing transport properties of p-type $\text{Mg}_2\text{Si}-\text{Mg}_2\text{Sn}$ solid solutions: optimization of thermoelectric performance and insight into the electronic band structure. Journal of Materials Chemistry A, 7:1045–1054, 2019.
- [75] R Berman, E.L. Foster, and J.M. Ziman. The thermal conductivity of dielectric crystals: the effect of isotopes. Royal Society, page 344, 1956.
- [76] Glen A Slack. Thermal Conductivity of MgO , Al_2O_3 , $\text{Mg Al}_2\text{O}_4$, and Fe_3O_4 Crystals from 3° to 300°K . Physical Review, 126(2), 1962.
- [77] Shin-ichiro Tamura. Isotope Scattering of large wave-vector phonons in GaS and InSb: Deformation dipole and overlap-shell models. Physical Review B, 30(2):849–854, 1984.
- [78] R Berman. Thermal Conduction in Solids. Clarendon Press, Oxford, 1976.
- [79] Benedikt Klobes, Johannes de Boor, Ahmet Alatas, Michael Y Hu, Ronnie E Simon, and Raphaël P Hermann. Lattice dynamics and elasticity in thermoelectric $\text{Mg}_2\text{Si}_{1-x}\text{Sn}_x$. Physical Review Materials, 3(2):025404, 2019.
- [80] Patrick E Hopkins. Dispersion considerations affecting phonon-mass impurity scattering rates. AIP Advances, 1:041705, 2011.
- [81] Jason M Larkin and Alan J H Mcgaughey. Predicting alloy vibrational mode properties using lattice dynamics calculations, molecular dynamics simulations, and the virtual crystal approximation. Journal of Applied Physics, 114:023507, 2017.
- [82] Jesús Carrete, Bjorn Vermeersch, Ankita Katre, Ambroise van Roekeghem, Tao Wang, Georg K.H. Madsen, and Natalio Mingo. almaBTE: A solver of the space-time dependent Boltzmann transport equation for phonons in structured materials. Computer Physics Communications, 220:351–362, 2019.
- [83] Wu Li, Jesús Carrete, Nebil A. Katcho, and Natalio Mingo. ShengBTE: A solver of the Boltzmann transport equation for phonons. Computer Physics Communications, 185:1747–1758, 2014.
- [84] Hamid Reza Seyf, Luke Yates, Thomas L Bougher, Samuel Graham, Baratunde A Cola, Theeradetch Detchprohm, Mi-hee Ji, Jeomoh Kim, Russell Dupuis, Wei Lv, and Asegun Henry. Rethinking phonons: The issue of disorder. npj Computational Materials, 49(April), 2017.
- [85] Ankita Katre, Atsushi Togo, Isao Tanaka, and Georg K.H. Madsen. First principles study of thermal conductivity cross-over in nanostructured zinc-chalcogenides. Journal of Applied Physics, 117:045102, 2015.

- [86] Zhiting Tian, Jivtesh Garg, Keivan Esfarjani, Takuma Shiga, Junichiro Shiomi, and Gang Chen. Phonon conduction in PbSe, PbTe, and $\text{PbTe}_{1-x}\text{Se}_x$ from first-principles calculations. Physical Review B - Condensed Matter and Materials Physics, 85:184303, 2012.
- [87] Yanfei Wang, Fan Yang, and Ping Xiao. Rattlers or oxygen vacancies: Determinant of high temperature plateau thermal conductivity in doped pyrochlores. Applied Physics Letters, 102(14):1–6, 2013.
- [88] Yang Wang, Fang Li, Luxiang Xu, Yu Sui, Xianjie Wang, Wenhui Su, and Xiaoyang Liu. Large Thermal Conductivity Reduction Induced by La/O Vacancies in the Thermoelectric LaCoO_3 System. Inorganic Chemistry, 50(10):4412–4416, 2011.
- [89] Yanzhong Pei and Donald T Morelli. Vacancy phonon scattering in thermoelectric In_2Te_3 - InSb solid solutions. Applied Physics Letters, 94(2009):122112, 2009.
- [90] Gangjian Tan, Wolfgang G Zeier, Fengyuan Shi, Pengli Wang, G Je, Vinayak P Dravid, and Mercouri G Kanatzidis. High Thermoelectric Performance $\text{SnTe-In}_2\text{Te}_3$ Solid Solutions Enabled by Resonant Levels and Strong Vacancy Phonon Scattering. Chemistry of Materials, 27:7801–7811, 2015.
- [91] Jiawen Shen, Xinyue Zhang, Siqi Lin, Juan Li, Zhiwei Chen, Wen Li, and Yanzhong Pei. Vacancy scattering for enhancing the thermoelectric performance of CuGaTe_2 solid solutions. Journal of Materials Chemistry A, 4(40):15464–15470, 2016.
- [92] Felix Böcher, Sean P. Culver, Jan Peilstöcker, Kai S. Weldert, and Wolfgang G. Zeier. Vacancy and anti-site disorder scattering in AgBiSe_2 thermoelectrics. Dalton Transactions, 46(12):3906–3914, 2017.
- [93] Zhixue Qu, Taylor D. Sparks, Wei Pan, and David R. Clarke. Thermal conductivity of the gadolinium calcium silicate apatites: Effect of different point defect types. Acta Materialia, 59(10):3841–3850, 2011.
- [94] C. A. Ratsifaritana and P. G. Klemens. Scattering of phonons by vacancies. International Journal of Thermophysics, 8(6):737–750, 1987.
- [95] Paul G Klemens. Phonon scattering by oxygen vacancies in ceramics. Physica B, 264:263–265, 1999.
- [96] Yanzhong Pei, Linglang Zheng, Wen Li, Siqi Lin, Zhiwei Chen, Yanying Wang, Xiangfu Xu, Hulei Yu, Yue Chen, and Binghui Ge. Interstitial Point Defect Scattering Contributing to High Thermoelectric Performance in SnTe . Advanced Electronic Materials, 2(6):1600019, 2016.
- [97] Junjie Yu, Chenguang Fu, Yintu Liu, Kaiyang Xia, Umut Aydemir, Thomas C. Chasapis, G. Jeffrey Snyder, Xinbing Zhao, and Tiejun Zhu. Unique role of refractory ta alloying in

- enhancing the figure of merit of nbfesb thermoelectric materials. Advanced Energy Materials, 8(1):1701313, 2018.
- [98] Chenguang Fu, Yintu Liu, Xinbing Zhao, and Tiejun Zhu. Are solid solutions better in fensb-based thermoelectrics? Advanced Electronic Materials, 2(12):1600394, 2016.
- [99] Hangtian Zhu, Jun Mao, Yuwei Li, Jifeng Sun, Yumei Wang, Qing Zhu, Guannan Li, Qichen Song, Jiawei Zhou, Yuhao Fu, Ran He, Tian Tong, Zihang Liu, Wuyang Ren, Li You, Zhiming Wang, Jun Luo, Andrei Sotnikov, Jiming Bao, Kornelius Nielsch, Gang Chen, David J Singh, and Zhifeng Ren. Discovery of TaFeSb-based half-Heuslers with high thermoelectric performance. Nature Communications, 10(1):270, 2019.
- [100] Hideaki Kato, Masaaki Kato, Yoichi Nishino, Uichiro Mizutani, and Shigeru Asano. Effect of silicon substitution on thermoelectric properties of Heusler-type Fe_2VAl alloy. Journal of Japanese Institute of Metals, 65(7):652–656, 2001.
- [101] Y Nishino, S Deguchi, and U Mizutani. Thermal and transport properties of the Heusler-type $\text{Fe}_2\text{VAl}_{1-x}\text{Ge}_x$ ($0 \leq x \leq 0.20$) alloys: Effect of doping on lattice thermal conductivity, electrical resistivity, and Seebeck coefficient. Physical Review B, 74:115115, 2006.
- [102] Krystel Renard, Arinori Mori, Yuichiro Yamada, Suguru Tanaka, Hidetoshi Miyazaki, and Yoichi Nishino. Thermoelectric properties of the Heusler-type $\text{Fe}_2\text{VTa}_x\text{Al}_{1-x}$ alloys. Journal of Applied Physics, 115:033707, 2014.
- [103] Fuminori Kobayashi, Naoki Ide, and Yoichi Nishino. Effects of Re Substitution on Thermoelectric Properties of Pseudogap System Fe_2VAl . Journal of Japanese Institute of Metals, 71(2):208–212, 2007.
- [104] Wenjia Lu, Wenqing Zhang, and Lidong Chen. Thermoelectric properties of $(\text{Fe}_{1-x}\text{Co}_x)_2\text{VAl}$ Heusler-type compounds. Journal of Alloys and Compounds, 484(1-2):812–815, 2009.
- [105] Riley Hanus, Janine George, Max Wood, Alexander Bonkowski, Yongqiang Cheng, Douglas L. Abernathy, Michael E. Manley, Geoffroy Hautier, G. Jeffrey Snyder, and Raphaël P. Hermann. Uncovering design principles for amorphous-like heat conduction using two-channel lattice dynamics. Materials Today Physics, 18:100344, 2021.
- [106] S. Joseph Poon and Jian He. Multi-Principal-Element Approach to High-Performance Thermoelectric Materials. arXiv, pages 1–17, 2019.
- [107] Ruiheng Liu, Hongyi Chen, Kumpeng Zhao, Yuting Qin, Binbin Jiang, Tiansong Zhang, Gang Sha, Xun Shi, Ctirad Uher, Wenqing Zhang, and Lidong Chen. Entropy as a Gene-Like Performance Indicator Promoting Thermoelectric Materials. Advanced Materials, 29(38):1–7, 2017.

- [108] Michael C. Gao, Daniel B. Miracle, David Maurice, Xuehui Yan, Yong Zhang, and Jeffrey A. Hawk. High-entropy functional materials. Journal of Materials Research, 33(19):3138–3155, 2018.
- [109] John Androulakis, Chia Her Lin, Hun Jin Kong, Ctirad Uher, Chun I. Wu, Timothy Hogan, Bruce A. Cook, Thierry Caillat, Konstantinos M. Paraskevopoulos, and Mercouri G. Kanatzidis. Spinodal decomposition and nucleation and growth as a means to bulk nanostructured thermoelectrics: Enhanced performance in $\text{Pb}_{1-x}\text{Sn}_x\text{Te-PbS}$. Journal of the American Chemical Society, 129(31):9780–9788, 2007.
- [110] Y. Xia, S. Bhattacharya, V. Ponnambalam, A. L. Pope, S. J. Poon, and T. M. Tritt. Thermoelectric properties of semimetallic (Zr, Hf)CoSb half-Heusler phases. Journal of Applied Physics, 88(4):1952–1955, 2000.
- [111] Brenden R. Ortiz, Jesse M. Adamczyk, Kiarash Gordiz, Tara Braden, and Eric S. Toberer. Towards the high-throughput synthesis of bulk materials: Thermoelectric $\text{PbTe-PbSe-SnTe-SnSe}$ alloys. Molecular Systems Design and Engineering, 4(2):407–420, 2019.
- [112] G. Jeffrey Snyder, Alemayouh H. Snyder, Maxwell Wood, Ramya Gurunathan, Berhanu H. Snyder, and Changning Niu. Weighted Mobility. Advanced Materials, 32(25):1–5, 2020.
- [113] J. Bardeen and W. Shockley. Deformation potentials and mobilities in non-polar crystals. Physical Review, 80(1):72–80, 1950.
- [114] J.M. Ziman. Models of Disorder. Alden Press, Oxford, 1979.
- [115] F. Murphy-Armando and S. Fahy. First-principles calculation of alloy scattering in $\text{Ge}_x\text{Si}_{1-x}$. Physical Review Letters, 97(9):1–4, 2006.
- [116] L. Makowski and M. Glicksman. Disorder scattering in solid solutions of III-V semiconducting compounds. Journal of Physics and Chemistry of Solids, 34(3):487–492, 1973.
- [117] J.W. Harrison and J.R. Hauser. Alloy scattering in ternary III-V compounds. Physical Review B, 17(2):912–913, 1978.
- [118] Wang Heng, Ramya Gurunathan, Chenguang Fu, and G. Jeffrey Snyder. Thermoelectric transport modeling beyond single parabolic band and acoustic phonon scattering. Materials Advances, 2021. in preparation.
- [119] Saumitra R. Mehrotra, Abhijeet Paul, and Gerhard Klimeck. Atomistic approach to alloy scattering in $\text{Si}_{1-x}\text{Ge}_x$. Applied Physics Letters, 98(17):98–101, 2011.
- [120] Mats Hillert. Empirical methods of predicting and representing thermodynamic properties of ternary solution phases. Calphad, 4(1):1–12, 1980.

- [121] J. Ganguly. Thermodynamic modelling of solid solutions. In C.A. Geiger, editor, EMU Notes in Mineralogy, pages 37–69. Mineralogical Society of Great Britain, 2001.
- [122] Mats Hillert. Phase Equilibria, Phase Diagrams and Phase Transformations. Cambridge University Press, 2008.
- [123] Simen N.H. Eliassen, Ankita Katre, Georg K.H. Madsen, Clas Persson, Ole Martin Løvvik, and Kristian Berland. Lattice thermal conductivity of $\text{TixZryHf}_{1-x-y}\text{NiSn}$ half-Heusler alloys calculated from first principles: Key role of nature of phonon modes. Physical Review B, 95(4):1–9, 2017.
- [124] Matthias Schrade, Kristian Berland, Simen N H Eliassen, Matylda N Guzik, Cristina Echevarria-Bonet, Magnus H Sørby, Petra Jenuš, Bjørn C Hauback, Raluca Tofan, Anette E Gunnæs, Clas Persson, Ole M Løvvik, and Terje G Finstad. The role of grain boundary scattering in reducing the thermal conductivity of polycrystalline XNiSn ($\text{X}=\text{Hf}, \text{Zr}, \text{Ti}$) half-Heusler alloys. Scientific Reports, 7(1):13760, 2017.
- [125] M. Caro, L. K. Béland, G. D. Samolyuk, R. E. Stoller, and A. Caro. Lattice thermal conductivity of multi-component alloys. Journal of Alloys and Compounds, 648:408–413, 2015.
- [126] Yong Zhang, Yun Jun Zhou, Jun Pin Lin, Guo Liang Chen, and Peter K. Liaw. Solid-solution phase formation rules for multi-component alloys. Advanced Engineering Materials, 10(6):534–538, 2008.
- [127] Indika U Arachchige and Mercuri G Kanatzidis. Anomalous Band Gap Evolution from Band Inversion in $\text{Pb}_{1-x}\text{Sn}_x\text{Te}$ Nanocrystals. Nano Letters, 9(4):1583–1587, apr 2009.
- [128] James P. Male, Riley Hanus, G. Jeffrey Snyder, and Raphaël P. Hermann. Thermal Evolution of Internal Strain in Doped PbTe . Chemistry of Materials, 33(12):4765–4772, 2021.
- [129] Yixuan Wu, Zhiwei Chen, Pengfei Nan, Fen Xiong, Siqi Lin, Xinyue Zhang, Yue Chen, Lidong Chen, Binghui Ge, and Yanzhong Pei. Lattice Strain Advances Thermoelectrics. Joule, 3(5):1276–1288, 2019.
- [130] Hyun Sik Kim, Stephen D Kang, Yinglu Tang, Riley Hanus, and G Jeffrey Snyder. Dislocation strain as the mechanism of phonon scattering at grain boundaries. Materials Horizons, 3:234–240, 2016.
- [131] Yuan Yu, Siyuan Zhang, Antonio Massimiliano Mio, Baptiste Gault, Ariel Sheskin, Christina Scheu, Dierk Raabe, Fangqiu Zu, Matthias Wuttig, Yaron Amoyal, and Oana Cojocaru-Mirédin. Ag-Segregation to Dislocations in PbTe -Based Thermoelectric Materials. ACS Applied Materials and Interfaces, 10(4):3609–3615, 2018.

- [132] Oshrat Appel, Tsvika Zilber, Sergey Kalabukhov, Ofer Beeri, and Yaniv Gelbstein. Morphological effects on the thermoelectric properties of $\text{Ti}_{0.3}\text{Zr}_{0.35}\text{Hf}_{0.35}\text{Ni}_{1+\delta}\text{Sn}$ alloys following phase separation. *Journal of Materials Chemistry C*, 3(44):11653–11659, 2015.
- [133] Michael Schwall and Benjamin Balke. Phase separation as a key to a thermoelectric high efficiency. *Physical Chemistry Chemical Physics*, 15(6):1868–1872, 2013.
- [134] Jun Luo, Li You, Jiye Zhang, Kai Guo, Hangtian Zhu, Lin Gu, Zhenzhong Yang, Xin Li, Jiong Yang, and Wenqing Zhang. Enhanced Average Thermoelectric Figure of Merit of the PbTe-SrTe-MnTe Alloy. *ACS Applied Materials and Interfaces*, 9(10):8729–8736, 2017.
- [135] C.E. Rasmussen and C.K.I. Williams. *Gaussian Processes for Machine Learning*. 2006.
- [136] Marcus Noack and USDOE. gpcam v6, 1 2021.
- [137] Sung Wng Kim, Yoshisato Kimura, and Yoshinao Mishima. High temperature thermoelectric properties of TiNiSn-based half-Heusler compounds. *Intermetallics*, 15(3):349–356, 2007.
- [138] Srikant Kumar Mohanty, Yu-Yan Chen, Ping-Hung Yeh, and Ray-Hua Horng. Thermal Management of GaN-on-Si High Electron Mobility Transistor by Copper Filled Micro-Trench Structure. *Scientific Reports*, 9(1):19691, 2019.
- [139] Sang Il Kim, Hyeon A Mun, Hyun Sik Kim, Sung Woo Hwang, Jong Wook Roh, Dae Jin Yang, Weon Ho Shin, Xiang Shu Li, Young Hee Lee, G Jeffrey Snyder, and Sung Wng Kim. Dense dislocation arrays embedded in grain boundaries for high-performance bulk thermoelectrics. *Science*, 348(6230):109–115, 2015.
- [140] Haijun Wu, Jesús Carrete, Zhiyun Zhang, Yongquan Qu, Xuetao Shen, Zhao Wang, Li-Dong Zhao, and Jiaqing He. Strong enhancement of phonon scattering through nanoscale grains in lead sulfide thermoelectrics. *NPG Asia Materials*, 6(6):e108–e108, 2014.
- [141] Xianfu Meng, Zihang Liu, Bo Cui, Dandan Qin, Huiyuan Geng, Wei Cai, Liangwei Fu, Jiaqing He, Zhifeng Ren, and Jiehe Sui. Grain boundary engineering for achieving high thermoelectric performance in n-type skutterudites. *Advanced Energy Materials*, 7(13):1602582, 2017.
- [142] Rolf Landauer. Spatial variation of currents and fields due to localized scatterers in metallic conduction. *IBM Journal of Research and Development*, 44(1):251–259, 1957.
- [143] Christian Monachon, Ludger Weber, and Chris Dames. Thermal Boundary Conductance : A Materials Science Perspective. *Annual Reviews of Materials Research*, 46:433–463, 2016.
- [144] Gang Chen. Thermal conductivity and ballistic-phonon transport in the cross-plane direction of superlattices. *Physical Review B*, 57(23):14958, 1998.

- [145] Z. Chen, Z. Wei, Y. Chen, and C. Dames. Anisotropic Debye model for the thermal boundary conductance. Physical Review B, 87(12):125426, 2013.
- [146] C. Dames and G. Chen. Theoretical phonon thermal conductivity of Si/Ge superlattice nanowires. Journal of Applied Physics, 95(2):682–693, 2004.
- [147] Lucas Lindsay. First principles peierls-boltzmann phonon thermal transport: A topical review. Nanoscale and Microscale Thermophysical Engineering, 20(2):67–84, 2016.
- [148] Amelia Carloina Sparavigna. The boltzmann equation of phonon thermal transport solved in the relaxation time approximation - i - theory, mechanics. Materials Science & Engineering Journal, 3:34–45, 2016.
- [149] E. T. Swartz and R. O. Pohl. Thermal boundary resistance. Review of Modern Physics, 61(3):605–668, 1989.
- [150] R. S. Prasher and P. E. Phelan. A scattering-mediated acoustic mismatch model for the prediction of thermal boundary resistance. Journal of Heat Transfer, 123(1):105–112, 2001.
- [151] Yandong Sun, Yanguang Zhou, Ming Hu, G. Jeffrey Snyder, Ben Xu, and Wei Liu. Probing the phonon mean free paths in dislocation core by molecular dynamics simulation. Journal of Applied Physics, 129(5):055103, 2021.
- [152] Yandong Sun, Yanguang Zhou, Ramya Gurunathan, Jin-Yu Zhang, Ming Hu, Wei Liu, Ben Xu, and G. Jeffrey Snyder. Phonon scattering in the complex strain field of a dislocation, 2021.
- [153] Songting Cai, Xiaobing Hu, Mercuri Kanatzidis, and Vinayak Dravid. Novel core-shell nanoscale precipitates in high performance pbse-cdse thermoelectric materials. Microscopy and Microanalysis, 26(S2):34–36, 2020.
- [154] Sien Wang, Dongchao Xu, Ramya Gurunathan, G. Jeffrey Snyder, and Qing Hao. Thermal studies of individual Si/Ge heterojunctions — The influence of the alloy layer on the heterojunction. Journal of Materiomics, 6(2):248–255, 2020.
- [155] Yingying Zhang, Dengke Ma, Yi Zang, Xiaojia Wang, and Nuo Yang. A modified theoretical model to accurately account for interfacial roughness in predicting the interfacial thermal conductance. Frontiers in Energy Research, 6(48):1–6, 2018.
- [156] Thomas Beechem, Samuel Graham, Patrick Hopkins, and Pamela Norris. Role of interface disorder on thermal boundary conductance using a virtual crystal approach. Applied Physics Letters, 90(5), 2007.
- [157] Kiarash Gordiz and Asegun Henry. Phonon transport at crystalline Si/Ge interfaces: The role of interfacial modes of vibration. Scientific Reports, 6(October 2015):1–9, 2016.

- [158] Ashutosh Giri and Patrick E. Hopkins. Role of interfacial mode coupling of optical phonons on thermal boundary conductance. Scientific Reports, 7(1):1–11, 2017.
- [159] Daniel N. Blaschke, Emil Mottola, and Dean L. Preston. Dislocation drag from phonon wind in an isotropic crystal at large velocities. Philosophical Magazine, 100(5):571–600, 2020.
- [160] A. M’Ndange-Pfupfu and L. D. Marks. Modeling of phonon wind shielding effects on moving dislocation arrays. Tribology Letters, 47(3):431–434, 2012.
- [161] Daisuke Aketo, Takuma Shiga, and Junichiro Shiomi. Scaling laws of cumulative thermal conductivity for short and long phonon mean free paths. Applied Physics Letters, 105(13), 2014.
- [162] Jesús Carrete, Bjorn Vermeersch, Ankita Katre, Ambroise van Roekeghem, Tao Wang, Georg K.H. Madsen, and Natalio Mingo. almaBTE: A solver of the space-time dependent Boltzmann transport equation for phonons in structured materials. Computer Physics Communications, 220:351–362, 2017.
- [163] Ting Han Chou, Lucas Lindsay, Alexei A. Maznev, Jateen S. Gandhi, Donna W. Stokes, Rebecca L. Forrest, Abdelhak Bensaoula, Keith A. Nelson, and Chi Kuang Sun. Long mean free paths of roomtemperature THz acoustic phonons in a high thermal conductivity material. Physical Review B, 100(9):1–9, 2019.
- [164] Tzu-Ming Liu, Shih-Ze Sun, Chieh-Feng Chang, Chang-Chi Pan, Guan-Ting Chen, Jen-Inn Chyi, Vitalyi Gusev, and Chi-Kuang Sun. Anharmonic decay of subterahertz coherent acoustic phonons in gan. Applied Physics Letters, 90(4):041902, 2007.
- [165] Jivtesh Garg, Tengfei Luo, and Gang Chen. Spectral concentration of thermal conductivity in GaN - A first-principles study. Applied Physics Letters, 112(25), 2018.
- [166] Atsushi Togo, Laurent Chaput, and Isao Tanaka. Distributions of phonon lifetimes in Brillouin zones. Physical Review B, 91:094306, 2015.
- [167] M. Y. Toriyama, A. M. Ganose, M. Dylla, S. Anand, J. Park, M. K. Brod, J. Munro, K. A. Persson, A. Jain, and G. J. Snyder. Comparison of the tetrahedron method to smearing methods for the electronic density of states, 2021.
- [168] Giuseppe Romano. Openbte: a solver forab-initio phonon transport in multidimensional structures. arXiv preprint arXiv:2106.02764, 2021.
- [169] Ravi Prasher. Acoustic mismatch model for thermal contact resistance of van der Waals contacts. Applied Physics Letters, 94(041905), 2014.
- [170] James Hickman and Yuri Mishin. Thermal conductivity and its relation to atomic structure for symmetrical tilt grain boundaries in silicon. Physical Review Materials, 4(3):033405, 2020.

- [171] P. K. Schelling, S. R. Phillpot, and P. Keblinski. Kapitza conductance and phonon scattering at grain boundaries by simulation. Journal of Applied Physics, 95:6082–6091, 2004.
- [172] A. Maiti, G. D. Mahan, and S. T. Pantelides. Dynamical simulations of nonequilibrium processes - Heat flow and the Kapitza resistance across grain boundaries. Solid State Communications, 102(7):517–521, 1997.
- [173] Kiarash Gordiz and Asegun Henry. A formalism for calculating the modal contributions to thermal interface conductance. New Journal of Physics, 17(10), 2015.
- [174] Kiarash Gordiz and Asegun Henry. Phonon transport at interfaces: Determining the correct modes of vibration. Journal of Applied Physics, 119(1), 2016.
- [175] Kiarash Gordiz and Asegun Henry. Phonon transport at crystalline Si/Ge interfaces: The role of interfacial modes of vibration. Scientific Reports, 6(October 2015):1–9, 2016.
- [176] W. Zhang, T. S. Fisher, and N. Mingo. Simulation of Interfacial Phonon Transport in Si–Ge Heterostructures Using an Atomistic Green’s Function. Journal of Heat Transfer, 129(April):483–491, 2007.
- [177] Jinghang Dai and Zhiting Tian. Rigorous formalism of anharmonic atomistic Green’s function for three-dimensional interfaces. Physical Review B, 101(4):41301, 2020.
- [178] Yangyu Guo, Zhongwei Zhang, Marc Bescond, Shiyun Xiong, Masahiro Nomura, and Sebastian Volz. Anharmonic phonon-phonon scattering at the interface between two solids by nonequilibrium green’s function formalism. Phys. Rev. B, 103:174306, May 2021.
- [179] Read W. T. and Shockley W. Dislocation Models of Crystal Grain Boundaries. Physical Review, 78(3):275 – 289, 1950.
- [180] Wei Cai and William Nix. Imperfections in Crystalline Solids. Cambridge University Press, 2016.
- [181] Riley Hanus, Anupam Garg, and G Jeffrey Snyder. Phonon diffraction and dimensionality crossover in phonon-interface scattering. Communications Physics, 1:78, 2018.
- [182] D Xu, R Hanus, Y Xiao, S Wang, G J Snyder, and Q Hao. Thermal boundary resistance correlated with strain energy in individual Si film-wafer twist boundaries. Materials Today Physics, 6:53–59, 2018.
- [183] Kaiping Tai, Abigail Lawrence, Martin P. Harmer, and Shen J. Dillon. Misorientation dependence of Al₂O₃ grain boundary thermal resistance. Applied Physics Letters, 102(3):1–5, 2013.

- [184] Mercuri G. Kanatzidis. Nanostructured thermoelectrics: The new paradigm? Chemistry of Materials, 22(3):648–659, 2010.
- [185] Yoon-jun Kim, Li-dong Zhao, Mercuri G Kanatzidis, and David N Seidman. Analysis of Nanoprecipitates in a Na-Doped PbTe-SrTe Thermoelectric Material with a High Figure of Merit. Applied Materials and Interfaces, 9:21791 – 21797, 2017.
- [186] Gunter Gottstein. Grain Boundary Migration in Metals: Thermodynamics, Kinetics, Applications. CRC Press, 2nd edition, 2009.
- [187] J. H. Van Der Merwe. On the stresses and energies associated with inter-crystalline boundaries. Proceedings of the Physical Society. Section A, 63(6):616–637, 1950.
- [188] P. Carruthers. Theory of thermal conductivity of solids at low temperatures. Reviews of Modern Physics, 33(1):92–138, 1961.
- [189] M. Omini and A. Sparavigna. Role of grain boundaries as phonon diffraction gratings in the theory of thermal conductivity. Physical Review B, 61:6677–6688, 2000.
- [190] John Price Hirth and Jens Lothe. Theory of Dislocations. Wiley, New York, 2nd edition, 1982.
- [191] Yugui Yao, Tsuchiang Wang, and Chongyu Wang. Peierls-Nabarro model of interfacial misfit dislocation: An analytic solution. Physical Review B, 59(12):8232–8236, 1999.
- [192] R.A. Brown. The scattering of phonons by the strain and rotation fields of crystal defects. Journal of Physics C, 16:1009, 1983.
- [193] Chengyun Hua and Austin J. Minnich. Importance of frequency-dependent grain boundary scattering in nanocrystalline silicon and silicon-germanium thermoelectrics. Semiconductor Science and Technology, 29(12), 2014.
- [194] Zhaojie Wang, Joseph E. Alaniz, Wanyoung Jang, Javier E. Garay, and Chris Dames. Thermal conductivity of nanocrystalline silicon: Importance of grain size and frequency-dependent mean free paths. Nano Letters, 11(6):2206–2213, 2011.
- [195] A.C. Anderson. The Scattering of Phonons by Dislocations. In Phonon Scattering in Condensed Matter. Springer Series in Solid-State Sciences, volume 51. Springer, Berlin, Heidelberg, 1984.
- [196] Konstantinos Termentzidis, Mykola Isaiev, Anastasiia Salnikova, Imad Belabbas, David Lacroix, and Joseph Kioseoglou. Impact of Screw and Edge Dislocations on the Thermal Conductivity of Individual Nanowires and Bulk GaN: a Molecular Dynamics study. Physical Chemistry Chemical Physics, 2018.

- [197] Yuan Yu, Chongjian Zhou, Siyuan Zhang, Min Zhu, Matthias Wuttig, Christina Scheu, Dierk Raabe, Gerald Jeffrey Snyder, Baptiste Gault, and Oana Cojocaru-Mirédin. Revealing nano-chemistry at lattice defects in thermoelectric materials using atom probe tomography. Materials Today, 32(February):260–274, 2020.
- [198] Marat Khafizov, In Wook Park, Aleksandr Chernatynskiy, Lingfeng He, Jianliang Lin, John J. Moore, David Swank, Thomas Lillo, Simon R. Phillpot, Anter El-Azab, and David H. Hurley. Thermal conductivity in nanocrystalline ceria thin films. Journal of the American Ceramic Society, 97(2):562–569, 2014.
- [199] Ho Sun Shin, Seong Gi Jeon, Jin Yu, Yong Sung Kim, Hyun Min Park, and Jae Yong Song. Twin-driven thermoelectric figure-of-merit enhancement of Bi_2Te_3 nanowires. Nanoscale, 6(11):6158–6165, 2014.
- [200] Guodong Li, Jiangang He, Qi An, Sergey I. Morozov, Shiqiang Hao, Pengcheng Zhai, Qingjie Zhang, William A. Goddard, and G. Jeffrey Snyder. Dramatically reduced lattice thermal conductivity of Mg_2Si thermoelectric material from nanotwinning. Acta Materialia, 169:9–14, 2019.
- [201] Jun Mao, Yumei Wang, Zihang Liu, Binghui Ge, and Zhifeng Ren. Phonon scattering by nanoscale twin boundaries. Nano Energy, 32(October 2016):174–179, 2017.
- [202] Huicong Dong, Jianwei Xiao, Roderick Melnik, and Bin Wen. Weak phonon scattering effect of twin boundaries on thermal transmission. Scientific Reports, 6(1):19575, 2016.
- [203] Jan K. Bohrer, Kevin Schröer, Lothar Brendel, and Dietrich E. Wolf. Thermal resistance of twist boundaries in silicon nanowires by nonequilibrium molecular dynamics. AIP Advances, 7:045105, 2017.
- [204] Sheng-Hong Ju and Xin-Gang Liang. Investigation on interfacial thermal resistance and phonon scattering at twist boundary of silicon. Journal of Applied Physics, 113:053513, 2013.
- [205] E. S. Landry and A. J. H. McGaughey. Thermal boundary resistance predictions from molecular dynamics simulations and theoretical calculations. Physical Review B, 80(16):165304, 2009.
- [206] Tianzhuo Zhan, Satoshi Minamoto, Yibin Xu, Yoshihisa Tanaka, and Yutaka Kagawa. Thermal boundary resistance at Si/Ge interfaces by molecular dynamics simulation. AIP Advances, 5(4):047102, 2015.
- [207] Patrick E. Hopkins. Thermal transport across solid interfaces with nanoscale imperfections: Effects of roughness, disorder, dislocations, and bonding on thermal boundary conductance. ISRN Mechanical Engineering, 2013(1), 2013.

- [208] Xiaobo Li and Ronggui Yang. Effect of lattice mismatch on phonon transmission and interface thermal conductance across dissimilar material interfaces. Physical Review B, 86:054305, 2012.
- [209] Theodorian Borca-Tasciuc, Weili Liu, Jianlin Liu, Taofang Zeng, David W. Song, Caroline D. Moore, Gang Chen, Kang L. Wang, Mark S. Goorsky, Tamara Radetic, Ronald Gronsky, Takaaki Koga, and Mildred S. Dresselhaus. Thermal conductivity of symmetrically strained Si/Ge superlattices. Superlattices and Microstructures, 28(3):199 – 206, 2000.
- [210] S.-M. Lee, David G. Cahill, and Rama Venkatasubramanian. Thermal conductivity of Si–Ge superlattices. Applied Physics Letters, 70(22):2957–2959, 1997.
- [211] A. P. Merkle and L. D. Marks. A predictive analytical friction model from basic theories of interfaces, contacts and dislocations. Tribology Letters, 26(1):73–84, 2007.
- [212] Mingda Li. Quantized Dislocations. Journal of Physics: Condensed Matter, 31, 2019.
- [213] Toshiyuki Ninomiya. Dislocation Vibration and Phonon Scattering. Journal of the Physical Society of Japan, 25(3), 1968.
- [214] V.I. Alshits and Y.M. Sandler. Flutter Mechanisms of Dislocation Drag. Physica Status Solidi (B), 64(K45), 1974.
- [215] Jay Amrit, Aymeric Ramiere, and Sebastian Volz. Role of fluttering dislocations in the thermal interface resistance between a silicon crystal and plastic solid He 4. Physical Review B, 97(1):1–8, 2018.
- [216] Prepared as CHiMaD Materials Design Educational Content.
- [217] Yukari Katsura, Masaya Kumagai, Takushi Kodani, Mitsunori Kaneshige, Yuki Ando, Sakiko Gunji, Yoji Imai, Hideyasu Ouchi, Kazuki Tobita, Kaoru Kimura, and Koji Tsuda. Data-driven analysis of electron relaxation times in pbte-type thermoelectric materials. Science and Technology of Advanced Materials, 20(1):511–520, 2019.
- [218] Hang Zhang and Austin J Minnich. The best nanoparticle size distribution for minimum thermal conductivity. Scientific Reports, 5(1):8995, 2015.
- [219] N Mingo, D Hauser, N P Kobayashi, M Plissonnier, and A Shakouri. “Nanoparticle-in-Alloy” Approach to Efficient Thermoelectrics: Silicides in SiGe. Nano Letters, 9(2):711–715, feb 2009.
- [220] Arun Kumar, Gaganpreet Kaur, and Anandh Subramaniam. Critical sizes for coherent to semicoherent transition in precipitates. International Journal of Materials Research, 104(12):1171–1181, 2013.

- [221] Aniruddha Biswas, Donald J. Siegel, and David N. Seidman. Simultaneous segregation at coherent and semicoherent heterophase interfaces. Physical Review Letters, 105(7):1–4, 2010.
- [222] Riley Hanus, Matthias T. Agne, Alexander J. E. Rettie, Zhiwei Chen, Gangjian Tan, Duck Young Chung, Mercouri G. Kanatzidis, Yanzhong Pei, Peter W. Voorhees, and G. Jeffrey Snyder. Lattice softening significantly reduces thermal conductivity and leads to high thermoelectric efficiency. Advanced Materials, 31(21):1900108, 2019.
- [223] Massoud Kaviany. Heat Transfer Physics. Cambridge University Press, 2 edition, 2014.
- [224] Takuma Hori. Verification of the phonon relaxation time approximation by probing the relaxation process of a single excited mode. Phys. Rev. B, 100:214116, Dec 2019.
- [225] Micheline Roufousse and P.G. Klemens. Thermal Conductivity of Complex Dielectric Solids. Physical Review B, 7(12):5379–5386, 1976.
- [226] Rizwan Akram, Yonggao Yan, Dongwang Yang, Xiaoyu She, Gang Zheng, Xianli Su, and Xinfeng Tang. Microstructure and thermoelectric properties of Sb doped $\text{Hf}_{0.25}\text{Zr}_{0.75}\text{NiSn}$ Half-Heusler compounds with improved carrier mobility. Intermetallics, 74:1–7, 2016.
- [227] O Appel and Y Gelbstein. A Comparison Between the Effects of Sb and Bi Doping on the Thermoelectric Properties of the $\text{Ti}_{0.3}\text{Zr}_{0.35}\text{Hf}_{0.35}\text{NiSn}$ Half-Heusler Alloy. Journal of Electronic Materials, 43(6):1976–1982, 2014.
- [228] Xiao-Ya LI, Ye-Feng Bao, Yi Fan, and Yong-Fen Jiang. Effect of sb doping on thermoelectric property of n-type half-heusler compounds. Journal of Inorganic Materials, 29(9):931–935, 2014.
- [229] M. Gürth, G. Rogl, V. V. Romaka, A. Grytsiv, E. Bauer, and P. Rogl. Thermoelectric high ZT half-Heusler alloys $\text{Ti}_{1-x-y}\text{Zr}_x\text{Hf}_y\text{NiSn}$ ($0 \leq x \leq 1$; $0 \leq y \leq 1$). Acta Materialia, 104:210–222, 2016.
- [230] Ken Kurosaki, Takuji Maekawa, Hiroaki Muta, and Shinsuke Yamanaka. Effect of spark plasma sintering temperature on thermoelectric properties of (Ti,Zr,Hf)NiSn half-Heusler compounds. Journal of Alloys and Compounds, 397(1):296–299, 2005.
- [231] H. Muta, T. Yamaguchi, K. Kurosaki, and S. Yamanaka. Thermoelectric properties of zrnisn based half heusler compounds. In ICT 2005. 24th International Conference on Thermoelectrics, 2005., pages 351–354, 2005.
- [232] Sascha Populoh, Oliver C. Brunko, Krzysztof Gallazka, Wenjie Xie, and Anke Weidenkaff. Half-heusler (TiZrHf)NiSn unileg module with high powder density. Materials, 6(4):1326–1332, 2013.

- [233] S. Sakurada and N. Shutoh. Effect of Ti substitution on the thermoelectric properties of (Zr,Hf)NiSn half-Heusler compounds. Applied Physics Letters, 86(8):1–3, 2005.
- [234] M. B. Tang and J. T. Zhao. Low temperature transport and thermal properties of half-Heusler alloy Zr_{0.25}Hf_{0.25}Ti_{0.5}NiSn. Journal of Alloys and Compounds, 475(1-2):5–8, 2009.
- [235] Cui Yu, Hanhui Xie, Chenguang Fu, Tiejun Zhu, and Xinbing Zhao. High performance half-Heusler thermoelectric materials with refined grains and nanoscale precipitates. Journal of Materials Research, 27(19):2457–2465, 2012.
- [236] Cui Yu, Tie-Jun Zhu, Rui-Zhi Shi, Yun Zhang, Xin-Bing Zhao, and Jian He. High-performance half-Heusler thermoelectric materials Hf_{1-x}Zr_xNiSn_{1-y}Sb_y prepared by levitation melting and spark plasma sintering. Acta Materialia, 57(9):2757–2764, 2009.
- [237] R. A. Downie, D. A. MacLaren, and J.-W. G. Bos. Thermoelectric performance of multiphase XNiSn (X = Ti, Zr, Hf) half-Heusler alloys. J. Mater. Chem. A, 2:6107–6114, 2014.
- [238] Yintu Liu, Hanhui Xie, Chenguang Fu, G. Jeffrey Snyder, Xinbing Zhao, and Tiejun Zhu. Demonstration of a phonon-glass electron-crystal strategy in (Hf,Zr)NiSn half-Heusler thermoelectric materials by alloying. J. Mater. Chem. A, 3:22716–22722, 2015.
- [239] Michael Schwall. Heusler compounds for thermoelectric applications. PhD thesis, Johannes Gutenberg University of Mainz, 2012.
- [240] Elisabeth Rausch, Benjamin Balke, Siham Ouardi, and Claudia Felser. Enhanced thermoelectric performance in the p-type half-Heusler (Ti/Zr/Hf)CoSb_{0.8}Sn_{0.2} system via phase separation. Phys. Chem. Chem. Phys., 16:25258–25262, 2014.
- [241] Elisabeth Rausch, Benjamin Balke, Torben Deschauer, Siham Ouardi, and Claudia Felser. Charge carrier concentration optimization of thermoelectric p-type half-Heusler compounds. APL Materials, 3(4):041516, 2015.
- [242] Pengfei Qiu, Xiangyang Huang, Xihong Chen, and Lidong Chen. Enhanced thermoelectric performance by the combination of alloying and doping in TiCoSb-based half-Heusler compounds. Journal of Applied Physics, 106(10):103703, 2009.
- [243] W. Silpawilawan, K. Kurosaki, Y. Ohishi, H. Muta, and S. Yamanaka. Fenbsb p-type half-Heusler compound: beneficial thermomechanical properties and high-temperature stability for thermoelectrics. J. Mater. Chem. C, 5:6677–6681, 2017.
- [244] T. Sekimoto, K. Kurosaki, H. Muta, and S. Yamasaka. Thermoelectric and thermophysical properties of TiCoSb, ZrCoSb, HfCoSb prepared by SPS. In ICT 2005. 24th International Conference on Thermoelectrics, 2005., pages 347–350, 2005.

- [245] Shan Li, Hangtian Zhu, Jun Mao, Zhenzhen Feng, Xiaofang Li, Chen Chen, Feng Cao, Xingjun Liu, David J Singh, Zhifeng Ren, and Qian Zhang. n-Type TaCoSn-Based Half-Heuslers as Promising Thermoelectric Materials. ACS Applied Materials & Interfaces, 11(44):41321–41329, nov 2019.
- [246] Sadeq Hooshmand Zaferani, Alireza Darebaghi, Soon-Jik Hong, Daryoosh Vashae, and Reza Ghomashchi. Experimental realization of heavily p-doped half-heusler covsn compound. Energies, 13(6), 2020.
- [247] Matthew A. Hopcroft, William D. Nix, and Thomas W. Kenny. What is the Young’s modulus of silicon? Journal of Microelectromechanical Systems, 19(2):229–238, 2010.
- [248] Jose M. Escalante. Non-linear behavior of germanium electronic band structure under high strain. Computational Materials Science, 152(May):223–227, 2018.

APPENDIX A

Phonon Boltzmann Transport Equation

The phonon Boltzmann Transport Equation (BTE) tracks spatiotemporal changes in the phonon occupation ($n_{\mathbf{q}s}$; for an example phonon mode indexed as $\mathbf{q}s$; See Section 2.1) in response to various applied fields and scattering sources. The general form for the phonon BTE in the presence of a temperature gradient is [24]:

$$(A.1) \quad -\mathbf{v}_{\mathbf{q}s} \cdot \nabla T \frac{\partial n_{\mathbf{q}s}}{\partial T} + \left. \frac{\partial n_{\mathbf{q}s}}{\partial t} \right|_{\text{scatt}} = 0$$

The RHS of the above equation summarizes total rate of change in phonon occupation $n_{\mathbf{q}s}$ due to diffusion in the presence of the temperature gradient and scattering processes, and in steady state heat flow, this total rate of change should vanish to 0. Here, we will primarily summarize the common assumptions made in order to make the phonon BTE tractable. The section primarily follows the texts by Srivastava [46], Ziman [29], and Kaviani [223].

Equation A.1 can generally not be solved as is, and requires some simplification. We first assume that the deviation from the equilibrium distribution $n_{\mathbf{q}s}^0$, the Bose-Einstein distribution in this case, is small. In the presence of a finite temperature gradient, the temperature dependence of the phonon occupation should not deviate significantly from $\partial n_{\mathbf{q}s}^0 / \partial T$, which we can substitute into the first term. In the second term, related to the rate of change due to scattering, we can use the linear term in the Taylor expansion around $n_{\mathbf{q}s}^0$ by replacing $n_{\mathbf{q}s}$ with $n_{\mathbf{q}s} - n_{\mathbf{q}s}^0$. The linearized form is then given by:

$$(A.2) \quad -\mathbf{v}_{\mathbf{q}s} \cdot \nabla T \frac{\partial n_{\mathbf{q}s}^0}{\partial T} + \left. \frac{\partial (n_{\mathbf{q}s} - n_{\mathbf{q}s}^0)}{\partial t} \right|_{\text{scatt}} = 0$$

The next approximation commonly made is the single mode relaxation time (SMRT) approximation. While it is somewhat questionable in its premise, the SMRT performs well when evaluating thermal conductivity and the influence of defects even under large non-equilibrium conditions [224]. In the physical picture suggested by the SMRT, all phonon modes are at thermal equilibrium except a single mode, which deviates slightly from $n_{\mathbf{q}s}^0$. Here it is also assumed that the deviation from equilibrium $n_{\mathbf{q}s} - n_{\mathbf{q}s}^0$ decays to 0 following a time constant, or relaxation time $\tau_{\mathbf{q}s}$, which does not itself depend on the non-equilibrium phonon distribution before or after the scattering event.

$$(A.3) \quad n_{\mathbf{q}s} - n_{\mathbf{q}s}^0 = \exp\left(-\frac{t}{\tau_{\mathbf{q}s}}\right)$$

As a result, the linearized BTE in the SMRT approximation simplifies to:

$$(A.4) \quad -\mathbf{v}_{\mathbf{q}s} \cdot \nabla T \frac{\partial n_{\mathbf{q}s}^0}{\partial T} = -\frac{n_{\mathbf{q}s} - n_{\mathbf{q}s}^0}{\tau_{\mathbf{q}s}}$$

The heat flux is given by the expression below in terms of the phonon energy $\hbar\omega_{\mathbf{q}s}$, the group velocity $\mathbf{v}_{\mathbf{q}s}$, and the deviation from the equilibrium distribution $n'_{\mathbf{q}s} = n_{\mathbf{q}s} - n_{\mathbf{q}s}^0$.

$$(A.5) \quad \mathbf{j} = \frac{1}{(2\pi)^3} \sum_s \int \hbar\omega_{\mathbf{q}s} \mathbf{v}_{\mathbf{q}s} n'_{\mathbf{q}s} d\mathbf{q}$$

Substituting the expression for $n'_{\mathbf{q}s}$, the heat current is then equal to:

$$(A.6) \quad \mathbf{j} = \frac{\nabla T}{(2\pi)^3} \sum_s \int \hbar\omega_{\mathbf{q}s} \mathbf{v}_{\mathbf{q}s} \tau_{\mathbf{q}s} \frac{\partial n_{\mathbf{q}s}^0}{\partial T} d\mathbf{q}.$$

We can then substitute in the modal heat capacity $C_{\mathbf{q}s} = \hbar\omega_{\mathbf{q}s} \frac{\partial n_{\mathbf{q}s}^0}{\partial T}$. Then, noting the relationship between heat flux and thermal conductivity set by Fourier's law, $\mathbf{j} = -\kappa \nabla T$, the thermal conductivity equals the following sum over modal contributions, which follows the basic form of the phonon gas model shown in Equation 2.29.

$$(A.7) \quad \kappa = \frac{1}{(2\pi)^3} \sum_s \int C_{\mathbf{q}s} \mathbf{v}_{\mathbf{q}s} \tau_{\mathbf{q}s} d\mathbf{q}.$$

To convert this into an integral over spectral rather than modal quantities, a Brillouin zone integration must be performed using a scheme like Gaussian smearing or the tetrahedron method [167].

APPENDIX B

Phonon Relaxation Time Derivations

The derivations here follow the work of Klemens and are primarily summaries of the following three works: Klemens 1955 [56], Roufosse and Klemens 1976 [225], and Klemens 1958 [37]. These phonon lifetimes are determined from the standpoint of Fermi's Golden Rule and first order perturbation theory. Previous work has shown that higher order perturbation terms have a negligible effects on the lattice energy [72, 81].

B.1. Mass Defect Scattering

As introduced in Section 2.2.2, Fermi's Golden Rule relates the scattering rate of an incident phonon $\mathbf{q}s$ to the perturbation matrix element, a measure of the overlap between two phonon states due to a perturbation to the lattice energy. The perturbation matrix element in the derivation of Klemens includes a coefficient (C), which captures the physics of the perturbation induced by the point defect, while $a(\mathbf{q}s)$ and $a^*(\mathbf{q}'s')$ are creation and annihilation operators to represent the change in occupation numbers of the $\mathbf{q}s$ and $\mathbf{q}'s'$ states as a result of the phonon-impurity interaction.

$$(B.1) \quad \langle \mathbf{q}s | H' | \mathbf{q}'s' \rangle = C(\mathbf{q}s, \mathbf{q}'s') a(\mathbf{q}s) a^*(\mathbf{q}'s')$$

Substituting in the full form of the creation and annihilation operators gives the expression below, where N refers to the number of phonons in a given state.

$$(B.2) \quad |\langle \mathbf{q}s | H' | \mathbf{q}'s' \rangle|^2 = \frac{\hbar^2}{M^2 \omega^2} C^2(\mathbf{q}s, \mathbf{q}'s') [N(N' + 1) - N'(N + 1)]$$

It has been shown that the term in the square brackets reduces to 1 in the integral over the constant energy surface corresponding to final \mathbf{q}' states [56]. To calculate the value of C , it is useful once more to look at the real space representation of the lattice perturbation. Equation 3.1 giving the energy perturbation (E') to the lattice due to mass difference is reproduced here:

$$(B.3) \quad E'(\mathbf{R}) = \frac{1}{2} \Delta M(\mathbf{R}) \dot{u}^2(\mathbf{R}).$$

To evaluate $|\langle \mathbf{q} | H' | \mathbf{q}' \rangle|^2$ we must first take the Fourier transform of $M(\mathbf{R})$ so that it is in terms of the scattering vector $\mathbf{Q} = \mathbf{q}'s' - \mathbf{q}s$. Here, S refers to the number of sites in the lattice [72, 77].

$$(B.4) \quad \Delta \tilde{M}(\mathbf{Q}) = \frac{1}{S} \sum_{\mathbf{R}} \Delta M(\mathbf{R}) e^{i\mathbf{Q}\mathbf{R}}$$

The expression for C^2 picks up a factor of $\Delta\tilde{M}(\mathbf{Q})\Delta\tilde{M}(\mathbf{Q}')$, which is equal to:

$$(B.5) \quad \Delta\tilde{M}(\mathbf{Q})\Delta\tilde{M}(\mathbf{Q}') = \frac{1}{S^2} \sum_{\mathbf{R}, \mathbf{R}'} \Delta M(\mathbf{R})\Delta M(\mathbf{R}') e^{i(\mathbf{Q}'\mathbf{R}' - \mathbf{Q}\mathbf{R})}$$

If the approximation is made that the point defects are randomly distributed over the lattice, the sum over lattice sites can instead be written as an average squared mass difference (ΔM^2) times the number of defect sites in the lattice (S_i) [72, 77], which yields a factor of defect site fraction f_i .

$$(B.6) \quad \Delta\tilde{M}(\mathbf{Q})\Delta\tilde{M}(\mathbf{Q}') = \frac{1}{S} \frac{S_i}{S} \Delta M^2 = \frac{1}{S} f_i \Delta M^2$$

Next, the velocity squared $\dot{\mathbf{u}}^2(\mathbf{R})$ term can be written as before as a double sum over normal modes—the full form of which is shown in Equation 3.2. However, in contrast to our scattering potential derivation shown in Section 2.2.2, we will focus here on off-diagonal terms where $\mathbf{q} \neq \mathbf{q}'$, as these indicate a phonon transition. Given the frequency conservation implied by elastic scattering, $\omega_{\mathbf{q}} = \omega_{\mathbf{q}'}$. Finally, the creation and annihilation operators are related to the displacement amplitudes as: $a(\mathbf{q}) = A_{\mathbf{q}} \exp(i\omega_{\mathbf{q}}t)$. The off-diagonal terms reduce to the following form:

$$(B.7) \quad \dot{\mathbf{u}}^2(\mathbf{q}s, \mathbf{q}'s') = a_{\mathbf{q}s} a_{\mathbf{q}'s'}^* \omega^2 [\mathbf{e}_{\mathbf{q}}(\mathbf{R}) \cdot \mathbf{e}_{\mathbf{q}'}(\mathbf{R})] \exp(i(\mathbf{q}s + \mathbf{q}'s') \cdot \mathbf{R})$$

For an isolated defect, the phase factor, $\exp(i(\mathbf{q} + \mathbf{q}') \cdot \mathbf{R})$, can be neglected, but it does effect the final scattering phase space in clusters of point defect. Finally, the annihilation/creation operator factor ($a_{\mathbf{q}} a_{\mathbf{q}'}^*$) can be dropped, since this is already accounted for in the simplified matrix element shown in Equation B.2. Combining Equations B.6 and B.7, the final expression for $C^2(\mathbf{Q})$ is then:

$$(B.8) \quad C^2(\mathbf{Q}) = \frac{1}{4S} f_i (\Delta M)^2 \omega^4 |\mathbf{e}_{\mathbf{q}s}(\mathbf{R}) \cdot \mathbf{e}_{\mathbf{q}'s'}(\mathbf{R})|^2$$

Substituting this expression in for the transition probability $W_{\mathbf{q}, \mathbf{q}'}$ described by Fermi's Golden Rule (Equation 2.18), we get:

$$(B.9) \quad W_{\mathbf{q}, \mathbf{q}'} = \frac{\pi}{2S} f_i \frac{\Delta M^2}{M^2} \omega^2 \delta(\Delta\omega) |\mathbf{e}_{\mathbf{q}s}(\mathbf{R}) \cdot \mathbf{e}_{\mathbf{q}'s'}(\mathbf{R})|^2$$

The remainder of the derivation follows the one provided in the main text (Section 3.2) closely. We apply Equation 2.21 to calculate the scattering rate by integrating over all possible final phonon states $\mathbf{q}'s'$. Here, polarization dependence is preserved, so we must integrate over 3 surfaces defined by $\omega = \omega'$, corresponding to the polarizations s' . On average, the dot product of the polarization vectors $|\mathbf{e}_{\mathbf{q}s}(\mathbf{R}) \cdot \mathbf{e}_{\mathbf{q}'s'}(\mathbf{R})|^2$ will additionally yield a factor of 1/3. The resulting scattering rate is then identical to Equation 3.6.

B.2. Phonon-Phonon Scattering

The umklapp scattering rate follows a similar derivation, however, the conservation rule is more complicated since the process involves three phonon modes ($\mathbf{q}, \mathbf{q}', \mathbf{q}''$) as well as momentum exchange with the lattice via the addition or subtraction of a reciprocal lattice vector (\mathbf{b}). The

derivation here is adopted from the derivation by Klemens for strain scattering off a point defect, however in this case, the strain is produced by another phonon rather than a point imperfection [37].

$$(B.10) \quad \mathbf{q} + \mathbf{b} = \mathbf{q}' + \mathbf{q}''$$

The umklapp perturbation matrix element is similar in form to that of point defect scattering, but now includes three creation or annihilation operators since the process involves the change in occupation number for three phonon modes. Additionally, the coefficient (C_U) is dependent on the anharmonicity of the lattice.

$$(B.11) \quad \langle i | H' | f \rangle^2 = [C_U(\mathbf{q}, \mathbf{q}', \mathbf{q}'') a(q) a^*(q') a^*(q'')]^2 = \frac{\hbar^3}{M^3 \omega \omega' \omega''} C_U^2(\mathbf{q}, \mathbf{q}', \mathbf{q}'') [(N+1)(N'+1)(N''+1) - NN'N'']$$

In Klemens, the phonon mode q'' is treated as a Fourier strain component producing a perturbation to the lattice energy. If a uniform dilatational strain (Δ) is assumed, the Fourier component can be written as $i\omega''/v_p(\omega'')\sqrt{S}$ in the limit $q'' \rightarrow 0$. The elastic strain impacts force constants, and therefore induces a frequency shift captured by the Grüneisen model [37].

$$(B.12) \quad \omega(\mathbf{q}) = \omega_0(\mathbf{q})[1 - \gamma(\mathbf{q})\Delta]$$

The coefficient C_U then represents the lattice energy change associated with a uniform dilatational strain.

$$(B.13) \quad C_U(\mathbf{q}, \mathbf{q}', \mathbf{q}'') = \frac{-2i}{\sqrt{S}v_p(q'')} \gamma M \omega \omega' \omega''$$

The final component of the squared matrix element (shown in Equation B.11) is the term in the square brackets, representing the difference in occupation of phonon modes from the initial to final state. At the high temperature limit, this term can be written in terms of the Bose-Einstein distribution such that it reduces to: $k_B T \omega / \hbar \omega' \omega''$. The full form of the squared matrix element simplifies to the form shown below.

$$(B.14) \quad \langle i | H' | f \rangle^2 = \frac{\hbar^2}{M} \frac{4\gamma^2 \omega^2}{S v_p^2(q'')} k_B T$$

Just as before, the scattering probability is defined using Fermi's Golden Rule (Equation 2.18), where the initial and final states are now represented as $|i\rangle$ and $|f\rangle$, for simplicity. As before, the scattering rate is calculated by summing over $W_{i,f}$ for all possible final states. This is achieved by performing a sum over all \mathbf{q}' and \mathbf{b} , which then fixes the value of \mathbf{q}'' as a result of the conservation condition (Equation B.10).

$$(B.15) \quad \tau_U = \sum_{\mathbf{q}', \mathbf{b}} W_{i,f}$$

It is assumed that \mathbf{q}' is restricted to spheres of radius $\frac{1}{2}(q + b)$, which is suggested to be true as long as the dispersion relation is not modified by the zone structure [225]. Therefore, the sum can be once again replaced by a surface integral over this sphere, and picks up a volume factor of $V_{\text{tot}}/(2\pi^3)$, where V_{tot} is the volume of the crystal.

$$(B.16) \quad \tau_{\text{U}}^{-1} = \sum_{\mathbf{b}} \frac{V_{\text{tot}}}{(2\pi)^3} \int W_{i,f} d^3\mathbf{k}'$$

Following the same integral simplifications discussed in the derivation of τ_{PD} , the scattering rate due to umklapp processes is shown below.

$$(B.17) \quad \tau_{\text{U}}^{-1} = \frac{V_0 \pi \gamma^2 \omega^2}{M v_{\text{p}}^2(\omega'') v_{\text{g}}(\omega')} \sum_{\mathbf{b}} (q + b)^2$$

Finally, the approximation is made that q is small in magnitude in comparison to the reciprocal lattice vector $b = 2\pi/a$, such that $(q + b)^2 = 4\pi^2/a^2$. For a cubic close-packed material with a rhombohedral primitive unit cell, the volume per site V_0 is $a^3(\sqrt{2})^{-1}$, and the scattering rate reduces to the form shown below.

$$(B.18) \quad \tau_{\text{U}}^{-1} = \frac{4\pi a \gamma^2 T k_{\text{B}}}{\sqrt{2} M} \frac{\omega^2}{v_{\text{p}}^2(\omega'') v_{\text{g}}(\omega')}$$

APPENDIX C

Elaborated Example of Vacancy Scattering

This section provides a full example of the phonon-vacancy scattering model applied to literature values. The thermal conductivity measurements from Wang *et al.* are utilized for $\text{La}_{1-x}\text{CoO}_{3-y}$ with La and O vacancies. The mass difference scattering strength is given by the expression below, where \overline{M}_1 is the average mass of the La site and \overline{M}_3 is the average mass of the O site. Here, the average atomic mass in the compound $\langle \overline{M} \rangle = (\overline{M}_1 + M_{\text{Co}} + 3\overline{M}_3)/5$.

$$(C.1) \quad \Gamma_{\text{M}} = \frac{(1/5)(x(0 - \overline{M}_1)^2 + (1-x)(M_{\text{La}} - \overline{M}_1)^2 + 3(y(0 - \overline{M}_3)^2 + (1-y)(M_{\text{O}} - \overline{M}_3)^2))}{\langle \overline{M} \rangle^2}$$

In the original text, the full thermal conductivity reduction is explained using mass difference scattering alone, without the perturbation due to broken bonds. However, in this case, the volume in Equation 12 of the text was incorrectly defined as the volume of the primitive unit cell when defining the point defect relaxation, where it should have been defined as the volume per atom. This error compensates for the missing broken bonds term, such that the curve reported in the paper still adequately represents the data, and the main conclusions about the point defect scattering strength hold. However, using the virial theorem treatment, the above equation can be adjusted by tripling the mass difference on both vacancy sites as shown below.

$$(C.2) \quad \Gamma_{\text{M}} = \frac{(1/5)(x(-M_{\text{La}} - 2\langle \overline{M} \rangle)^2 + (1-x)(M_{\text{La}} - \overline{M}_1)^2 + 3(y(-M_{\text{O}} - 2\langle \overline{M} \rangle)^2 + (1-y)(M_{\text{O}} - \overline{M}_3)^2))}{\langle \overline{M} \rangle^2}$$

Figure C.1 includes: 1) the model in the original paper using the unit cell volume (V_{uc}), 2) the revised mass difference only model where the volume per atom (V_0) is used, and 3) the model with the virial theorem treatment for broken bonds, where V_0 is used. As in the original paper by Wang *et al.*, it is assumed that $x = y$ in the defective chemical formula [88].

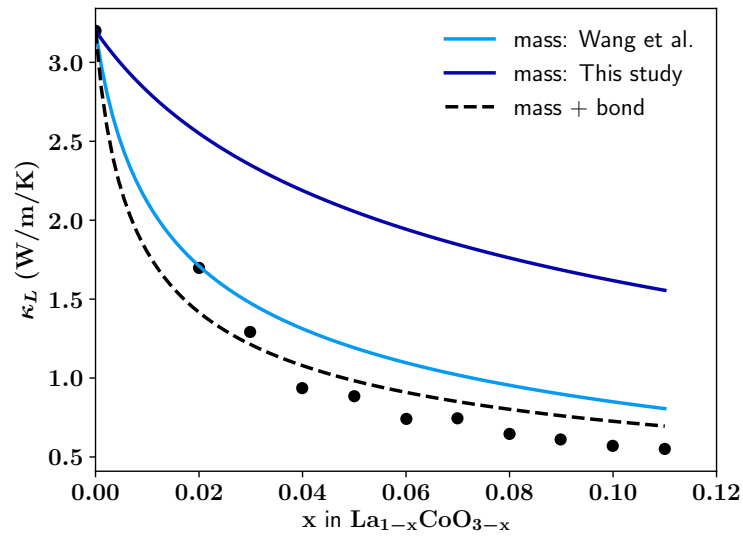


Figure C.1. **Phonon-Vacancy Scattering: Virial Theorem Model versus Experiment** The mass difference model with the unit cell volume error (light blue) is compared to the mass difference only model described in this study (dark blue) as well as the vacancy model (dashed) with the virial treatment for broken bonds, which best captures the κ_L reduction [88].

APPENDIX D

Pseudoternary half-Heusler Data Summary

Summary of literature data used in the alloy scattering models. Data collection was greatly facilitated by the use of the StarryData2 database [217].

Table D.1. **Experimental Transport Function (σ_{E0}) and Lattice Thermal Conductivity (κ_L) Values from Literature for the $XNiSn$ System** The σ_{E0} values were calculated using the approach described in Section 4.2.1 when S and σ pairs were available for samples at multiple doping levels. The κ_L values were calculated by subtracting off the electronic thermal conductivity term modeled using the Wiedemann-Franz law.

x(TiNiSn)	x(ZrNiSn)	x(HfNiSn)	σ_{E0} (S/m)	κ_L (W/m/K)	Dopant	Source
0	0.25	0.75	70125	5.38	Sb	[226]
0.3	0.35	0.35		3.88	Bi	[132]
0.3	0.35	0.35		3.66	excess Ni	[227]
0	0	1		6.38		[124]
0	1	0		6.74		[124]
1	0	0		3.85		[124]
0.5	0.5	0		3.31		[124]
0.5	0	0.5		2.45		[124]
0	0.5	0.5		2.3		[124]
0.5	0.25	0.25		2.83		[124]
0.5	0.25	0.25	60937	2.91	Sb	[228]
0.25	0.75	0		3.07		[229]
0.5	0.5	0		2.42		[229]
0.75	0.25	0		3.73		[229]
1	0	0		3.18		[229]
0	1	0		3.49		[229]
0.25	0	0.75		2.87		[229]
0.5	0	0.5		2.75		[229]
0.75	0	0.25		2.48		[229]
0	0	1		3.46		[229]
0	0.75	0.25		4.13		[229]
1	0	0	84677	6.95	Sb	[137]
0.95	0	0.05	116606	5.21	Sb	[137]
0.8	0	0.2	76209	4.94	Sb	[137]

Continued on next page

x(TiNiSn)	x(ZrNiSn)	x(HfNiSn)	σ_{E0} (S/m)	κ_L (W/m/K)	Dopant	Source
0.3	0.35	0.35		3.58		[230]
0	1	0		12.72		[231]
0.3	0.7	0		7.39		[231]
0.5	0.5	0		5.30		[231]
0.5	0.5	0		4.67		[231]
0.33	0.33	0.33		5.67		[232]
0	0.5	0.5		2.81		[232]
0	0.5	0.5		4.16		[232]
0	0.5	0.5		3.99		[233]
0.2	0.4	0.4		3.74		[233]
0.3	0.35	0.35		3.09		[233]
0.5	0.25	0.25	158357	2.92	Sb	[233]
0.7	0.15	0.15		3.3		[233]
0.5	0.25	0.25		3.3		[234]
0	0.75	0.25		3.61		[235]
0	0.4	0.6	85158	3.3	Sb	[236]
0	0.3	0.7	72348	4	Sb	[236]
0.5	0.5	0	63378	4	Sb	[237]
0	0.9	0.1	107439	3.3	Sb	[145]
0	0.2	0.8	93747	4.5	Sb	[238]
0	0	1	85915	6.5	Sb	[238]
0.5	0.25	0.25	43947	3.58	Sb	[133]
0.43	0.28	0.29	35671	5.6		[239]
0.21	0.4	0.39	50008	9.1		[239]

Table D.2. **Experimental Transport Function (σ_{E0}) and Lattice Thermal Conductivity (κ_L) Values from Literature for the XFeSb System** All values are reported for samples with 20% Ti doping. The κ_L values were calculated by subtracting off the electronic thermal conductivity term modeled using the Wiedemann-Franz law.

x(VFeSb)	x(NbFeSb)	x(TaFeSb)	σ_{E0} (S/m)	κ_L (W/m/K)	Dopant	Source
0.05	0.95	0	120353	4.85	Ti	[98]
0.1	0.9	0	129429	4.52	Ti	[98]
0.25	0.75	0	115760	3.69	Ti	[98]
0.4	0.6	0	97073	3.07	Ti	[98]
0.55	0.45	0	92508	3.28	Ti	[98]
0.7	0.3	0	81242	3.18	Ti	[98]
0.85	0.15	0	76770	3.44	Ti	[98]

Continued on next page

x(VFeSb)	x(NbFeSb)	x(TaFeSb)	σ_{E0} (S/m)	κ_L (W/m/K)	Dopant	Source
1	0	0	47298	3.17	Ti	[98]
0	1	0	130483	4.45	Ti	[98]
0	0.96	0.04	666753	3.99	Ti	[97]
0	0.88	0.12	540480	3.47	Ti	[97]
0	0.8	0.2	550582	2.95	Ti	[97]
0	0.76	0.24	651593	2.12	Ti	[97]
0	0.68	0.32	572491	2.39	Ti	[97]
0	0.64	0.36	548937	2.13	Ti	[97]
0	0.6	0.4	538820	1.76	Ti	[97]
0.05	0	0.95	138242	2.52	Ti	[99]
0.1	0	0.9	177881	2.33	Ti	[99]
0.15	0	0.85	247795	2.46	Ti	[99]
0.1875	0	0.8125	74954	1.22	Ti	unpublished
0.1	0.7	0.2	87960	0.95	Ti	unpublished
0.63	0	0.37	53170	3.26	Ti	unpublished
0.34125	0.325	0.33375	44879	2.03	Ti	unpublished
0	0.8	0.2	121976	3.65	Ti	unpublished
0	0.5	0.5	136446	3.64	Ti	unpublished
0	0.2	0.8	82195	3.33	Ti	unpublished
0.6	0.2	0.2	41556	2.54	Ti	unpublished
0	0	1	151851	5.5	Ti	unpublished
0	1	0	143928	7.42	Ti	unpublished

Table D.3. **Experimental Transport Function (σ_{E0}) and Lattice Thermal Conductivity (κ_L) Values from Literature for the XCoSb System** The σ_{E0} values were calculated using the approach described in Section 4.2.1 when S and σ pairs were available for samples at multiple doping levels. The κ_L values were calculated by subtracting off the electronic thermal conductivity term modeled using the Wiedemann-Franz law.

x(TiCoSb)	x(ZrCoSb)	x(HfCoSb)	σ_{E0} (S/m)	κ_L (W/m/K)	Dopant	Source
0	0	1	84928	4.39	Sb	[240]
0	0.5	0.5	73550	2.64	Sb	[240]
0.5	0	0.5	68372	2.33	Sb	[240]
0.5	0.5	0	55161	4.08	Sb	[240]
0	1	0	70354	4.39	Sb	[240]
1	0	0	56680	6.46	Sb	[240]
0.3	0.35	0.35	68706	2.4	Sb	[241]
1	0	0		14.7		[242]

Continued on next page

x(TiCoSb)	x(ZrCoSb)	x(HfCoSb)	σ_{E0} (S/m)	κ_L (W/m/K)	Dopant	Source
0.9	0.1	0	46205	10.9	Ni	[242]
0.8	0.2	0		7.64		[242]
0.6	0.4	0		6.97		[242]
0.5	0.5	0		7.6		[242]
0	1	0		15.6		[243]
0	0	1		11.9		[244]

Table D.4. **Experimental Transport Function (σ_{E0}) and Lattice Thermal Conductivity (κ_L) Values from Literature for the $XCoSn$ System** The σ_{E0} values were calculated using the approach described in Section 4.2.1 when S and σ pairs were available for samples at multiple doping levels. The κ_L values were calculated by subtracting off the electronic thermal conductivity term modeled using the Wiedemann-Franz law.

x(VCoSn)	x(NbCoSn)	x(TaCoSn)	σ_{E0} (S/m)	κ_L (W/m/K)	Dopant	Source
0	0	1	38603	5.94	Sb	[245]
0	1	0	91932	7.72	Sb	[245]
0	0.4	0.6	56619	4.8	Sb	[245]
1	0	0	16316	12.8		[246]

APPENDIX E

Grain Boundary Scattering: Model Parameters and Strain Field Descriptions

E.1. Model Parameters

The model parameters used in the Kapitza resistance calculations for the Si-Si tilt and twist boundary and Si-Ge heterointerface described in Section 5.4 are listed in Table E.1 below. Across a temperature range of 100- 800°C, the temperature dependence of the input parameters due to lattice thermal expansion had a negligible impact on the phonon relaxation time predictions. However, temperature dependent inputs could be determined from quasi-harmonic DFT calculations, for example.

Table E.1. **Parameters used in Model** Table of material property inputs used in the thermal boundary resistance model for the Si–Si tilt and twist grain boundaries as well as the Si–Ge heterointerface.

Properties	Silicon	Germanium
Speed of sound (v_s ; m/s) [19]	6084	5400
Atoms per unit cell (N)	2	2
Volume per atom (V ; Å ³) [19]	19.7	22.7
Density (ρ , kg/m ³)	2330	5323
Stiffness coefficients (c_{11}, c_{12}, c_{44} ; GPa) [247, 248]	165.6, 63.9, 79.5	126.0, 44.0, 67.7
Bulk Modulus (G ; GPa) [247]	97.83	
Grüneisen parameter (γ) [181]	1	

The most computationally demanding portion of the model is the calculation of the spectral relaxation time, owing to the integrals over incident phonon direction and phonon frequency. Running serially on a laptop, the calculation of each spectral relaxation time value $\tau(\omega)$ takes 2.16 minutes. We find that a spline of 50 spectral relaxation time $\tau(\omega)$ values are sufficient to converge the thermal boundary resistance R_K . Therefore, running serially on a laptop, each thermal boundary resistance calculation takes approximately 2 hours.

E.2. Twist Boundary Strain Field Details

The displacement vector field for a screw dislocation has only one non-zero component oriented along the line of the dislocation. Therefore, a dislocation with Burgers vector (b) parallel to \hat{z} has the following displacement field [190, p. 60]:

$$(E.1) \quad \mathbf{u}_n = (0, 0, u_z),$$

$$u_{3,n} = \frac{b}{2\pi} \arctan\left(\frac{y}{x}\right).$$

The displacement produces a pure shear state, with only two non-zero strain components:

$$(E.2) \quad \epsilon_{xz} = \epsilon_{zx} = \frac{1}{2} \frac{\partial u_z}{\partial x} = -\frac{by}{4\pi(x^2 + y^2)},$$

$$\epsilon_{yz} = \epsilon_{zy} = \frac{1}{2} \frac{\partial u_z}{\partial y} = \frac{bx}{4\pi(x^2 + y^2)}.$$

Next, we will consider the YZ array of screw dislocations spaced by D along the y -axis in order to model a low-angle twist boundary. The stress components from the dislocation array ϵ_{ij}^{YZ} can be determined from the following summation:

$$(E.3) \quad \epsilon_{ij}^{YZ} = \sum_{n=-\infty}^{\infty} \epsilon_{ij}(x, y - nD).$$

Analytic solutions to the above summation can be obtained, and are shown below [180, pp. 698-700]:

$$(E.4) \quad \epsilon_{xz}^{YZ} = -\frac{b}{2D} \left(\frac{\sin(2\pi y/D)}{\cosh(2\pi x/D) - \cos(2\pi y/D)} \right),$$

$$\epsilon_{yz}^{YZ} = \frac{b}{2D} \left(\frac{\sinh(2\pi x/D)}{\cosh(2\pi x/D) - \cos(2\pi y/D)} \right).$$

One can then evaluate the limit as $|x| \rightarrow \infty$:

$$(E.5) \quad \lim_{x \rightarrow \infty} \epsilon_{xz}^{YZ} = 0,$$

$$\lim_{x \rightarrow \infty} \epsilon_{yz}^{YZ} = \operatorname{sgn}(x) \frac{b}{2D}.$$

The ϵ_{yz}^{YZ} shear strain component persists at the long-range limit, converging to a constant value. This is energetically prohibitive for the twist boundary as a whole and shows the importance of including the ZY array of dislocations with sense vector along the y -axis, periodically spaced on the z -axis. The strain components from this array are the negative of Equation E.4 with y and z swapped, and their long-range limits are,

$$(E.6) \quad \lim_{x \rightarrow \infty} \epsilon_{xz} = 0,$$

$$(E.7) \quad \lim_{x \rightarrow \infty} \epsilon_{yz} = -\operatorname{sgn}(x) \frac{b}{2D},$$

which exactly cancel the far-field strain of the first array if both share the same b/D ratio [180].

E.3. Heterointerface Strain Field Details

As with the twist boundary, the heterointerface is taken to lie in the yz -plane with two interpenetrating arrays of dislocations, but now with edge character. Therefore, the strain fields are essentially equivalent to the tilt boundary case, requiring only a rotation such that the extra half-plane points in the x direction. They are given below for one dislocation through the origin in each of the two arrays. The notation follows Ref. [181].

Table E.2. **Heterointerface Strain Field Components** The real-space strain field components for both the YZ and ZY arrays of a semicoherent heterointerface normal to the x direction. The dilatational ϵ_Δ , shear or deviatoric ϵ_S , and rotational ϵ_R components are listed here.

YZ array	ZY array
$\epsilon_\Delta = \frac{-b(1-2\nu)}{2\pi(1-\nu)} \frac{x}{(x^2+y^2)}$	$\epsilon_\Delta = \frac{-b(1-2\nu)}{2\pi(1-\nu)} \frac{x}{(x^2+z^2)}$
$\epsilon_S = \frac{b}{4\pi(1-\nu)} \frac{y(y^2-x^2)}{(x^2+y^2)^2}$	$\epsilon_S = \frac{b}{4\pi(1-\nu)} \frac{z(z^2-x^2)}{(x^2+z^2)^2}$
$\epsilon_R = \frac{b}{\pi} \frac{y}{x^2+y^2}$	$\epsilon_R = \frac{b}{\pi} \frac{z}{x^2+z^2}$

Again, considering the YZ array, analytic solutions exist for the real-space sum over the misfit edge dislocations periodically-spaced by D . The analytic solutions for the three, independent non-zero strain components ϵ_{ij}^{YZ} in a Cartesian basis are [180, pp. 695-697] [187]:

$$(E.8) \quad \epsilon_{xx}^{YZ} = \frac{b}{4(1-\nu)D} \left[\frac{-2\nu S_X(C_X - c_Y) + 2\pi X(C_X c_Y - 1)}{(C_X - c_Y)^2} \right],$$

$$(E.9) \quad \epsilon_{yy}^{YZ} = \frac{b}{4(1-\nu)D} \left[\frac{2(1-\nu)S_X(C_X - c_Y) - 2\pi X(C_X c_Y - 1)}{(C_X - c_Y)^2} \right],$$

$$(E.10) \quad \epsilon_{xy}^{YZ} = \frac{b}{2(1-\nu)D} \left[s_Y \left(\frac{2\pi X S_X - C_X + c_Y}{(C_X - c_Y)^2} \right) \right],$$

where $X \equiv x/D$, $Y \equiv y/D$, $s_Y \equiv \sin 2\pi Y$, $c_Y \equiv \cos 2\pi Y$, $S_X \equiv \sinh 2\pi X$, and $C_X \equiv \cosh 2\pi X$.

We can again evaluate the limit as $|x| \rightarrow \infty$:

$$(E.11) \quad \lim_{x \rightarrow \infty} \epsilon_{xx}^{YZ} = \text{sgn}(x) \frac{-b\nu}{2(1-\nu)D},$$

$$(E.12) \quad \lim_{x \rightarrow \infty} \epsilon_{yy}^{YZ} = \text{sgn}(x) \frac{b}{D},$$

$$(E.13) \quad \lim_{x \rightarrow \infty} \epsilon_{xz}^{YZ} = 0.$$

Here, the dilatation strain components (ϵ_{xx}^{YZ} and ϵ_{yy}^{YZ}) persist in the far field limit, while the shear strain decays. Additionally, the far-field dilatational strain is not cancelled out by the ZY array. However, as noted in the text, the nonzero dilatation in the far field is artificial since the reference lattices are different on either side of the interface. We reiterate that this far-field dilatational strain is subtracted and treated with an acoustic mismatch term capturing the step function change in stiffness matrix at the interface.

List of Tables

5.1	Twist Boundary Fourier Strain Field Components	103
5.2	Heterointerface Fourier Strain Field Components	104
5.3	Si Twist Boundary Thermal Boundary Resistance Thermal boundary resistance (R_K ; $\text{m}^2\text{K}/\text{GW}$) comparison to previous theoretical and experimental literature results for the Si-Si symmetric twist boundary.	113
5.4	Room temperature thermal boundary resistance (R_K ; $\text{m}^2\text{K}/\text{GW}$) with comparison to theoretical and experimental literature results for Si-Ge heterointerface	116
D.1	Experimental Transport Function (σ_{E0}) and Lattice Thermal Conductivity (κ_L) Values from Literature for the <i>XNiSn</i> System The σ_{E0} values were calculated using the approach described in Section 4.2.1 when S and σ pairs were available for samples at multiple doping levels. The κ_L values were calculated by subtracting off the electronic thermal conductivity term modeled using the Wiedemann-Franz law.	156
D.2	Experimental Transport Function (σ_{E0}) and Lattice Thermal Conductivity (κ_L) Values from Literature for the <i>XFeSb</i> System All values are reported for samples with 20% Ti doping. The κ_L values were calculated by subtracting off the electronic thermal conductivity term modeled using the Wiedemann-Franz law.	157
D.3	Experimental Transport Function (σ_{E0}) and Lattice Thermal Conductivity (κ_L) Values from Literature for the <i>XCoSb</i> System The σ_{E0} values were calculated using the approach described in Section 4.2.1 when S and σ pairs were available for samples at multiple doping levels. The κ_L values were calculated by subtracting off the electronic thermal conductivity term modeled using the Wiedemann-Franz law.	158
D.4	Experimental Transport Function (σ_{E0}) and Lattice Thermal Conductivity (κ_L) Values from Literature for the <i>XCoSn</i> System The σ_{E0} values were calculated using the approach described in Section 4.2.1 when S and σ pairs were available for samples at multiple doping levels. The κ_L values were calculated by subtracting off the electronic thermal conductivity term modeled using the Wiedemann-Franz law.	159

- E.1 **Parameters used in Model** Table of material property inputs used in the thermal boundary resistance model for the Si–Si tilt and twist grain boundaries as well as the Si–Ge heterointerface. 160
- E.2 **Heterointerface Strain Field Components** The real-space strain field components for both the YZ and ZY arrays of a semicoherent heterointerface normal to the x direction. The dilatational ϵ_{Δ} , shear or deviatoric ϵ_S , and rotational ϵ_R components are listed here. 162

List of Figures

- 1.1 **zT Dependence on Doping Level** The constituents of the figure-of-merit zT each have a dependence on doping level, such that zT itself tends to be sharply peaked at an optimal doping level. Therefore, without the assurance of optimal doping, zT is an inadequate metric of the true potential of a thermoelectric material. In order to reliably compare literature values, doping-independent metrics such as the transport function σ_{E0} are therefore preferable. 15
- 2.1 **Schematic of Dispersion Approximations** Comparison of phonon dispersion approximations for half-Heusler compound, $HfNiSn$. In comparison to the full phonon dispersion (a), the Debye model (b) uses the constant classical speed of sound, which assigns a large phonon velocity even to relatively flat optical modes. The Born von Karman dispersion (c) corrects for this by having the group velocity approach 0 at the zone edge using a sinusoidal form. Finally, the hybrid Debye + Einstein model (d) uses separate functional forms to treat the acoustic branch as propagating phonons and optical branches as localized Einstein modes, which couple to one another. A Born von Karman + Einstein model can also be used to describe the acoustic branch. 24
- 2.2 **Lattice Thermal Conductivity Trends with Temperature** Plot inset shows the log-log trend to highlight temperature dependencies at the low- and high-temperature regimes. At the low-T limit, κ_L varies as T^3 , stemming from the heat capacity. A rollover occurs, characterized by the onset of resistive phonon-phonon scattering processes. Finally, beyond the Debye temperature, $\kappa_L \propto T^{-1}$, stemming from the phonon-phonon relaxation time. 30
- 2.3 **Defect Dimensionality and Fermi's Golden Rule** The main components of Fermi's Golden Rule for defects are the number density of defects (n_d), the volume containing the defect (V_d), the squared scattering matrix element ($|H'|$), and the phase space for the scattering transitions ($g(\omega)$). The last two terms contribute frequency dependencies. The defect dimensionality influences the momentum conservation and thus the available phase space. In contrast, the squared matrix element is expected to be proportional to ω^2 for any defect dimensionality. 34
- 2.4 **Phonon Gas Model Schematic** In the phonon gas model, the thermal conductivity can be written as an integral over the phonon spectrum, where the heat carried by the phonons in each frequency integral is determined by

the amount of heat they carry (spectral heat capacity; $C(\omega)$), the velocity of the phonons (spectral group velocity; $v_g(\omega)$), and the time the phonon travels between scattering events (spectral lifetime; $\tau(\omega)$). 37

- 3.1 **Schematic of Point Defect Perturbations** The lattice perturbation mechanisms of a point defect include a mass difference (ΔM), harmonic force constant difference (ΔK), and strain scattering from site radius difference (ΔR). Each contribution perturbs the lattice Hamiltonian (E) through a different term. T is the kinetic energy of the lattice, and U_2 and U_3 are the harmonic and anharmonic contributions to the lattice potential energy. 43
- 3.2 **Klemens Model Comparisons to Simulation and Experiment** Thermal conductivity reductions due to point defect scattering for two systems at 300 K: (a) Si based on DFT dispersions and \mathbf{T} matrix scattering theory (points) and the Klemens model (lines) and (b) $\text{Mg}_2\text{Sn}_{1-x}\text{Si}_x$ from experiment (points), \mathbf{T} matrix theory (dotted), and Klemens model (solid) [65, 73, 74] 44
- 3.3 **Phonon Dispersion Diagrams Implied by the Virtual Crystal and Monatomic Lattice Approximations** The MLA and VCA represented in a 1D diatomic chain. In the MLA, the primitive unit cell is unaltered, but the atoms contained within are summed into a single, vibrating mass. As a result, there is no optical branch. In the VCA, the primitive unit cell is reduced to one atom, causing a tupling of the Brillouin zone. The large acoustic branch in this case includes the phonon states previously in the optical branch. 48
- 3.4 **Unit Cell Basis: Schematic of Microstates with Differing Scattering Strengths** In an example 2-atom primitive unit cell (shown in dotted line), three possible microstates exist, containing 0,1, or 2 impurity atoms. In the unit cell basis, each microstate would contribute a term to the overall scattering parameter (Γ). 48
- 3.5 **Off-stoichiometric Defect Scattering Model Applied to Literature Data** Both vacancy and interstitial scattering data from literature (points) can be described using a simple treatment of broken (or added) bonds based on the virial theorem (line). Normalized thermal conductivity reductions for systems with (a) stoichiometric vacancies, where \square represents a vacancy [88, 89, 91] and (b) stoichiometric interstitial atoms [59, 96] 53
- 3.6 **VFe₂Al: Lattice Thermal Conductivity Trends with Composition and Temperature** κ_L trends with changes in composition are well described by analytic alloy scattering models. (a) κ_L versus composition curves from the literature [101–103] are modelled using the Klemens alloy scattering model. (b) κ_L versus temperature curves with varying Co dopant concentrations from Lu et al. [104] are modelled using point-defect and umklapp scattering theory fit with a single Grüneisen parameter of 2.78. 54
- 3.7 **Effect of κ_L on zT Trends with Carrier Concentration n** The zT versus carrier concentration (n) curves at 300 K from a two-band model for

the valence and conduction band using a bandgap value of $E_g = 0.02$ eV. The blue curve includes the n -dependence of κ_L is included using the point defect scattering strength of Ge for n-type and Re for p-type. In contrast, the orange curve uses the constant pristine κ_L value of 28 W/m/K. Finally, we compare to experimental zT scatter points for both the Ge-doped [101] and Re-doped [103], which show good correspondence with the two-band model combined with the Klemens alloy scattering model for κ_L . Here, we emphasize that including the n -dependence of κ_L is important both for modelling the correct magnitude of zT , but also the correct n values at which it is optimized. The shift in optimal n value is signified by the dotted gray lines.

55

- 4.1 **Schematic of Muggianu Model** The geometric Muggianu model provides a method to determine a ternary excess quantity (multicolored center composition) from a weighted sum of corresponding binary excess quantities. Binary compositions are shown along binary systems as red, blue, and green scatter points. 66
- 4.2 **Thermoelectric Transport Properties for (Ti, Zr, Hf)NiSn System** Alloy model predictions for the (a) electronic transport function σ_{E0} , (b) lattice thermal conductivity κ_L , and (c) quality factor B for the (Ti,Zr,Hf)NiSn system. Experimental scatter points are overlaid, and in cases where a composition was measured multiple times, the median value is plotted here. Contour lines from the DFT investigation by Eliassen *et al.* [123] are reproduced in panel (b) for comparison purposes. See Appendix Section D for full data. 69
- 4.3 **Summary of Thermoelectric Modelling and Data for Remaining Compound Families** Alloy model predictions with overlaid experimental scatter points for three compound families: $X\text{FeSb}$, $X\text{CoSn}$, and $X\text{CoSb}$. For each system, the electronic transport function σ_{E0} , lattice thermal conductivity κ_L , and quality factor B are shown. Although each compound family has the same motif for lattice thermal conductivity, with κ_L minimized along the binary with highest mass contrast, the B factor plots show very different patterns of high and low performance regions. This speaks to the trade-off between thermal and electronic property variation with alloying. 71
- 4.4 **Lattice Thermal Conductivity of IV-VI Reciprocal System** Lattice thermal conductivity heatmap in the quaternary IV-VI semiconductor system. Both the experimental measurements (a) and alloy model (b) show the thermal conductivity minimized near the equiatomic $\text{Pb}_{0.5}\text{Sn}_{0.5}\text{Te}_{0.5}\text{Se}_{0.5}$ composition. In this system, substitution on both the cation and anion site yields a peak mass and strain contrast (c,d) near the center of the compositional space. 72
- 4.5 **Hall Hole Mobility of IV-VI Reciprocal System** Hall mobility heatmap in p-type quaternary $\text{PbTe-PbSe-SnTe-SnSe}$ alloy system. The experimental data (a) is reproduced from Ortiz *et al.* [111] and is compared to the alloy mobility model extrapolated using the Muggianu method (b). Finally, we plot

- deviation between the experiment and mobility $|\mu_{\text{exp}} - \mu_{\text{alloy}}|$, which helps to isolate the effect of density-of-states variations (Δg) across the alloy range. 73
- 4.6 **Orthogonal Point Defect Scattering Strategies** Multicomponent alloy design strategies for reduced thermal conductivity due to point defect scattering should take advantage of orthogonal scattering effects. (a) Schematic of lattice with 2-atom primitive unit cell basis (encircled by dotted line). (b) Alloy elements, labelled 1 and 2, substitute on different sublattices. (c) Alloy element 1 contributes significant mass contrast while alloy element 2 contributes significant strain contrast. 74
- 4.7 **Example Phonon Bandstructure Colored by Tamura Model Weighting Term** The phonon bandstructure of NaCl, in which phonon states are colored by the eigenvector overlap factor $\phi_{\mathbf{q}}(s)$, which weights the mass difference scattering term in the Tamura model. In this case, the bandstructure is colored by the $\phi_{\mathbf{q}}(s = \text{Na})$ term, and as the lighter element, Na follows the expected behavior by showing higher participation in the higher frequency range. The $s = \text{Cl}$ case is the exact negative of the heatmap shown, such that the scattering frequency window is in the lower frequency range. 76
- 4.8 **Decoupled Mass and Strain Scattering in Multicomponent Alloy** Example ternary alloy in which the mass contrast (Γ_{M}) and strain contrast (Γ_{R}) are maximized along different binary systems. The total scattering parameter Γ is then peaked in the middle of the ternary alloy space, such that the minimum thermal conductivity region (encircled) is also centered around the equiatomic composition. 77
- 4.9 **Physics-Informed Gaussian Process Regression Transport Function Model** (a) Prediction values and (b) their associated standard deviations from the physics-informed Gaussian process regression model for σ_{E0} . The Ti-rich region with high σ_{E0} is reported to be the result of an increase in Seebeck effective mass [137]. This high-performance region is not captured by the physics-based alloy scattering models alone. 79
- 5.1 **Temperature Profiles for Landauer Transmissivity and Scattering Transport Theories** Temperature profiles in a sample with an average grain size L_x . In the scattering model, the interface perturbation modifies the overall phonon lifetime and maintains a uniform temperature gradient across the sample. Landauer theory allows for spatial variation of the applied field and supports temperature drops spatially localized at the interfaces. 85
- 5.2 **Schematic of long and short mean-free-path phonons in a polycrystalline material** [modeled off of Figure 1 in Ref. [161]]. Short mean-free-path phonons will be scattered by mechanisms within the grain (phonon-phonon interactions, point defects) and will, therefore, not interact with grain boundaries and interfaces. 88

- 5.3 **Spectral Thermal Quantities Extrapolated to the Γ Point** Spectral thermal quantities (C_V , $v_{g,xx}^2$, $\tau^{-1} = \Gamma$) for Si are calculated using the tetrahedron method on an (11,11,11) mesh. The red curves near the Γ point reflect the frequency-dependencies based on a Debye model and umklapp phonon-phonon scattering. While the value for $v_{g,xx}^2$ is computed from DFT acoustic velocities at the Γ point, the red curves for C_V and τ^{-1} are fit. An extrapolated value for $\lim_{\omega \rightarrow 0} \kappa_{xx}$ is then computed using the phonon gas model. The value of 4.95 W/m/K is close to that estimated using Equation 5.7 of 4.16 W/m/K. 89
- 5.4 **Adjustment of Spectral Thermal Conductivity at Γ Point** (a) Rather than approaching zero at the Γ point, κ_L is modified to converge to a value of 4.95 W/m/K/THz. (b) The impact of the adjustment is shown in the cumulative thermal curve, which has a higher slope near Γ and a higher overall thermal conductivity, closer to the converged κ value attained using a higher mesh density. 90
- 5.5 **Schematic of Interfacial Scattering Mechanisms and Implied Phonon Transitions** (a) The acoustic impedance mismatch across the interface can lead to a reflection or transmission probability in analogy to Snell's law. (b) Many low-energy interfaces can be decomposed into periodic arrays of dislocations, which act as a diffraction grating for phonons. The dislocation array can impart quantized momentum in units of $2\pi/D$, where D is the dislocation spacing. (c) Interfaces serve as a sink for point defects, leading to additional roughness and compositional disorder. These effects are often modeled as a source of diffuse phonon scattering, in which only phonon energy is conserved at the interface. (d) Finally, if the vibrational basis set includes the interfacial vibrational modes, such as the localized mode portrayed here, coupling to interfacial modes can also enhance or diminish the interfacial thermal conductance through inelastic processes. 92
- 5.6 **Interfaces Described by a Grid of Linear Defects** (a) Schematic of a twist boundary with misorientation angle θ . The black lines indicate screw dislocations and the blue/green shading indicates shear strain. (b) A semicoherent heterointerface between two materials with lattice constants a_1 and a_2 . The black lines indicate edge dislocations and the blue/green shading indicates hydrostatic strain. 95
- 5.7 **Two Interfacial Scattering Effects Addressed: Acoustic Mismatch and Dislocation Strain** Scattering at a semicoherent heterointerface stems from the periodic strain fields at a misfit dislocation array as well as the step function change in acoustic impedance. (a) Analytic solution for the dilatational strain field component ϵ_{yy} from an infinite array of misfit dislocations periodically spaced along the y -axis [180, pp. 695-697]. (b) Cross-section of 3D dilatational strain field, showing an underlying step function (dotted red line). This is indicating a change in lattice parameter (a) from material 1 to 2, rather than

- long-range strain. We subtract off the step function in strain, and instead treat this effect with an acoustic mismatch scattering term. This leaves the physical strain (ϵ_{eff}), which we treat with an anharmonic strain scattering potential. 98
- 5.8 **Dislocation Structure of a Symmetric Twist Grain Boundary**
Schematic of two orthogonal screw dislocation arrays, with Burgers vectors \mathbf{b}_1 and \mathbf{b}_2 , respectively, producing a twist misorientation (θ) at an interface. 99
- 5.9 **Diagrams of Dislocation Grid and Associated Scattering Phase Space**
(a) Diagram of orthogonal YZ and ZY arrays in dislocation cross-grid. In this case, equal D spacing is assumed for both. (b) Phase space diagram portraying the independent scattering of the YZ and ZY dislocation array, which overlap only at the $\mathbf{Q}_{\parallel} = 0$ ($n' = m' = 0$) condition. 102
- 5.10 **Group velocity Slowness Plots for Silicon** Direction dependence of the acoustic phonon group velocities plotted on a unit sphere. Fast/slow secondary correspond approximately to the two transverse branches, and primary is approximately the longitudinal branch. Produced using the `christoffel` package [27]. 107
- 5.11 **Comparison between Acoustic Mismatch Perturbation Potential and Classical Method.** a) (*copy of Figure 5.1*) A schematic illustration of two common models used to describe heat conduction in materials with interfaces. The blue line depicts the Landauer based model where a thermal boundary resistance arising from the conduction channel having a interfacial transmission probability or $t(\omega) > 0$, induces a sharply localized drop in temperature. The red line depicts a model based on phonon scattering theory and Matthiessen's rule, where each scattering mechanism contributes a scattering rate ($\tau(\omega)^{-1}$), and together modify the materials thermal conductivity homogeneously. b) A comparison between the transmissivity calculated using classical acoustic mismatch (AMM) theory and the interface perturbation theory, showing that the two cases differ by no more than 5% up to $\Delta v/v = 0.5$. 109
- 5.12 **Relaxation Time versus Incident Phonon Direction** Three-dimensional polar plots of the scattering rate $\tau^{-1}(\mathbf{q})$ (in GHz) versus incident angle (θ_i, ϕ_i) of an incoming phonon, holding phonon frequency constant. The results shown correspond to a twist boundary with $\theta = 5^\circ$ at the (a) long wavelength limit ($q = q_{\text{max}}/20$), where acoustic mismatch scattering dominates and the (b) short wavelength limit ($q = (2/3)q_{\text{max}}$), where the periodic strain field scattering effect is picked up. 111
- 5.13 **Si Twist Boundary Phonon Lifetime Predictions** (a) Spectral phonon lifetimes for a Si-Si twist interface at various misorientation angles (b) The log-log plot of this relaxation time shows a power law crossover from ω -independent to $\sim \omega^{-1}$, indicating a transition from planar-defect to linear-defect scattering. (c) The long-wavelength limit of the relaxation time is plotted against grain boundary angle, revealing a periodic variation stemming from the symmetry of the acoustic velocities. 111

- 5.14 **Comparison of Si Tilt and Twist Grain Boundary Scattering** (a) The spectral relaxation time (τ) converges at the long-wavelength limit, but decreases faster in the frequency-dependent regime for the twist boundary, when dislocation strain scattering is activated. (b) The twist boundary, therefore, is predicted to have about $1.3\times$ the thermal boundary resistance (R_K). 112
- 5.15 **Thermal Boundary Resistance correlates with Read-Shockley (R-S) Grain Boundary Energy** Twist boundary model predictions of the thermal boundary resistance (R_K) are shown as blue scatter points (mapped to right axis) and closely follow the Read-Shockley interfacial energy (red line; mapped to left axis). Both additionally trend with misorientation angle θ for low angle grain boundaries. Similar trends between R_K , R-S energy, and θ have also been shown through experiment and simulation [170, 183]. 114
- 5.16 **Si-Ge Heterointerface Phonon Lifetime and Kapitza Resistance Predictions** Si-Ge heterointerface scattering using a Born-von Karman phonon dispersion (a) Spectral lifetime for a Si-Ge heterointerface with a misfit dislocation spacing of 7 nm, comparing model with acoustic mismatch and dislocation strain (solid) to the model with acoustic mismatch alone (dotted) (b) Thermal boundary resistance predictions versus temperature from the heterointerface model with (solid) and without (dotted) dislocation strain scattering. Dislocation strain accounts for 50% of the overall thermal resistance. 116
- 5.17 **Diffraction Effects and Dimensionality Crossover in Dislocation Core Arrays** Phonon lifetimes including the effects of dislocation core and acoustic mismatch scattering for a 7° symmetric Si twist boundary. (a) Scattering rate plot for a phonon of normal incidence to the interface. Diffraction peaks occur at intervals of $|k| = 2\pi n/D$, where there is a spike in the number of allowed phonon transitions. (b) The log-log plot of the spectral relaxation time depicts smooth cross-over between ω -independent scattering (signature of planar acoustic mismatch scattering) and ω^{-3} scattering (signature of dislocation core scattering). An intermediate regime with ω^{-2} scattering may also be present, in which long wavelength phonons view the array of dislocation cores as a planar mass defect. 118
- 5.18 **Dislocation Core versus Strain Scattering Comparison** Comparison between the dislocation core and dislocation strain scattering effects in a 7° symmetric Si twist boundary. Phonon lifetimes (a) and Kapitza resistance (b) are compared between 1) a model including dislocation core and acoustic mismatch scattering (DC + AM) and 2) a model including dislocation strain and acoustic mismatch scattering (DS + AM). The strain scattering is shown to be the dominant effect at the interface, such that the contribution from dislocation core scattering can be ignored. 119
- 6.1 **Process-Structure-Properties-Performance Diagram for Thermoelectrics** Relationships between sample preparation, characteristics, properties, and performance are highlighted for bulk thermoelectric compounds. In an

integrated computational materials engineering (ICME) approach, the linkages are described through analytic or simulation-based methods. 124

C.1

Phonon-Vacancy Scattering: Virial Theorem Model versus

Experiment The mass difference model with the unit cell volume error (light blue) is compared to the mass difference only model described in this study (dark blue) as well as the vacancy model (dashed) with the virial treatment for broken bonds, which best captures the κ_L reduction [88]. 155

PhD Candidate in Materials Science and Engineering

Northwestern University, 2017-present

Member of Snyder Thermoelectrics Group

COMPLETED EDUCATION

MPhil with Distinction in Scientific Computing

University of Cambridge, Class of 2017, **Churchill Scholarship**

Honors B.S. in Materials Science & Engineering; Minor in Nanotechnology

Pennsylvania State University, Class of 2016, **Summa Cum Laude**

TECHNICAL EXPERIENCE

Multiscale Physics-based Thermal Transport Models

PhD: Graduate Research Assistant

Nov 2017- present
Northwestern University

- Thesis title: *Phonon-Defect Interactions in Semiconductor Materials*
- Applying CALPHAD mixing models to predict thermoelectric properties in a high-entropy alloy space
- Developed a semi-empirical model to predict the thermal boundary resistance of symmetric tilt and twist grain boundaries as well as semicoherent heterointerfaces. [Shared Python Codebase](#)
- Performed meta-analysis of thermal conductivity data in alloyed thermoelectric materials and developed a new, conceptually clear model of solid solution scattering of phonons

Modeling and Uncertainty Quantification: Battery and Thermoelectric Materials

Summer Internship

June-August 2019
Argonne National Laboratory

- Applied Bayesian inference to uncertainty quantification and model selection for thermoelectric property models
- Developed equivalent circuit models for Li-ion battery charge and discharge curves

Software Development for Integrated Computational Materials Engineering (ICME)

Summer Internship

June-August 2019
QuesTek Innovations

- Back-end programming for thermoelectric property database and prediction engine
- Python package development for uncertainty quantification of thermodynamic models using Bayesian inference

Nanoparticle Structure Determination and Heuristic Classification

Churchill Scholarship: MPhil in Scientific Computing

Jan -Sept 2017
University of Cambridge

- Thesis title: *Structure Determination of Ni-C Nanoclusters using Tight-binding and Heuristic Methods*
- Computed the relaxed structure of nanoparticle catalysts used in carbon nanotube growth
- Developed a machine learning tool to identify different structural regions of the nanoparticle

Thin Films for Magnetic Tunnel Junctions

NIST Summer Undergraduate Research Fellow

May- August 2016
National Institute of Standards and Technology

- Fabricated and characterized the magnetic and electrical properties of thin film magnetic tunnel junctions

Electrical Contacts for Thin Film Photovoltaics

Undergraduate Research Assistant

Sept 2013 - May 2016
Pennsylvania State University

- Thesis title: *Investigation of Ohmic Contacts to Tin (II) Sulfide*
- Experimental screening for electrical contact materials to tin sulfide for solar cell applications
- Developed MATLAB tool to evaluate a ternary phase diagram based on the thermochemical properties of the binary phases. The code has since been applied to study the phase equilibria between metal contact candidates and binary semiconductors, including SnS, WSe₂, and MoS₂.

Thin Films for Spintronics and Magnetic Memory

EuroScholars Research Abroad Program

Aug - Dec 2015

Leiden University, Netherlands

- Fabricated switching devices to study spin-injection from a ferromagnet to normal metal with applications to spintronics/magnetic memory

Robotics-Enabled Combinatorial Nanocrystal Synthesis

US Department of Energy Research Internship

June - Aug 2015

Lawrence Berkeley National Laboratory

- Programmed liquid-handling robot to operate as tool for high-throughput, automated nanoparticle synthesis

Monte Carlo Simulation of Defect Interactions

NanoJapan: International Research Experience for Undergraduates

May- Aug 2014

Tohoku University, Japan

- Participated in 12-week NSF-funded research/ cultural excursion program in Japan
- Developed a Monte Carlo model to study crystal defects in cubic silicon carbide

Design and Construction of Thin Film Deposition System

Summer Research Intern

June- Aug 2013

SUNY Polytechnic Institute

- Constructed a DC sputter deposition system including full setup of pneumatic and electrical controls

SELECTED HONORS AND AWARDS

PPG Fellowship (2020)

The Churchill Scholarship (2017)

Northwestern Data Science Initiative Fellowship (2017)

Cabell Fellowship (2017)

Student Marshal (Top GPA) for the College of Earth and Mineral Sciences Spring 2016 Commencement

Dean Edward Steidle Memorial Scholar Award (2016)

TEACHING/OUTREACH EXPERIENCE

Teaching Assistant: Teaching experience in materials design and physics of materials

- Materials Engineering Methodology and Design (2015-2016)

- Thermal and Electronic Properties of Materials (2018)

- Physics of Materials (2019)

Diversity and Inclusion: Elected graduate student representative of the Northwestern Materials Science and Engineering department diversity, equity, and inclusion committee (2020-2021)

Science Educational Outreach: Coach for hands-on science activities in US and UK schools (2014-present)

Science Communication: Cambridge science magazine writer/ FameLab science speaking finalist (2017)

TECHNICAL STRENGTHS

Programming Languages

Python, MATLAB, C++, JAVA, C#, Bash scripting, (exposure to Fortran)

Laboratory Techniques

Thin Film Deposition; Nanoparticle Synthesis; Optical and Electron

Microscopy; Lithography; Electrical, Optical, and Magnetic Characterization

REFEREED JOURNAL ARTICLES

1. **R. Gurunathan**, S. Sarker, G.J. Snyder, L. Ward, A. Mehta (in preparation). Modeling Thermoelectric Transport in a Multicomponent Alloy Space.
2. R. Hanus, **R. Gurunathan**, Lucas Lindsay, Matthias T. Agne, Jingjing Shi, Samuel Graham, G.J. Snyder. Thermal transport in defective and disordered materials. (accepted by Applied Physics Reviews as feature article).
3. **R. Gurunathan**, R. Hanus, A. Garg, G.J. Snyder. Thermal Resistance at a Twist Boundary and a Semicoherent Heterointerface. *Physical Review B*, **103**, 144302.
4. K. Imasato, S. Anand, **R. Gurunathan**, G.J. Snyder. The Effect of Mg₃As₂ Alloying on the Thermoelectric Properties of n-type Mg₃(Sb, Bi)₂. *Dalton Transactions*, **50**, 9376-9382.
5. Y. Sun, Y. Zhou, **R. Gurunathan**, J-Y. Zhang, M. Hu, W. Liu, B. Xu, G.J. Snyder. Phonon Scattering in the Complex Strain Field of a Dislocation in PbTe. *Journal of Materials Chemistry C*, **9**, 8506-8514.

6. S. Anand, **R. Gurunathan**, T. Soldi, L. Borgsmiller, R. Orenstein, G.J. Snyder (2020). Thermoelectric transport of semiconductor full-heusler VFe₂Al. *Journal of Materials Chemistry C*, **8**, 10174-10184.
7. **R. Gurunathan**, R. Hanus, G.J. Snyder (2020). Alloy Scattering of Phonons. *Materials Horizons*, **7**, 1452-1456.
8. G.J. Snyder, A. Snyder, M. Wood, **R. Gurunathan**, B. Snyder, C. Niu (2020). Weighted Mobility. *Advanced Materials*, **32**, 2001537.
9. **R. Gurunathan**, R. Hanus, M. Dylla, A. Katre, G.J. Snyder (2020). Analytical Models of Phonon–Point-Defect Scattering. *Physical Review Applied*, **13**, 034011.
10. S. Wang, D. Xu, **R. Gurunathan**, G.J. Snyder, Q. Hao (2020). Thermal studies of individual Si/Ge heterojunctions—The influence of the alloy layer on the heterojunction. *Journal of Materiomics.*, **6**, 248-255.
11. G.J. Snyder, M. Agne, **R. Gurunathan** (2019). Thermal Conductivity of Complex Materials. *National Science Review*, **6**, 380-381.
12. M. Wang, **R. Gurunathan**, K. Imasato, N. Geisendorfer, A. Jakus, J. Peng, R. Shah, M. Grayson, G.J. Snyder (2019). A Percolation Model for Piezoresistivity in Conductor-Polymer Composites. *Advanced Theory and Simulations*, **2**, 1800125.
13. K. Cooley, R. Alsaadi, **R. Gurunathan**, A. Domask, L. Kerstetter, W. Saidi, S. Mohney (2019). Room-temperature epitaxy of metal thin films on tungsten diselenide. *Journal of Crystal Growth*, **505**, 44-51.
14. **R. Gurunathan**, J. Nasr, J. Cordell, R. Banai, M. Abraham, K. Cooley, M. Horn, S. Mohney (2016). Pd and Au Contacts to SnS: Thermodynamic Predictions and Annealing Study. *Journal of Electronic Materials*, **45**, 6300-6304.
15. J. Nasr, J. Cordell, **R. Gurunathan**, J. Brownson, M. Horn (2017). Phase Control of RF Sputtered SnS_x with Post-Deposition Annealing for a Pseudo-Homojunction Photovoltaic Device. *Journal of Electronic Materials*, **46**, 1215-1222.
16. H. Nagasawa, **R. Gurunathan**, M. Suemitsu (2015). Controlling Planar Defects in 3C-SiC: Ways to Wake it up as a Practical Semiconductor. *Materials Science Forum*, **821-823**, 108-114.
17. A. Domask, **R. Gurunathan**, S. Mohney (2015). Transition Metal-MoS₂ Reactions: Review and Thermodynamic Predictions. *Journal of Electronic Materials*, **45**, 4065-4079.

NON-REFEREED TECHNICAL REPORTS

1. *Uncertainty Quantification of Phase Equilibria and Thermodynamics Workshop Report* (2020) Center for Hierarchical Materials Design (CHiMaD).
2. *MagicMat: Materials Genome and Integrated Materials Toolkit* (2020) SBIR Phase I Technical Report.

CONFERENCE ORAL PRESENTATIONS

1. R. Gurunathan, S. Sarker, L. Ward, J. Saal, A. Mehta, G.J. Snyder (2021) *Virtual Conference on Thermoelectrics*, online.
2. R. Gurunathan, R. Hanus, A. Garg, G.J. Snyder (2021) *Electronic Materials and Applications*, online (**invited**).
3. R. Gurunathan, R. Hanus, A. Garg, G.J. Snyder (2020) *Virtual Conference on Thermoelectrics*, online.
4. R. Gurunathan, G.J. Snyder (2019) *The North American Thermoelectric Workshop*, Evanston, IL.
5. R. Gurunathan, G.J. Snyder (2019) *North American Solid State Chemistry Conference*, Golden, CO. (**invited**)
6. R. Gurunathan, R. Hanus, G.J. Snyder (2019) *Int'l Conference on Thermoelectrics*, Gyeongju-shi, Korea.
7. R. Gurunathan, R. Hanus, G.J. Snyder (2019) *APS March Meeting*, Boston, MA.
8. R. Gurunathan, S. Mohney (2016) 58th *Electronic Materials Conference*, Newark, DE.

PROFESSIONAL REFERENCES

- Professor G. Jeffrey Snyder, *Northwestern University*: jeff.snyder@northwestern.edu
- Dr. Logan Ward, *Argonne National Laboratory*: lward@anl.gov
- Professor Suzanne Mohney, *Pennsylvania State University*: sem2@psu.edu